Mesoporous TiO_2/Fe_2O_3 bicomposites: synthesis and mechanistic studies of arsenic scavenging

A thesis submitted for the degree of

Doctor of Philosophy

By

Chaipat Lapinee

Department of Chemistry

Imperial College London

September 2016

Declaration of Originality

I, Chaipat Lapinee, hereby declare that the research describe in this thesis was conducted under the supervision of Professor Ramon Vilar and Professor Dominik Weiss at the Department of Chemistry, Imperial College London, and is entirely my own work unless otherwise stated.

Chaipat Lapinee

September 2016

Copyright Declaration

The copyright of this thesis rests with the author and is made available under a Creative Common Attribution Non-Commercial No Derivative licence. Researchers are free to copy, distribute or transmit the thesis on the condition that they attribute it, that they do not use it for commercial purposes and they do not alter, transform or build upon it. For any reuse or redistribution, researchers must make clear to others the licence terms of this work.

Acknowledgements

First of all, I would like to express my sincere thanks to my supervisors, Prof. Ramon Vilar, Prof. Dominik Weiss and Dr. Pascal Salaün for their suggestions, supports and for inspiring me during my time here.

I acknowledge support from Dr. Andrew Berry, Prof. Stephen Skinner, Dr. Jens Najorka, Dr. Giannantonio Cibin, Dr. Fred Mosselmans and Dr. Paul Wilde.

I would like to give special thanks to Barry, Chris, Florence, Tamara, Stelios, Peter, Matt R., Janice, Jennifer L., Matt K. and other friends in the MedInChem and the Environmental Geochemistry group for helps and supports. A big hug for my Thai friends here, including Nitipol, Mason, Picha, Nat, Veena, Achaya, Tonghathai, Channarong, Wiyada, Piyada, Sirirat, Krisana and also thanks to my UK friends, Leo, Julian, Andrew, Edward, and Alex for all the nice times together. My sincere thanks also go to my UK family, Mrs. Prateep Lapinee Ruddy and Mr. Kevin Ruddy for love and supports.

I would like to express my gratitude to the Royal Thai Government and the University of Phayao for PhD scholarship and also acknowledge Imperial College London and Diamond Light Source grants for synchrotron project 2014 and 2015.

Finally, I would love to say thank you so much to my parents and everyone in my family for their love and great support throughout of my life.

Abstract

Many parts of the world have arsenic contamination problems in drinking and ground water. The high toxicity of arsenic threatens people's health, since exposure to it can cause cancer and other dangerous diseases. Inorganic arsenic in natural water is found in two oxidation states, As^{V}(arsenate) or As^{III}(arsenite). As^{III} has the highest toxicity comparing with As^{V} and difficult to remove due to zero charge species of As^{III} at pH below 9. Consequently, photocatalytic oxidation of arsenite is a key challenge to improve removal efficiencies of future sorbents. Recent work has suggested that a TiO_2/Fe_2O_3 binary mixed oxides could play a key role in the design of future sorbents as it combines photocatalytic oxidation and adsorptive properties alike.

The aim of this thesis presented was to characterise the interaction of arsenic with TiO_2/Fe_2O_3 binary mixed oxides synthesised using different methods and to critically evaluate the potential of these bicomposites for future development work.

To this end, three different synthetic methods with respect to cost, time and energy consumption during production were tested. The mechanisms of arsenic interaction were assessed using macroscopic (i.e. adsorption isotherms, adsorption kinetics) and microscopic (i.e. synchrotron techniques) studies and the photocatalytic oxidation was studied using synchrotron and UV irradiation.

An electrochemical method for detection of arsenic has been implemented for the accurate analytical determination of As^{III} and As^{V} down to levels of 0.4 ppb using stripping voltammetry. TiO_2/Fe_2O_3 binary mixed oxides have been prepared using a co-precipitation method, a mesoporous method and sol-gel method.

The adsorption capacities of As^{III} on mesoporous TiO_2/Fe_2O_3 binary mixed oxides were found at 29.44±2.99, 22.64±1.74 and 21.60±0.33 mg g^{-1} at pH 5, 7 and 9, respectively. The adsorption kinetics study found the rate constant (k_2)

0.02 g mg^{-1} min^{-1}. The photocatalytic oxidation rate constant (k_{ox}) of As^{III} onto the surface of TiO_2/Fe_2O_3 binary mixed oxides with synchrotron beam irradiation found in between 0.062 to 0.078 min^{-1}. Additionally, the rate constant (k_{ox}) of As^{III} phototalytic oxidation in bicomposite suspension with UV irradiation found at $4.37x10^{-3}$ min^{-1}.

The binding mode of As^{III} and As^{V} onto the surface of TiO_2/Fe_2O_3 binary mixed oxides was to be a bidentate mononuclear edge sharing (^2E) complex and a bidentate binuclear corner sharing (^2C) complex.

Mesoporous TiO_2/Fe_2O_3 binary mixed oxides have been highlighted to be the best bicomposites in this study due to the highest adsorption capacities and ability to photocatalytic oxidation of As^{III} to As^{V}.

Table of Contents

Acknowledgements……..3

Abstract……4

Table of Contents…….6

List of Figures……11

List of Tables……..17

List of Schemes……..19

List of Abbreviations……..20

1. Introduction……21

1.1 Background……...21

1.1.1 Global contamination of ground water with arsenic…….....21

1.1.2 Speciation of arsenic…….23

1.1.3 Current arsenic removal techniques……..24

1.1.3.1 Coagulation and Precipitation……...24

1.1.3.2 Methods based on membrane technology…….25

1.1.3.3 Methods based on adsorption onto metal oxides……..26

1.2 Synthesis of metal oxides …….27

1.2.1 Synthesis of TiO_2…….27

1.2.2 Synthesis of TiO_2/Fe_2O_3 binary mixed oxides…….29

1.3 Adsorption mechanism of arsenic onto metal oxides ……31

1.3.1 Adsorption isotherms……...32

1.3.2 Adsorption kinetics of arsenic on metal oxides……...35

1.3.3 Geometry of arsenic complex onto the surface of iron oxides and TiO_2 ……36

1.4 Photocatalytic oxidation mechanism of As^{III} on TiO_2……...40

1.5 Analytical methods for the detection of arsenic…….45

1.6 Aims and Objectives…….47

References……..47

2. Experimental methods…….....53
2.1 Synthesis of TiO_2/Fe_2O_3 binary mixed oxides ……..53
2.1.1 Synthesis of co-precipitated TiO_2/Fe_2O_3 binary mixed oxides (CP).54
2.1.2 Synthesis of mesoporous TiO_2/Fe_2O_3 binary mixed oxides (MB)…54
2.1.3 Synthesis of sol-gel TiO_2/Fe_2O_3 binary mixed oxides (SG)…….55
2.1.4 Characterization of TiO_2/Fe_2O_3 binary mixed oxides …….....56
2.2 Voltammetry…….....56
2.3 X-ray absorption spectroscopy (XAS)……..57
2.3.1 Solid samples……...58
2.3.2 Solution samples……..58
2.3.3 Data analysis……59
2.4 Adsorption using batch and column experiments……60
2.4.1 Batch experiment…….....60
2.4.2 Column experiment……..61
2.5 Photocatalytic oxidation……...61
2.5.1 In situ photocatalytic oxidation……...62
2.5.1.1 Photocatalytic oxidation of As^{III} on mineral surface using synchrotron beam……62
2.5.1.2 Photocatalytic oxidation of As^{III} on mineral surface using UV 18 watt light…….62
2.5.2 Ex situ photocatalytic oxidation……...65
2.5.2.1 UV 18 watt and then As analysis using voltammetry……..65
References……..65

3. Adsorption capacity, kinetics and mechanism of arsenite on mesoporous TiO_2/Fe_2O_3 binary mixed oxides ……...66
3.1 Introduction…….67
3.2 Aims and objectives…….....71
3.3 Results and discussion……..72
3.3.1 Mesoporous TiO_2/Fe_2O_3 binary mixed oxides (MB)

synthetic method……..72
3.3.2 BET surface area and pore size of mesoporous TiO_2 (MT) and mesoporous TiO_2/Fe_2O_3 binary mixed oxides TiO_2/Fe_2O_3 (MB)…74
3.3.3 Adsorption isotherms of As^{III} on mesoporous TiO_2/Fe_2O_3 binary mixed oxides……76
3.3.4 Evidence of competitive adsorption of As^{III} and phosphate on MB……..81
3.3.5 Determination of the active sites of the MB……82
3.3.6 Adsorption Kinetics……85
3.3.7 Continuous flow system for scavenging of arsenic…….....92
3.3.7.1 Effect of pH solution on As^{V} removal……92
3.3.7.2 Effect of MB amount on As^{III} and As^{V} removal……..93
3.3.7.3 Effect of flow rate on As^{V} removal……...94
3.3.7.4 MB column regeneration……95
3.4 Conclusion……96
References……..97

4. Binding mode of arsenic oxides onto the surface of TiO_2/Fe_2O_3 binary mixed oxides……101
4.1 Introduction……102
4.2 Aims and objectives……...109
4.3 Results and discussion……110
4.3.1 Confirmation of arsenic oxidation states on the surface of TiO_2/Fe_2O_3 binary mixed oxides using XANES analysis…….110
4.3.2 EXAFS analysis of As^{III} adsorbed TiO_2/Fe_2O_3 binary mixed oxide materials……111
4.3.3 EXAFS analysis of As^{V} adsorbed on TiO_2/Fe_2O_3 binary mixed oxide materials……115
4.3.4 Geometry of arsenic TiO_2/Fe_2O_3 binary mixed oxide surface complexes……117

4.3.5 Effect of pH on geometry of arsenic adsorbed TiO_2/Fe_2O_3 binary mixed oxide surface complexes……....119
4.3.6 Effect of adsorption time on geometry of arsenic adsorbed on TiO_2/Fe_2O_3 binary mixed oxide surface complexes……...121
4.3.7 Discussion of binding modes of arsenic oxides on TiO_2/Fe_2O_3 binary mixed oxides …….123
4.3.7.1 Molecular structure of arsenic on TiO_2/Fe_2O_3 binary mixed oxides ……..123
4.3.7.2 Comparison of arsenic molecular structure adsorption on TiO_2/Fe_2O_3 binary mixed oxides at different pH values…124
4.3.7.3 Relationship between nature of binary mixed oxides and molecular structure of arsenic adsorption on TiO_2/Fe_2O_3 binary mixed oxides ……..125
4.3.7.4 Comparison of kinetic adsorption and molecular structure of arsenic on TiO_2/Fe_2O_3 binary mixed oxides ……...……..125
4.4 Conclusion……..126
References……127

5. Surface promoted photocatalytic oxidation of As^{III} to As^{V} using TiO_2/Fe_2O_3 binary mixed oxides ……129
5.1 Introduction……130
5.2 Aims and objectives……133
5.3 Results and discussion…….134
5.3.1 XANES analysis of As^{III} and As^{V} standards……..134
5.3.2 Effect of irradiation on photooxidation of As^{III} to As^{V} in the absence of TiO_2/Fe_2O_3 binary mixed oxides…….……135
5.3.3 Photocatalytic oxidation of As^{III} to As^{V} on the surface of TiO_2/Fe_2O_3 binary mixed oxides with UV(18W) irradiation…….136
5.3.4 Photocatalytic oxidation of As^{III} to As^{V} on the surface of TiO_2/Fe_2O_3 binary mixed oxides with synchrotron beam irradiation……138

5.3.5 Photocatalytic oxidation of As^{III} in aqueous solution using a tea-bag containing the TiO_2/Fe_2O_3 binary mixed oxides and synchrotron irradiation……..140
5.3.6 Photocatalytic oxidation of As^{III} in aqueous solution using TiO_2/Fe_2O_3 binary mixed oxide suspension with synchrotron beam irradiation in photo reactor……143
5.3.7 Photocatalytic oxidation of As^{III} to As^{V} using mesoporous TiO_2/Fe_2O_3 binary mixed oxide suspension……..145
5.3.8 The possible role of hydroxyl radical in the oxidation process…148
5.3.9 Photocatalytic oxidation kinetic rate calculations…….149
5.3.10 Design of photocatalytic oxidation reactor…….155
5.3.11 Effect of UV lamp energy on photocatalytic oxidation of As^{III} to As^{V} using MB…….....158
5.4 Conclusion……..159
References……159

6. Conclusions and future work……..162
6.1 Conclusions……162
6.2 Future work……163
References……164

List of Figures

Figure 1.1 Areas of arsenic contamination in groundwater including both natural and anthropogenic sources, Figure taken from Smedley and Kinniburgh [9]….22

Figure 1.2 Distribution of arsenic species as a function of pH, Figure taken from Guan et al., [16]……...23

Figure 1.3 The possible geometries of arsenate and arsenite on the surface of iron oxides and TiO_2, (A) goethite and lepidocrocite found similar geometries [61, 62, 63, 65], (B) ferrihydrite and hematite found similar geometries [61, 65], (C) anatase found only one geometric type [66]……36

Figure 2.1 The pellets of standard arsenic and arsenic bound TiO_2/Fe_2O_3 binary mixed oxides were sealed with kapton tape and set at the sample holder……..58

Figure 2.2 Picture of the experimental set-up to carry out studies of As^{III} adsorption and photocatalytic oxidation by TiO_2/Fe_2O_3 binary mixed oxides in a perspective photo reactor. The synchrotron beam passed through the solution at the beam path window……59

Figure 2.3 Photocatalytic oxidation of As^{III} to As^{V} with UV light and synchrotron beam, (A) the intensity of As^{III} XANES spectra was analysis before adding tea-bag of bicomposites and (B) tea-bag of bicomposite added, (C) the intensity of As^{III} XANES spectra was analysis before adding bicomposites in the solution and (D) suspension of TiO_2/Fe_2O_3 binary mixed oxides ……..64

Figure 3.1 The adsorption of As^{V} from solution at pH 7 by using CP, MB and SG, amounts of As^{V} adsorbed were compared to highlight the best bicomposite for arsenic removal, Figure taken from Bullough et al., [5] ……70

Figure 3.2 XRD patterns of mesoporous TiO_2 anatase synthesised by using a $Ti(OBu^n)_4$-P123-EtOH-HCl system, calcination at 350ºC for 4 h [3.48]. This material is called MT……72

Figure 3.3 XRD patterns of MB- TiO_2/Fe_2O_3 binary mixed oxides (1:1 mass ratio) synthesised by using co-precipitation of mesoporous TiO_2 (anatase) and Fe_2O_3 (hematite), calcination at 300 ºC for 6 h.……...73

Figure 3.4 Scanning Electron Microscope (SEM) images of mesoporous TiO_2/Fe_2O_3 binary mixed oxides (MB) at different magnifications (A) x1,500 (B) x2,500 presenting porous surfaces and size distribution of MB produced by studied method……74

Figure 3.5 Results of As^{III} adsorption on mesoporous TiO_2/Fe_2O_3 binary mixed oxides, As^{III} concentration ranged from 20 to 100 mg L^{-1} and sorbent concentration was 1 g L^{-1} in 0.01 M acetate buffer pH 5, 0.01 M HEPES buffer pH 7 and 0.01 M borate buffer pH 9 at temp. 25 ^{o}C (298 K), the plots show the average data from three replications of experiments, (±SD found in between 0.03 to 5.61), (A) adsorption isotherm plots at pH 5, pH 7 and pH 9, (B) Langmuir isotherm plots at pH 5, pH 7and pH 9 , (C) Freundlich isotherm plots at pH 5, pH 7 and pH 9. The experimental data plots were compared with the Langmuir and Freundlich models calculations at (D) pH 5, (E) pH7 and (F) pH 9……78

Figure 3.6 Effect of pH on As^{III} adsorption on 1 g L^{-1} MB at 298 K at pH 5, 7, 9 and 12 using initial concentration of 40 mg L^{-1} (±SD calculated from three replication experiments)…….81

Figure 3.7 Competitive adsorption of mixed As^{III} and phosphate (40 mg L^{-1}) solution on MB (As^{III} : Phosphate, 1:0, 1:1 and 1:10 concentration ratio) at pH 7 and 298 K (±SD calculated from three replication experiments)…….81

Figure 3.8 As^{III} adsorption kinetics on MB at different times in 0.01 M HEPES buffer pH 7 (298 K) with initial As^{III} concentration 40 mg L^{-1} and MB concentration 1 g L^{-1}. As^{III} concentration in solution decrease very fast in the first 15 min and slowly decrease until reach equilibrium. (A) As^{III} concentration in solution (mg L^{-1}) determined by voltammetry, (B) amounts of As^{III} adsorbed on MB (mg g^{-1}), (C) the experimental data fitted with the pseudo-first order model and (D) the pseudo-second order model……..86

Figure 3.9 The intra-particle diffusion (IDP) model for As^{III} adsorption on MB at pH 7 (25 ^{o}C), the plots presenting three different kinetic rates at different times…….89

Figure 3.10 Proposed As^{III} adsorption mechanism on the surface of MB describes by intra-particle diffusion kinetic model. The rate of adsorption relates to the diffusion of As^{III} from the solution to MB pore……...91

Figure 3.11 Removal of 100 µg L^{-1} As^{V} using 0.5 g MB column at pH 5, 7 and 9 with solution flow rate at 1 mL min^{-1}. (±SD calculated from three replications of measurement)…….92

Figure 3.12 Removal of 100 µg L^{-1} arsenic from solution by using different amounts of MB packed in column at pH 7 with 1 mL min^{-1}. Comparison of percent (A) As^{III} and (B) As^{V} removal using 0.05, 0.10, and 0.50 g MB column (±SD calculated from three replications of measurement)……..93

Figure 3.13 Results of solution flow rates effect on 100 µg L^{-1} As^{V} removal using 0.1 g MB column at pH 7 (±SD calculated from three replications of measurement)…….94

Figure 3.14 Recycle of 0.1 g MB column for 100 µg L^{-1} As^{V} removal at pH 7, comparison of percent As^{V} removal over five uses (±SD calculated from three replications of measurement)……..95

Figure 4.1 Possible binding modes of AsO_4^{3-} upon adsorption onto the surface of goethite (α-FeOOH), ^{1}V is a monodentate mononuclear corner sharing complex with an As-Fe distance of around 3.6 Å; ^{2}C is a bidentate binuclear corner sharing complex with an As-Fe distance of around 3.26 Å; ^{2}E is a bidentate mononuclear edge-sharing complex with an As-Fe distance of around 2.8 Å; Figure taken from Sherman and Randall [5]……...103

Figure 4.2 The surface structure of As^{V} adsorption on goethite, Figure taken from Fendorf et al., [6]……...104

Figure 4.3 As^{III} adsorption complexes on the surface of hematite (α-Fe_2O_3), ^{2}C is bidentate binuclear corner sharing complex, ^{2}E is bidentate mononuclear edge-sharing complex, Figure taken from Ona-Nguema et al., [9]…….105

Figure 4.4 Arsenic K-edge X-ray Absorption Near Edge Structure (XANES) spectra, (A) standard As^{III}, As_2O_3 and As^{V}, $HNa_2AsO_4.7H_2O$, arsenic adsorbed binary mixed oxides at (B) pH 5 and (C) pH 9, (D) Overlay of XANES spectra of As^{V} adsorbed CP-, MB-, SG- TiO_2/Fe_2O_3 binary mixed oxides at pH 7 for 2 and 24 h (spectra of six samples were found in the same position)……110

Figure 4.5 Arsenic K-edge EXAFS spectra for As^{III} adsorbed onto TiO_2/Fe_2O_3 bicomposites (CP and MB), K-edge EXAFS function (solid lines) and theoretical EXAFS calculation (dotted lines) for (A) As^{III}-CP and (B) As^{III}-MB. Radial structure Fourier transformed EXAFS spectra (solid lines) and theoretical EXAFS calculation (dotted lines) for (C) As^{III}-CP and (D) As^{III}-MB……...112

Figure 4.6 Arsenic K-edge EXAFS spectra for As^{V} adsorbed TiO_2/Fe_2O_3 binary mixed oxides (CP MB and SG), K-edge EXAFS function (solid lines) and theoretical EXAFS calculation (dotted lines)for (A) As^{V}-CP, (B) As^{V}-MB, and (C) As^{V}-SG. Radial structure Fourier transformed EXAFS spectra (solid lines) and theoretical EXAFS calculation (dotted lines) for (D) As^{V}-CP, (E) As^{V}-MB, and (F) As^{V}-SG…….116

Figure 4.7 The possible binding modes of As^{III} and As^{V} onto the surface of TiO_2/Fe_2O_3 binary mixed oxides indicated from our experimental results using EXAFS analysis, the interatomic distances of (A) As^{III}-Fe and As^{V}-Fe, (B) As^{III}-Ti, and As^{V}-Ti onto TiO_2/Fe_2O_3 binary mixed oxide surfaces……118

Figure 4.8 Interatomic distances from EXAFS fitting results of arsenic adsorption on CP and MB at pH 5, 7 or 9. (A) As^{III}-Fe_1 distances, (B) As^{III}-Fe_2 distances, (C) As^{III}-Ti distances, (D) As^{V}-Fe_1 distances, (E) As^{V}-Fe_2 distances and (F) As^{V}-Ti distances……...120

Figure 4.9 Interatomic distances from EXAFS fitting results of arsenic adsorption on CP, MB or SG for 2 or 24 h at pH 7. (A) As^{V}-Fe_1 distances and (B) As^{V}-Ti distances……... 122

Figure 5.1 XANES spectra at K-edge of As_2O_3 and $HNa_2AsO_4.7H_2O$ used to confirm oxidation states of arsenic on bicomposites……134

Figure 5.2 100 mg As^{III} L^{-1} solution irradiated using synchrotron beam during 30 min (A) XANES spectra of As^{III} solution, (B) percentage of As^{III} and As^{V} in solution……135

Figure 5.3 100 mg As^{III} L^{-1} solution irradiated using UV(18W) up to 30 minutes and subsequent determination of As^{III} using synchrotron beam, (A) K-edge of As^{III} in the XANES spectra of the solution, (B) percentage of As^{III} and As^{V} in solution……136

Figure 5.4 Effect of UV (18W) irradiation on photocatalytic oxidation of As^{III} to As^{V} after adsorption on the surface of TiO_2/Fe_2O_3 binary mixed oxides (1:1 mass ratio). XANES spectra of the surface of: (A) CP-, (C) MB- and (E) SG-TiO_2/Fe_2O_3 binary mixed oxides with 6 h of UV(18W) irradiation. XANES spectra of the surface after exposure to synchrotron beam on the same samples to confirm the peak of As^{V} on (B) CP, (D) MB and (F) SG……...137

Figure 5.5 Effect of synchrotron radiation on the photocatalytic oxidation of As^{III} on the surface of TiO_2/Fe_2O_3 binary mixed oxides. XANES spectra of arsenic on the surface of (A) CP, (C) MB and (E) SG TiO_2/Fe_2O_3 binary mixed oxides within 45 minutes. Panel B, D and F show the corresponding conversion of percentage As^{III} to percentage As^{V}……139

Figure 5.6 Investigation of the photocatalytic oxidation of As^{III} in aqueous solution using 2g of MB in the tea-bag (50 mM borate buffer pH 9), (A) Schematic representation of the experimental set up using the binary mixed

oxides packed in a tea-bag and subsequently placed into the photo reactor, (B) XANES spectra and K-edge of As^{III} of the system at different time intervals; (C) Calculated percentage As^{III} and percentage As^{V} in solution……..140

Figure 5.7 Photocatalytic oxidation of As^{III} in aqueous solution at pH 5 using 2g of MB placed in a tea-bag with a small hole to let MB diffuse through the solution during synchrotron beam irradiation. XANES spectra at K-edge of arsenic at different time intervals. (A) The MB tea-bag set up in photo-reactor was cut; (B) XANES spectra at start of experiment and after adsorption has occurred 15 min later; (C) Overlay of arsenic XANES spectra; (D) Percentage of As^{III} and As^{V} on the surface of binary mixed oxides ……...142

Figure 5.8 Progress of the photocatalytic oxidation of As^{III} in solution with 2 g of TiO_2/Fe_2O_3 binary mixed oxides suspended and using synchrotron beam irradiation, XANES K-edge spectra for: (A) CP, (B) MB and (C) SG at pH 5 (50 mM acetate buffer), and (D) CP, (B) MB and (F) SG at pH 9 (50 mM borate buffer). Panel (G) compares the percentage of As^{V} formed using CP, MB and SG (pH 9) after 7.5 min……...144

Figure 5.9 Irradiation of As^{III} solution using a UV 18 W lamp in the absence of MB (50 mM HEPES buffer pH 7)…….145

Figure 5.10 Photocatalytic oxidation of As^{III} with mesoporous TiO_2/Fe_2O_3 binary mixed oxide (MB) suspended in 50 mM HEPES buffer at pH 7 with UV 18 watt irradiation…….146

Figure 5.11 Concentration of As^{V} formed from photocatalytic oxidation of As^{III} after 24 and 48 hours using mesoporous TiO_2/Fe_2O_3 binary mixed oxide (MB) suspension in 50 mM HEPES buffer pH 7 using UV 18W irradiation……...147

Figure 5.12 Effect of added hydroxyl radical scavenger (salicylic acid) on photocatalytic oxidation of As^{III} in aqueous solution using binary mixed oxides. The mass ratio of binary mixed oxides to salicylic acid is 1. Oxidation using: as radiation (A) UV18 W irradiation; (B) synchrotron beam……148

Figure 5.13 (A) Photocatalytic oxidation kinetics of As^{III} using the synchrotron irradiation on the surface of CP, MB and SG, and (B) corresponding pseudo-first order model plots. (C) Photocatalytic oxidation kinetics of As^{III} using UV18 watt irradiation on the surface of MB; and (D) corresponding pseudo-first order model plots. (E) The effect of hydroxyl radical scavenger on the photocatalytic

oxidation of As^{III} to using MB suspension with UV 18 watt irradiation is also shown……151

Figure 5.14 (A) Comparison of photocatalytic oxidation rate constant (k_{ox}) on the solid surface of CP, MB and SG using synchrotron irradiation, and (B) on the solid surface of MB using synchrotron irradiation and MB suspension using UV 18 watt……..152

Figure 5.15 Time profiles of As^{V} products from As^{III} photocatalytic oxidation using MB suspension with UV 18 watt irradiation, (A) Concentration of As^{V} at different times, (B) kinetic calculation plots for medium rate 0-30 min and (C) overall rate 0-600 min……...154

Figure 5.16 Schematic representation of the photoreactor used in this work. The binary mixed oxides used was MB, contained in a quartz tube and irradiated with a UV 125 watt lamp. The reactor was placed inside a black metal box……155

Figure 5.17 Photocatalytic oxidation of As^{III} to As^{V} in aqueous solutions using MB suspension (1.0 g L^{-1}) with UV 125 watt irradiation in 50 mM HEPES buffer pH 7: the photocatalytic oxidation reaction was carried out in quartz tube and photo reactor. (A) Arsenic concentration at different reaction times: (B) Photo-oxidation over time with and without MB (The standard deviations were calculated from three replications of experiments)……...156

Figure 5.18 Percentages of As^{V} products in solutions by photocatalytic oxidation using MB suspension with UV lamp 18 and 125 watt reactors within 6 h irradiation times……158

List of Tables

Table 1.1 Adsorption capacities of arsenic on different metal oxides calculated using Langmuir or Freundlich models……34

Table 1.2 Photocatalytic oxidation efficiency of As^{III} to As^{V} using TiO_2 (Degussa P25) reported by Guan et al., [69]……43

Table 2.1 Voltammetric parameters for As^{III} and As^{V} analysis by SWASV using a vibrating gold microwire electrodes with background subtraction (BGS)…...57

Table 3.1 Summary of mixed Ti and Fe oxide material synthetic methods…….69

Table 3.2 BET surface area and pore size of mesoporous TiO_2, Fe_2O_3 and mesoporous TiO_2/Fe_2O_3 binary mixed oxides ……75

Table 3.3 The Langmuir and Freundlich parameters for As^{III} adsorption isotherms on mesoporous TiO_2/Fe_2O_3 binary mixed oxides in 0.01 M acetate buffer pH 5, 0.01 M HEPES buffer pH 7 and 0.01 M borate buffer pH 9 at temp. 25 ^{o}C (298K) (BET surface area of MB = 63.1 m^2 g^{-1})……..79

Table 3.4 Surface active site of MB theoretical calculation by using hematite as reference model [60]……83

Table 3.5 MB surface active sites calculated from the Langmuir adsorption capacities……84

Table 3.6 The kinetic parameters of 40 mg L^{-1} As^{III} adsorption on 1 g L^{-1} MB in 0.01 M HEPES buffer pH 7 at 25ºC (298 K)……...88

Table 3.7 Intra-particle diffusion kinetic model parameters of 40 mg L^{-1} As^{III} adsorption on 1 g L^{-1} MB in 0.01 M HEPES buffer pH 7 at 25ºC……90

Table 3.8 The optimum conditions for arsenic removal from aqueous solutions by using MB column with continuous flow system……96

Table 4.1 The interatomic distances and surface complexes of arsenic on Fe or Ti metal oxides……..106

Table 4.2 Arsenic K-edge EXAFS fitting parameters for As^{III} and As^{V} adsorbed on TiO_2/Fe_2O_3 binary mixed oxides ……113

Table 5.1 Summary of previously reported photocatalytic methods to oxidize arsenic(III)……132

Table 5.2 Photocatalytic oxidation rate constants for As^{III} calculated from experimental data……..154

Table 5.3 Summary of reactor designs for photocatalytic oxidation studies…..156

List of Schemes

Scheme 1.1 Sol-gel synthetic process of metal oxides [48]…….28

Scheme 1.2 Synthetic process for mesoporous TiO_2. Figure taken from Liu et al., [49]…….29

Scheme 1.3 Co-precipitation synthetic process for TiO_2/Fe_2O_3 binary mixed oxides, Figure taken from D'Arcy et al., [50]……..30

Scheme 1.4 Process of As^{III} photocatalytic oxidation on the surface of TiO_2 with UV irradiation, Figure taken from Guan et al., [16]…….41

List of Abbreviations

CP = Co-precipiated TiO_2/Fe_2O_3 binary mixed oxides

MB = Mesoporous TiO_2/Fe_2O_3 binary mixed oxides

MT = Mesoporous TiO_2

MMTC = Mesoporous Fe-Ce bimetal oxides

SG = Sol-gel TiO_2/Fe_2O_3 binary mixed oxides

XRD = X-ray diffraction spectroscopy

SEM = Scanning electron microscopy

BET = Brunauer-Emmett-Teller method

CV = Cyclic voltammetry

ASV = Anodic stripping voltammetry

CSV = Cathodic stripping voltammetry

SWASV = Square wave anodic stripping voltammetry

XAS = X-ray absorption spectroscopy

EXAFS = Extended X-ray absorption fine structure

XANES = X-ray absorption near edge structure

IDP = Intra-particle diffusion model

^1V = Monodentate mononuclear corner sharing complex

^2C = Bidentate binuclear corner sharing complex

^2E = Bidentate mononuclear edge sharing complex

AAS = Atomic absorption spectrometry

HG-AAS = Hydride generation atomic absorption spectrometry

ICP-AES = Inductively couple plasma atomic emission spectrometry

ICP-MS = Inductively couple plasma mass spectrometry

XRF = X-ray fluorescence spectroscopy

NAA = Neutron activation analysis

CE = Capillary electrophoresis

Chapter 1
Introduction

1.1 Background

1.1.1 Global contamination of ground water with arsenic

Millions of people in different parts of the world such as USA, China, Chile, Bangladesh, Taiwan, Mexico, Argentina, Poland, Canada, Hungary, Japan and India are at risk of drinking arsenic contaminated water (Figure 1.1). Since the accumulation of arsenic in the human body can severely affect people's health [1] arsenic contamination in water is a global problem which needs to be addressed.

Natural sources of arsenic in the environment include volcanic emissions to the atmosphere; release of hot volcanic spring waters, weathering of rocks enriched with arsenopyrites and associated soil runoff process. In addition, arsenic can also be released to the environment as a consequence of human activities such as mining, smelting, combustion of fossil fuels and the use of arsenic compounds such as disodium methylarsonate (DSMA), monosodium methylarsonate (MSMA), monomethylarsenic acid (MMAA), dimethylarsenic acid (DMAA), arsenic acid and phenylarsonates in agricultural pesticides, herbicides and animal feed additives [2]. Arsenic contamination is a global problem and removing this contaminant from water supplies has become a major challenge [3].

Consumption of arsenic contaminated water may cause thickening and discoloration of the skin, lesions, stomach pain, nausea, vomiting, diarrhea, numbness in hands and feet, partial paralysis and blindness [4]. The International Agency for Research on Cancer (IARC) has determined that inorganic arsenic is

carcinogenic to humans [6] and the United States Environmental Protection Agency (USEPA) has classified inorganic arsenic as a known human carcinogen [7]. Arsenic intake has been reported to increase the risk of cancer in the liver, lungs, skin, bladder, and kidneys [5]. In order to reduce the health risks associated with arsenic, the World Health Organization (WHO) recommended in 2001 a maximum concentration of 10 µg L^{-1} of arsenic as the drinking water standard [8].

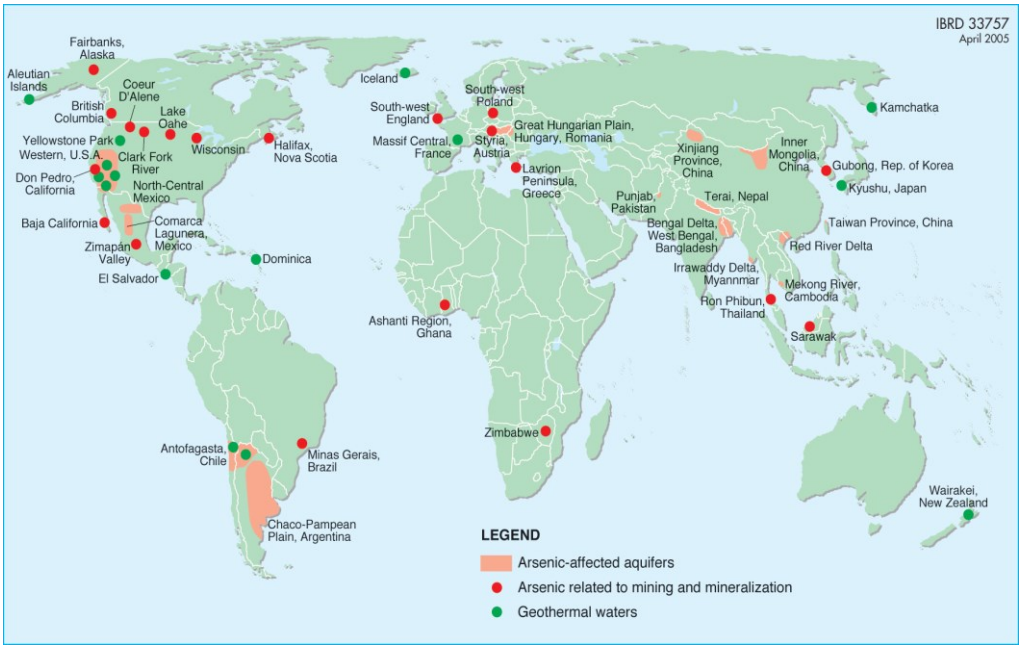


Figure 1.1 *Areas of arsenic contamination in groundwater including both natural and anthropogenic sources, Figure taken from Smedley and Kinniburgh* [9]

Arsenic contaminated water is odourless, colourless and tasteless and therefore people are unaware of the dangers when drinking this water [10]. High concentration of arsenic in ground water have been found in USA, China, Chile, Bangladesh, Taiwan, Mexico, Argentina, Poland, Canada, Hungary, Japan and India. Additionally, Bangaladesh and West Bengal in India are the areas that largest population is at risk of cosuming arsenic contaminated water [1] while

China, it is reported that 20 million are at risk of arsenic exposure through drinking water [11]. In developed countries including USA, there is also a serious arsenic contamination problem and more than 3 million people receive arsenic into their bodies by drinking contaminated water from their private wells which are difficult to test and remediate [10]. The ground waters in UK have also found the contamination of arsenic in some areas [12]. For example, the report from the British Geological Survey (BGS) and Public Health England in Cornwall found the high arsenic concentration across this region [13].

1.1.2 Speciation of arsenic

The main arsenic species present in natural waters are arsenate (oxidation state V) and arsenite (oxidation state III) oxy-anions [14]. The most common forms of arsenic (V) in the environment are arsenate (AsO_4^{3-}), hydrogen arsenate ($HAsO_4^{2-}$) and dihydrogen arsenate ($H_2AsO_4^-$) anions [15]. On the other hand, arsenite is mainly found as the neutral species H_3AsO_3 at pH below 9. Arsenic speciation at different pH ranges are shown in Figure 1.2.

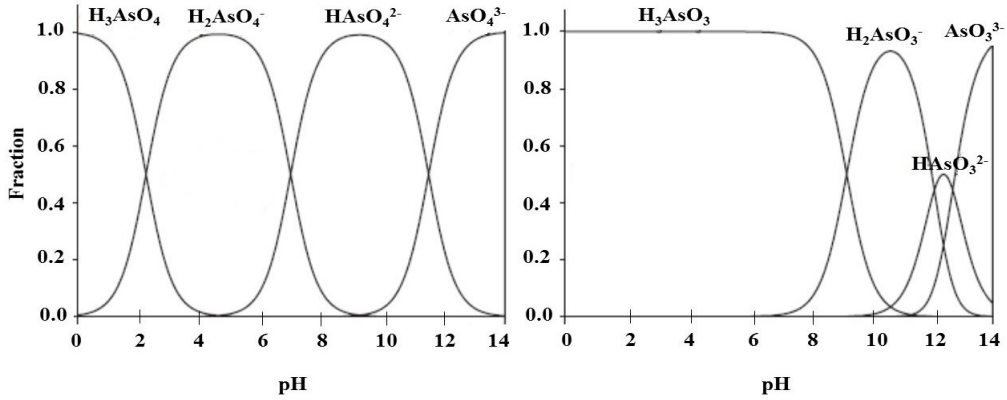


Figure 1.2 *Distribution of arsenic species as a function of pH, Figure taken from Guan et al., [16].*

In Nature, arsenic is either found bound onto iron oxide surfaces or can be incorporated within mineral structures. Therefore, it can be desorbed from the mineral surfaces and released into ground water [17].

1.1.3 Current arsenic removal techniques

A variety of arsenic removal methods have been investigated and implemented, including coagulation/filtration, membrane techniques including reverse osmosis, adsorption and ion-exchange. These methods have been reviewed and their relative advantages/disadvantages discussed by Mondal et al., [17], Garelick et al., [18], Ng et al., [19], Choong et al., [20], Mohan et al., [21] and Jain et al., [22]. An overview of the different techniques for arsenic removal is provided in the following sections. For a more exhaustive discussion, the reader is referred to the reviews indicated above.

1.1.3.1 Coagulation and Precipitation

Coagulation is an effective method for arsenic treatment in which chemicals such as $Al_2(SO_4)_3$, $Fe_2(SO_4)_3$, $FeCl_3$, and $Ca(OH)_2$ can be used as coagulating agents [23] . These agents can dissolve into water by stirring for short period of time. After that, all micro-particles and negatively charged ions are attached to the floc by electrostatic force and coagulate. The efficient removal of arsenic by coagulation method is controlled by pH and the amount of coagulating agent. For example, arsenic coagulation by $FeCl_3$ works at pH below 8 while with $Al_2(SO_4)_3$ the optimal pH to remove arsenic in between 6 and 8 [18, 23]. Coagulation using $Al_2(SO_4)_3$ is effective below pH 7. Therefore, it is essential to lower the pH of the water samples before treatment and then adjust pH of the treated water to a suitable value for consumption. On the other hand, coagulation with $Fe_2(SO_4)_3$ or $FeCl_3$ is not affected by pH and required less pre-treatment steps of the water

samples [25]. $FeCl_3$ at the concentration 20 mg L^{-1} could bring down As^V concentration below 30 µg L^{-1} from an initial concentration of 1,000 µg L^{-1}[25]. This results from the higher stability of iron hydroxides as compared to aluminum hydroxides around natural pH [22]. $Fe_2(SO_4)_3$ precipitation has also been used successfully as a coagulating agent to remove arsenic from contaminated ground water [26].

On the other hand, precipitation process is based on the formation of insoluble arsenic compounds. For example, arsenic dissolved in water can form calcium arsenate which due to its low solubility in water, precipitates and hence can be removed by filtration.

Coagulation and precipitation methods are sometimes unable to effectively remove arsenic at trace levels which is the limitation of these techniques.

These methods remove As^V more effectively than As^{III} since the former is found as negatively charged species at a wide pH range while the later is mainly found as neutrals species below pH 9 (see section 1.1.2). Therefore, pre-oxidation of As^{III} to As^V, by using chlorine or other oxidizing agents, is often necessary. However, a disadvantage of this step is that some of the oxidizing chemical used can generate toxic byproducts [24].

1.1.3.2 Methods based on membrane technology

Membranes have been used to remove arsenic from contaminated water in a range of different methods. There are two different types of membranes which have been used: (i) low-pressure membrane techniques such as microfiltration and ultrafiltration and (ii) high-pressure membrane techniques such as nanofiltration and reverse osmosis. Methods based on membranes are independent of pH for arsenic removal. However, in some cases water samples contain high concentration of suspended solids which makes the membrane clog.

Therefore, membrane methods often requires a sample pre-treatment step before removal of arsenic [19, 22, 25]. The maintenance of fouling membranes can bring lots of cost to the removal process. The development of a hybrid-membrane system using the reverse osmosis-coagulation combine method can improve the membrane decompose rate [19].

1.1.3.3 Methods based on adsorption onto metal oxides

Arsenic oxides can be removed from contaminated water by adsorbing them onto the surface of suitable materials such as metal oxides. Adsorption is the most cost-effective method for arsenic removal [23], and therefore these methods have been implemented at various treatment plants. As discussed in the previous section, arsenic(V) is mainly present in ground waters as charged species ($H_2AsO_4^-$ and $HAsO_4^{2-}$) and therefore it is more readily adsorbed than arsenic(III) which is found as the neutral H_3AsO_3 compound.

As^{III} is significantly more toxic and more mobile than As^V. It is also more difficult to remove by conventional treatment methods such as chemical precipitation [20, 27], adsorption onto iron-oxide coated sand [21], flotation [27] and filtration [20]. Therefore, most separation techniques require pre-oxidation of As^{III} to As^V for effective arsenic removal, causing added complexity [28, 29].

Titanium dioxide (TiO_2) is of particular interest because of its good adsorption capacity, physical and chemical stability, non-toxicity, resistance to corrosion, commercial availability and inexpensiveness [30-33]. TiO_2 has three polymorphs (i.e. anatase, rutile, and brookite). Recent work showed that anatase (99% pure) can adsorb 22.5 mg g^{-1} of As^V [34] and the capacity for As^V for a mixture of 70% anatase and 30% rutile has been reported 8.01 mg g^{-1} [35].

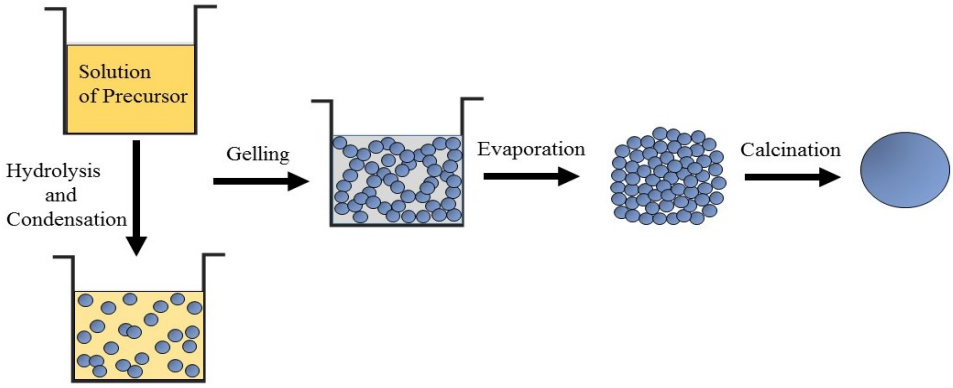
Iron oxides are often very effective in removing arsenic from water. The compound may be synthesized [36] or collected from rocks, sediments, or soils [37].

As discussed in previous sections, the removal of arsenic(III) from contaminated water by adsorption methods is more challenging than for arsenic(V). Therefore, several pre-treatment methods have been investigated to convert arsenic(III) to arsenic(V). One such method is based on photocatalytic oxidation of As^{III} to As^{V} using a TiO_2 photocatalyst to improve the removal efficiency [38-41] (see section 1.4).

1.2 Synthesis of metal oxides

1.2.1 Synthesis of TiO_2

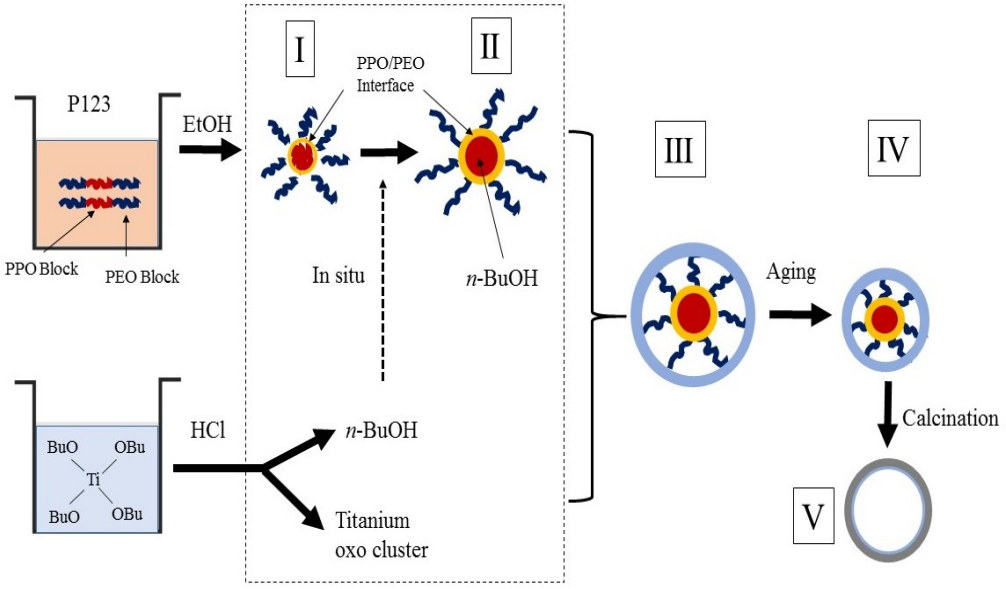
This section provides an overview of sol-gel techniques to prepare TiO_2 [42-48]. The sol-gel process can briefly be defined as the transformation of a precursor solution into an inorganic solid using polymerization reactions induced by water. The general process of sol-gel is shown in Scheme 1.1. The first step in the sol-gel process is the formation of an inorganic polymer by using hydrolysis and condensation reactions such as the conversion of the molecular precursor into a high crosslinked solid. A sol, i.e. a dispersion of colloidal particle in a liquid, is first formed by hydrolysis reaction. This developes a gel, which yields an interconnected, rigid and porous inorganic network enclosing a continuous liquid phase [48].



Scheme 1.1 *Sol-gel synthetic process of metal oxides [48]*

Metal alkoxides such as tetraethyl orthotitanate (TEOT) [43, 44] and titanium isoproxide [45] are used as precursors and frequently used to form TiO_2 gel. This method is simple, non-hazardous [46], cost effective with low process requirements [47]. Moreover, this method generally yields products with high purity and homogeneity [48].

Large-pore mesoporous materials have attracted much attention because of their potential applications in speciation, catalysis, medical implants and shape-selective heterojunctions. To increase the utility of mesoporous TiO_2 materials, it is necessary to prepare large-pore meso-nc-TiO_2. The synthesis of mesoporous TiO_2 using Pluronic (P123)-alcohol-water system can produce TiO_2 with pore size of about 10 nm which can support the photocatalytic properties [48]. The materials exhibit a good host porous structure to form a novel heterojunction through growth of a variety of wide band-gap semiconductors and assembling functional polymers, noble metals, carbon nanotubes, and other components in the large mesopore channels, which could be useful for the development of improved efficiency in solar cells, sensors, and photocatalytic applications [49]. The mesoporous TiO_2 synthetic method reported by Liu et al., [48] is shown in Scheme 1.2.



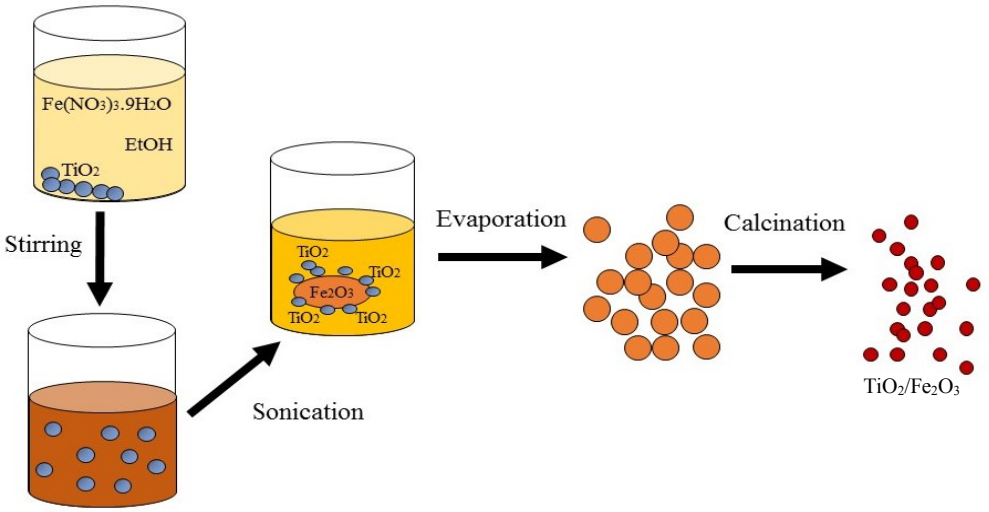
Scheme 1.2 *Synthetic process for mesoporous TiO_2. Figure taken from Liu et al., [48]*

1.2.2 Synthesis of TiO_2/Fe_2O_3 bicomposites

In recent years, various synthetic methods for producing mixed Ti and Fe oxides have been reported in the literature [41, 49, 50, 51]. These mixed oxides have been applied to the study of photocatalytic oxidation [49] and adsorption processes [50]. The synthesis of mixed oxides by doping Fe_2O_3 into TiO_2 can improve photocatalytic property of TiO_2 [52]. The source of Ti and Fe in binary mixed metal oxides have been utilized including titanium tetra-isopropoxide [42, 51], titanium IV tetra-tert-butoxide [52] and powdered TiO_2 anatase as Ti pre-cursors [51] and iron nitrate [51], Fe^{III} acetylacetonate [42] and $Fe^{II/III}$ chloride as Fe pre-cursor materials [52]. Additionally, the processes of hydrothermal deposition [51, 52], impregnation [42, 51] and sol-hydrolysis [52] have been adapted to improve the distribution of $Fe^{II/III}$ into the TiO_2 lattice. Impregnation is facile and inexpensive [51].

The development of TiO_2 and Fe_2O_3 phases depends on parameters including the synthetic method used, calcination temperature and relative ratio of Ti and Fe oxides. Calcination temperatures of Fe:Ti (1:1 ratio) mixtures at 700ºC and 900ºC, lead to the information of rutile and of pseudo-brookite (Fe_2TiO_5) due to the diffusion of Fe^{III} into TiO_2 at higher temperature [42] whereas only amorphous anatase and traces of rutile were found at calcination temperature of 500ºC [42].

Several synthetic methods for Ti and Fe mixed oxides have been previously reported [49, 50]. One of the most employed methods to synthesize mixed oxides of Ti and Fe is co-precipitation. The co-precipiation technique is related to the dissolving of a salt precursor such as a chloride, oxychloride or nitrate. The precipitation of corresponding metal hydroxides is occurred during addition of base solution such as sodium hydroxide or ammonium hydroxide solution. The residues are then washed and calcined to obtain the final products. This preparation method is effective for synthesis of metal oxide composites. The synthetic steps are shown in Scheme 1.3.



Scheme 1.3 *Co-precipitation synthetic process for TiO_2/Fe_2O_3 bicomposites, Figure taken from D'Arcy et al., [50]*

The synthesis of TiO_2/Fe_2O_3 bicomposites using co-precipitation method was reported by D'Arcy et al., [50]. They used commercial TiO_2 anatase co-precipitated with Fe_2O_3 in ethanol and calcined at 300^oC for 6 hours. The synthetic process can produce bicomposites with the large surface areas of approximately 41.7 m^2 g^{-1}. These bicomposites were applied to study the adsorption mechanism of As^V from aqueous solution.

1.3 Adsorption mechanism of arsenic onto metal oxides

Adsorption modifies the electrostatic properties of suspended particles, the reactivity of solid surfaces and the rate of reactions on the particles surface [53]. Adsorption can be divided into physisorption and chemisorption. Physisorption occurs when the adsorbent interacts via weak electrostatic forces with the adsorbent's surface active sites [54]. Chemisorption on the other hand involves the formation of chemical bonds (either ionic or covalent) between the adsorbate and adsorbent's surface active sites. The mechanism of arsenic adsorption onto the surface of metal oxides can be described by isotherm models (see section 1.31) which can indicate arsenic adsorption on the surface as being monolayer or multilayer. In addition, the formation of monolayer on the metal surface can indicate the binding by chemisorption and the formation of multilayer could be the binding in the form of physisorption [54].

The point of zero charge (PZC) of an adsorbent is where the surface of materials is not charged and that occurs at different pH values depending on material [53]. At pH values below the PZC, the surface charge of adsorbent is positive as acidic solution donates more protons than hydroxyl groups. On the other hand, at pH values higher than the PZC, the surface charge of the adsorbent is negatively charged. Therefore, the knowledge of PZC of adsorbents is important for the design of an effective adsorption process for a given application.

1.3.1 Adsorption isotherms

Arsenic adsorption mechanism on metal oxides have been studied using adsorption isotherm models including the Langmuir and Freundlich models, which can identify the adsorption layer on the surface of the metal oxides [41, 50]. The Langmuir model describes the formation of monolayers on the surface of metal oxides with the limitation of surface active sites [41, 50]. The Freundlich isotherm model defines that arsenic can form adsorption multilayer of arsenic on the surface of metal oxides with unlimited surface active sites [41, 50].

Arsenic adsorption mechanism on metal oxides including TiO_2 [55, 56], Fe oxides [57] and mixed oxides [41, 49, 50] has been examined using the Langmuir and Freundlich models. A summary of the adsorption studies previously reported in the literature for TiO_2 [55, 56], Fe_2O_3 [56-58] or mixed oxides including $MnFe_2O_4$ [58], iron oxides [57], nanostructured Fe(III)-Ti(IV) binary mixed oxides [41], co-precipitated TiO_2/Fe_2O_3 bicomposites [50], mesoporous TiO_2/Fe_2O_3 bicomposites [49] are shown in Table 1.1. The adsorption mechanism of arsenic onto these materials has been rationalized using Langmuir models [41,50]. However, in some cases, it has been found that the Freundlich model is better at explaining the arsenic adsorption mechanism onto TiO_2 nanopowder [56] and Fe_2O_3 nanopowder [56]. These results from the literature (see Table 1.1) can be used to conclude that arsenic can possibly form adsorption monolayer onto the surface of metal oxides. Additionally, investigations of arsenic adsorption mechanism onto TiO_2 have been reported by Dutta et al., [35], Bang et al., [8], Xu et al., [34] and Pirila et al., [30]. The adsorption mechanism of As^{III} and As^{V} reported in previous works [8, 30, 34, 35] indicated that arsenic form monolayer on the surface of TiO_2. Moreover, the Langmuir model can well describe the adsorption mechanism of arsenic on Fe oxides including magnetite [59] and goethite [59]. These works conclude that arsenic can also form a monolayer on the surface of Fe oxides. Finally, a similar adsorption mechanism

was also found for arsenic adsorption onto the surface of mixed TiO_2/Fe_2O_3 reported by Gupta and Ghosh [41] and D'Arcy et al., [50].

To investigate the effect of pH on adsorption capacities (see Table 1.1), Zhang et al., [58] compared the adsorption capacities of arsenic on Fe oxides at pH 3 and 7. They found that the adsorption capacities of As^{III} and As^{V} at pH 3 higher than that at pH 7. Additionally, the adsorption capacities of As^{V} on co-precipitated TiO_2/Fe_2O_3 bicomposites at pH 5, 7, 9 were investigates and compared (see Table 1.1) by D'Arcy et al., [50]. They found that the adsorption capacity of As^{V} at pH 3 is highest comparing with pH 7 and 9. These results of adsorption capacities at low pH (pH 3 and 5) reported by Zhang et al., [58] and D'Arcy et al., [50] indicate that at lower pH (pH 3 and 5) arsenic can adsorb better than higher pH (pH 7 and 9).

Table 1.1 *Adsorption capacities of arsenic on different metal oxides calculated using Langmuir or Freundlich models.*

Adsorbent	pH	Surface Area (m^2 g^{-1})	Temp. (^oC)	Model Tested	As^{III} capacity (mg g^{-1})	As^{V} capacity (mg g^{-1})	Ref.
TiO_2	7.0	330	25	Langmuir	59.93	37.46	[16]
TiO_2(Degussa P25)	4.0	55	22	Langmuir	3.45	4.65	[16]
Goethite	9.0	39	22	-	28	7	[16]
TiO_2	7.0	251	25	Langmuir	32.4	41	[16]
Ferrihydrite	7.0	-	-	Langmuir	-	68.75	[16]
Goethite	7.0	-	-	Langmuir	-	442.8	[16]
Goethite	-	39	-	-	-	4	[57]
Hematite	-	14.14	-	-	-	0.2	[57]
Nanocrystalline TiO_2	7.0	-	-	Langmuir	0.8 mmol/g	0.5 mmol/g	[55]
TiO_2 nanopowder	6.7	190-290	-	Freundlich	-	12.09	[56]
Fe_2O_3 Nanopowder	6.7	50-245	-	Freundlich	-	5.64	[56]
Fe_3O_4	3.0 (As^V)	102	25	Langmuir	49.8	44.1	[58]
	7.0 (As^{III})	102	25	Freundlich	15.2	19.2	[58]
$MnFe_2O_4$	3.0 (As^V)	138	25	Langmuir	93.8	94.6	[58]
	7.0 (As^{III})	138	25	Freundlich	29.6	59.7	[58]
$CoFe_2O_4$	3.0 (As^V)	101	25	Langmuir	100.3	73.8	[58]
	7.0 (As^{III})	101	25	Freundlich	36.9	49.4	[58]
Iron oxide loaded sand	4.5	-	25	Langmuir	110	85	[16]
Manganese oxide loaded sand	4.5	-	25	Langmuir	36	35	[16]
Iron sand	4.5	-	25	Langmuir	5	55	[16]

Table 1.1 (Continued) *Adsorption capacities of arsenic on different metal oxides calculated using Langmuir or Freundlich models.*

Adsorbent	pH	Surface Area (m^2 g^{-1})	Temp. (^oC)	Model Tested	As^{III} capacity (mg g^{-1})	As^{V} capacity (mg g^{-1})	Ref.
Iron oxide nanoparticle on alumina supports	6.5	30	-	-	-	3.16	[57]
Nanostructure iron(III)-Titanium(IV) mixed oxide	7.0	-	-	Langmuir	85	14	[41]
Co-precipitated TiO_2/Fe_2O_3 bicomposites	5,7,9	41.7	25	Langmuir	-	12.14 (pH5) 7.79 (pH7) 6.48 (pH9)	[50]
Mesoporous TiO_2/Fe_2O_3 bicomposites	3,7,9	95	25	-	-	-	[49]

1.3.2 Adsorption kinetics of arsenic on metal oxides

The kinetics studies of arsenic adsorption on mixed TiO_2/Fe_2O_3 have been previously reported by Gupta and Ghosh [41] and D'Arcy et al [50]. The kinetic models including pseudo-first and second order have been used to determine the adsorption kinetic rate of arsenic on these materials.

Gupta and Ghosh [41], indicated that As^{III} adsorption onto the surface of nanostructure TiO_2/Fe_2O_3 binary oxides was reach equilibrium within 3.5 h faster than that of As^{V} which needed 6.0 h to equilibrate. D'Arcy et al., applied both models to study adsorption kinetic of As^{V} on co-precipitated TiO_2/Fe_2O_3 bicomposites and concluded that a pseudo-second order rate model is suitable for a good approximation of adsorption rates on the surface of the bicomposites. The

results found in D'Arcy's work [50] agree with the reports by Gupta and Ghosh [41].

1.3.3 Geometry of arsenic complex onto the surface of iron oxides and TiO_2

The molecular structure of arsenate and arsenite on the surface of various Fe and Ti oxides have been studied and reported in previous works [60-71] including ferrihydrite ($Fe_2O_3.0.5H_2O$) [61], goethite (α-FeO(OH)) [62], hematite (Fe_2O_3) [65], lepidocrocite (γ-FeO(OH)), [65] and anatase [66]. The geometries of arsenate and arsenite adsorption on various types of iron oxides [61, 62, 65] and titanium dioxide [66] found in different types of surface complexes are shown in Figure 1.3.

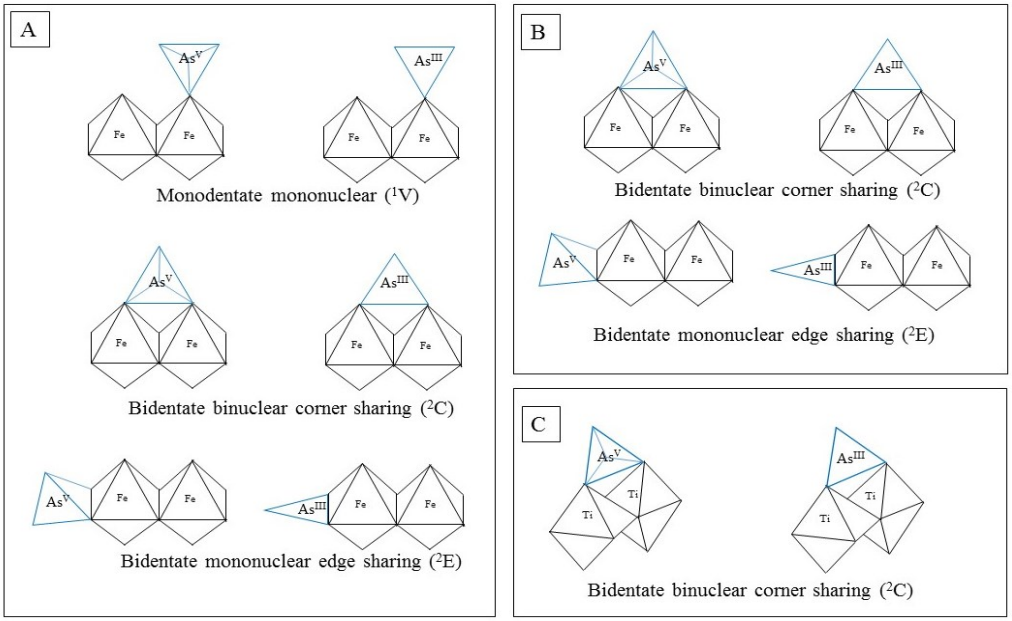


Figure 1.3 *The possible geometries of arsenate and arsenite on the surface of iron oxides and TiO_2, (A) goethite and lepidocrocite found similar geometries [61, 62, 63, 65], (B) ferrihydrite and hematite found similar geometries [61, 65], (C) anatase found only one geometric type [66]*

Arsenate binding modes on the surface of scorodite, goethite, lepidocrocite, hematite, ferrihydrite were described first by Sherman and Simon [61] using extended X-ray adsorption fine structure spectroscopy (EXAFS). The study showed that tetrahedral As^{V} is likely to bind as a bidentate binuclear corner sharing (^{2}C) complex, bidentate mononuclear edge sharing (^{2}E) complex on the surface of scorodite, goethite, lepidocrocite, hematite, ferrihydrite [61]. Additionally, the binding mode as a monodentate mononuclear corner sharing (^{1}V) complex were found only onto the surfaces of goethite and lepidocrocite [61].

Fendrof and co-workers [62] used EXAFS to study the molecular structure of As^{V} on the surface of goethite and found that it binds as a bidentate binuclear corner sharing (^{2}C) complex with As^{V}-Fe interatomic distance around 3.59 Å and as a bidentate mononuclear edge (^{2}E) sharing complex with As^{V}-Fe interatomic distance around 2.85 Å.

Manning et al., [63] reported a spectroscopic evidence of As^{III} adsorption on the surface of goethite. EXAFS spectra showed an average As^{III}-Fe interatomic distance of around 3.38±0.01 Å which is consistent with a bidentate binuclear corner sharing (^{2}C) complex of As^{III} on the surface of goethite by inner-sphere adsorption.

The geometry of adsorbed As^{III} and As^{V} complexes on the surface of iron oxides such as lepidocrocite, magnetite and/or maghemite were reported by Manning et al., [64]. EXAFS analysis show interatomic distances of As-Fe around 3.30-3.36 Å which are attributed to bidentate binuclear corner sharing (^{2}C) complexes.

Ona-Nguema et al., [65] described adsorption complex of As^{III} onto the surfaces of ferrihydrite, hematite, goethite and lepidrocrocite. EXAFS studies indicated that As^{III} form bidentate mononuclear edge sharing (^{2}E) complexes on ferrihydrite with As^{III}-Fe interatomic distance of 2.90±0.05 Å and bidentate binuclear corner sharing (^{2}C) surface complexes on hematite with As^{III}-Fe

interatomic distance of 3.35±0.05 Å. These surface complexes are found under high and low surface coverage adsorption conditions. Furthermore, As^{III} form bidentate binuclear corner sharing (^2C) surface complexes on goethite and lepidocrocite with As^{III}-Fe distances of around 3.3-3.4 Å and form minor amount of monodentate mononuclear corner sharing (^1V) complex with As^{III}-Fe interatomic distance around 3.6 Å.

The geometry of As^{III} and As^{V} adsorption complex on the surface of Fe oxides were described in the works of Morine et al., [68], Guan et al., [69], and Jönsson et al., [70] and found that As^{III} adsorption on maghemite has two types of surface complexes including bidentate mononuclear edge sharing (^2E) complex with As^{III}-Fe interatomic distance around 2.90±0.03Å. As^{V} complex system on the surface of maghemite binds as a bidentate binuclear corner sharing (^2C) complex with As^{V}-Fe interatomic distance of 3.35±0.03 Å [68]. Bidentate binuclear corner sharing (^2C) complexes are formed during the adsorption of As^{V} onto the surface of granular ferric hydroxide with interatomic distance of As^{V}-Fe 3.32 Å [69].

Jönsson et al., [70] studied As^{V} and As^{III} adsorption complexes on fougerite, magnetite and siderite. As^{V} adsorption on these minerals form inner sphere surface complex with bidentate binuclear corner sharing (^2C) complex between AsO_4 tetrahedral and FeO_6 octahedral with As^{V}-Fe interatomic distances around 3.43, 3.42 and 3.36 Å for fouherite, magnetite and siderite. As^{III} adsorption on magnetite and fougerite surfaces form inner sphere complex with bidentate binuclear corner sharing (^2C) complex with As^{III}-Fe interatomic distances 3.39 and 3.43 Å of interatomic distances for magnetite and ferrihydrite.

The results from previous studies [61-70] present the possible geometry of arsenic adsorbed Fe oxide surface complexes dividing into three different types including bidentate mononuclear edge sharing (^2E) complex (As-Fe 2.8-2.9 Å), bidentate binuclear corner sharing (^2C) complex (As-Fe 3.3-3.4 Å) and surface type of monodentate mononuclear corner sharing (^1V) complex (As-Fe 3.6 Å in some cases).

The adsorption complexes of arsenic on TiO_2 have been also reported in several publications [66, 67, 71]. The EXAFS technique has been utilized to determine interatomic distance of As-Ti which can be used to define the geometry of arsenic-Ti surface complexes.

Pena et al., [66] studied the adsorption complexes of As^{III} and As^{V} on the surfaces of nanocrystalline TiO_2 anatase. EXAFS analysis results were used to specify the geometry of arsenic adsorption on the surface of TiO_2. The results indicate that both As^{III} and As^{V} bind to the TiO_2 surface with bidentate binuclear corner sharing (^2C) complex at interatomic distances around 3.30 and 3.35 Å for As^{V}-Ti and As^{III}-Ti, respectively.

The adsorption of As^{III} and As^{V} on TiO_2 nanoparticles have been studied by Jegadeesan et al., [67]. The geometry of arsenic adsorption complexes on TiO_2 were also investigated using EXAFS analysis and found that both As^{III} and As^{V} form bidentate binuclear corner sharing (^2C) with inner sphere complex on the surface of TiO_2 at As^{III}-Ti and As^{V}-Ti interatomic distances of around 3.33±0.02 and 3.34±0.02 Å, respectively.

Jing et al., [71] reported the removal of arsenic Ti-lanthanide-activated carbon (TLAC) composite and used EXAFS analysis to explain the geometry of arsenic adsorbed TLAC surface complex. The results show an As^{V}-Ti interatomic distance of around 3.34 Å which indicates that As^{V} forms a bidentate binuclear corner sharing (^2C) complex.

In summary, the results discussed herein indicate that both As^{III} and As^{V} form bidentate binuclear corner sharing (^2C) complexes on the surface of TiO_2 with interatomic distances ranging from 3.00-3.35 Å.

The interatomic distances of As-Fe and As-Ti and the geometry of surface complexes from literature can be used to predict and describe the binding mode and structure of arsenic on the surface of TiO_2/Fe_2O_3 binary mixed oxides.

1.4 Photocatalytic oxidation mechanism of As^{III} on TiO_2

The photocatalytic and hydrophilic properties of TiO_2 have been used for degradation of organic pollutants or coating of waterproof materials [72]. The electronic structure has a filled valence band and an empty conduction band [73]. Photon absorption exceeding the band gap energy results in the separation of charge and generates a valence band hole (h_{vb}^{+}) and a conduction band electron (e_{cb}^{-}). The photocatalytic reaction has been reported by Lee et al., [32] which can be presented as shown below.

$$TiO_2 + h\nu \rightarrow e_{cb}^{-} + h_{vb}^{+} \quad (1.1)$$

$$e_{cb}^{-} + h_{vb}^{+} \rightarrow \text{heat} \quad (1.2)$$

$$OH^{-} + h_{vb}^{+} \rightarrow OH^{*} \quad (1.3)$$

$$O_2 + e_{cb}^{-} \rightarrow O_2^{*-} \quad (1.4)$$

where, $h\nu$ is the photon, e_{cb}^{-} is the conduction band electron, h_{vb}^{+} is the valence band hole, $OH^{-}$is the hydroxide ion, OH^{*} is hydroxyl radical, O_2^{*-} is superoxide.

The conduction band electron (e^{-}_{cb}) and the valence band hole (h^{+}_{vb}) can migrate to the surface of the mineral in which they become trapped by hydroxide groups [74]. The recombination of the conduction band electron and the valence band hole occurs when there is a lack of suitable energy scavengers at the surface [73]. If a suitable scavenger is present, such as oxygen, this scavenger acts as the primary electron acceptor producing a superoxide radical (O_2^{*-}) as shown in equation 1.4. This leaves a positive hole in the crystal lattice [75]. To improve photo-efficiency and prevent recombination, both the electrons and holes must have substrates with which to react at the surface [74].

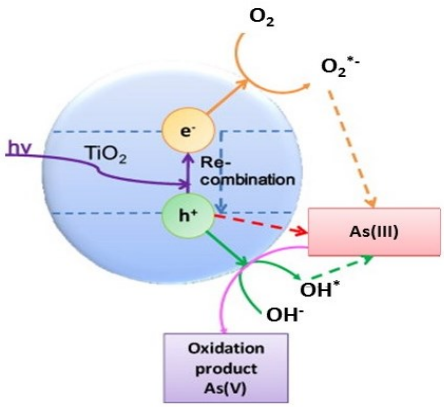
Oxidative species including the weak oxidant, superoxide radical (O_2^{*-}) and strong oxidant, hydroxyl radical (OH^{*}) are the main species involved in the

photocatalytic oxidation reaction. This process takes place on the surface of TiO_2 with UV activation [38].

Studies of the photocatalytic activity of TiO_2 indicate that anatase is a more efficient phase than rutile because it has a wider band gap energy giving a higher driving force for the photo-induced redox reactions but require the presence of UV instead of visible light [72]. Anatase is stable and transforms to rutile at high temperature (500-600^{O}C) [76]. The band gap energy of anatase and rutiles are 3.2 and 3.0 eV, respectively. Anatase has a higher density of localized states, electrons with energies between the conduction and valence band, greater surface area and slower recombination rate that contribute to improved performance [76].

Sunlight contains a mixture of UVA (315-400 nm) and UVB (280-315 nm) light which provides enough energy for the photocatalytic oxidation of As^{III} using TiO_2 [55, 77]. Previous studies showed that the photocatalytic oxidation follows first order kinetics [55, 77].

The photocatalytic oxidation of As^{III} using TiO_2 has been reported by Guan et al., [16] and Lee et al., [32] and is summarized by Scheme 1.4.



Scheme 1.4 *Process of As^{III} photocatalytic oxidation on the surface of TiO_2 with UV irradiation. Figure taken from Guan et al.,* [16]

Effect of TiO_2 crystallite size on As^{III} photocatalytic oxidation was reported by Xu and Meng [84]. They studied crystalline size in between 6.6 and 30.1 nm and found that TiO_2 with the large surface area had a faster rate of As^{III} photocatalytic oxidation.

The effect of pH on As^{III} photocatalytic oxidation using TiO_2 with UV-irradiation has been investigated by Lee and Choi [32]. The initial rate of the reaction at pH 9 was faster than at pH 3 and completed reaction within 2 h of irradiation. This work also found that the presence of humic acid and ferric ion can support the photocatalytic oxidation mechanism. Moreover, Ryu and Choi [80] reported the modification of TiO_2 surface with noble metal such as Pt for As^{III} photocatalytic oxidation and found the modified material facilitates the photocatalytic oxidation reaction by trapping the conduction band electron and consequently retarding the charge-pair recombination. Jayaweera et al., [81] found that the photocatalytic oxidation of As^{III} using TiO_2 suspension with UV irraddiation and air bubbling increased the reaction rate. Ferguson et al., [74] and Yang et al., [78] studied at a range of pH values from 3 to 9 [78] which covers the pH range of groundwater (pH 5-9). Their results showed that the performance of the photocatalytic oxidation reaction was not impacted by pH in the studied system [74, 77].

As^{III} photocatalytic oxidation by TiO_2 was found in range 80-100% with light energy activation around 300 – 400 W [69]. The performance of TiO_2 in As^{III} photocatalytic oxidation from various works have been reported by Guan et al., [69]. The experimental parameters and results were summarized in Table 1.2.

Table 1.2 *Photocatalytic oxidation efficiency of As^{III} to As^{V} using TiO_2 (Degussa P25) reported by* Guan et al., [69]

Catalyst	[Catalyst] ($g\ L^{-1}$)	$[As^{III}]_0$ ($mg\ L^{-1}$)	pH	Light source	Time (min)	% Oxidation	Ref.
TiO_2	2	39.38	9	A 400W mercury arc lamp	30	~100%	[78]
TiO_2	0.01	0.1	5-9	A 1000W Xe arc lamp, λ <320 nm	3.3	>98%	[77]
TiO_2	1.5	3.75	3 or 9	A 300W Xe arc lamp, λ >300 nm	120	~100%	[32]
TiO_2	0.25	100	7	A 250W Xe arc discharge lamp, λ >300 nm	60-90	80%	[81]
TiO_2	0.5	37.5	3	A 300W Xe arc lamp, λ >300 nm	180	>90%	[80]
TiO_2	0.5	37.5	9	A 300W Xe arc lamp, λ >300 nm	180	~77%	[80]
Pt/TiO_2	0.5	37.5	3 or 9	A 300W Xe arc lamp, λ >300 nm	180	~100%	[80]
TiO_2	1	1.0	-	A low pressure mercury lamps, λ = 350 nm	7	~100%	[79]
TiO_2	0.01	7.5	3	A 4 W UV lamp, λ >352 nm	30	~40%	[85]
TiO_2	0.1	3.0	9	A 125 W high pressure mercury vapor, λ = 360 nm	~12.5	~100%	[82]
TiO_2	0.05	0.062	6.3	A 8 W, λ =365 nm UV lamp	10	~100%	[74]
TiO_2	0.05	0.188	6.3	A 8 W, λ =365 nm UV lamp	15	~100%	[74]
TiO_2	0.05	0.622	6.3	A 8 W, λ =365 nm UV lamp	60	~100%	[74]
TiO_2	0.1	5.63	3	A 4 W UV lamp,λ >352 nm	40	~80%	[86]
TiO_2	0.05	5.0	6.4	A 9W Radium lamp, 350< λ<400 nm	10	~100%	[83]

Table 1.2 (Continued) *Photocatalytic oxidation efficiency of As^{III} to As^{V} using TiO_2 (Degussa P25) reported by* Guan et al., [69]

Catalyst	[Catalyst] ($g\ L^{-1}$)	$[As^{III}]_0$ ($mg\ L^{-1}$)	pH	Light source	Time (min)	% Oxidation	Ref.
TiO_2	0.05	10.0	6.4	A 9W Radium lamp, 350< λ<400 nm	30	~100%	[83]
TiO_2	0.05	20.0	6.4	A 9W Radium lamp, 350< λ<400 nm	30	~100%	[83]
TiO_2	0.5	15.0	3	A 300W Xe arc lamp, λ >300 nm	180	~100%	[38]

The photocatalytic oxidation performance of mixed Fe and Ti metal oxides has been studied by various groups. The mixed oxides studied were synthesized using different methods, including Fe doped into TiO_2 [42, 52], mixed Fe_2O_3 and TiO_2 films [41] and mesoporous TiO_2/Fe_2O_3 [49]. Mixed oxides generally showed an improved photocatalytic oxidation of As^{III} compared to TiO_2. The mixed oxides of Ti and Fe were examined in UV-visible irradiation systems and reported completed oxidation reaction at irradiation times between 120 -500 min [42, 52].

The effect of synthetic methods for mixed Ti and Fe oxides synthetic method on photocatalytic oxidation property has been studied by Pal et al., [42] showing that calcination temperature, iron concentration, absence of oxygen and particle size affect photocatalytic properties of TiO_2/Fe_2O_3. Increase in calcination temperature during synthetic process affects the photocatalytic properties of TiO_2/Fe_2O_3 which was seen from the diminishing of O-Cresol degradation. Zhu et al., [52] reported the synthesis and characterization of Fe-TiO_2 photocatalyst using a hydrothermal method. The photocatalytic properties of Fe doped TiO_2 were studied. In the synthetic methods, $FeCl_3$ and $FeCl_2$ were used to dope into TiO_2 to produce $FeCl_3$-TiO_2 and $FeCl_2$-TiO_2. The surface areas and photocatalytic properties of both materials were compared and found that $FeCl_3$-TiO_2 had higher surface area and photocatalyst doped with $FeCl_3$ have better catalytic property than those doped with $FeCl_2$. The specific surface area found

at 101.4 and 90.5 m^2 g^{-1} for $FeCl_3$-TiO_2 and $FeCl_2$-TiO_2, respectively. Higer specific surface area may be support the higher photocatalytic activity, due to enhance the adsorption of irradiation photons and dye molecules. Moreover, the results from UV-Vis reflectance spectra presented a small shift to longer wavelength and the adsorption were extended to the visible ranges for the Fe doped samples.

1.5 Analytical methods for the detection of arsenic

Several techniques are used to determine arsenic concentrations in solutions such as atomic absorption spectrometry (AAS) coupled to hydride generation (HG-AAS), electrothermal atomic absorption spectrometry (ETAAS), inductively coupled plasma atomic emission spectroscopy (ICP-AES), high-performance liquid chromatography coupled to ICP-MS (HPLC-ICP-MS), X-ray fluorescence (XRF), neutron-activation analysis (NAA) and capillary electrophoresis (CE). These techniques are all laboratory based and have substantial acquisition and subsistence costs associated [87]. Electroanalytical techniques, in contrast, are portable and inexpensive with low detection limit for arsenic [89]. This includes polarography with a dropping mercury electrode or gold electrode and anodic and cathodic stripping methods, anodic stripping voltammetry (ASV), anodic stripping chronopotentiometry (SC) and cathodic stripping voltammetry (CSV). Numerous gold electrodes have been used including disk electrodes, microwires, films on glassy carbon or on platinum, interconnected microdisk arrays, nanoparticles and modified gold electrodes with carbon nanotubes [89].

Voltammetry is a versatile, low cost electro-analytical technique for the quantification of arsenic in water samples [88-91] and the characterisation of oxidation/reduction processes [92]. The current produced by electrochemical reactions is measured as a function of an applied potential. Anodic stripping voltammetery (ASV) is frequently used for the determination of trace elements

in aqueous solutions. It consists of two steps: a deposition step where a reductive potential is applied at the working electrode and a stripping step where the potential is varied towards positive values. During the deposition step, the target ion is reduced and accumulates at the surface of the electrode. During the stripping step, the accumulated metal is oxidised back to solution and the current generated by this oxidation is directly proportional the concentration of the element in the sample [93].

All forms of inorganic arsenic present in the water needs to be transformed into the same chemical form, because arsenite and arsenate are not accumulated at the same rate. Therefore, prior to measurement, arsenite can be oxidised to arsenate or arsenate reduced to arsenite. The latter is difficult and needs a strong reducing agent possibly with heating the solution. However, the oxidation of arsenite to arsenate is rapid and can be achieved by imposing a low potential of -1.5 V to the gold electrode. Protons are reduced (Eq. 1.5) and H_2 gas is formed, as can be seen by the occurrence of bubbles at the surface of gold electrode. This reduction current must be matched by an oxidation current at the auxiliary electrode. In that case, two main reactions occur: the oxidation of water to oxygen (Eq. 1.6) and the oxidation of chloride to hypochlorous acid (Eq. 1.7). This latter is a strong oxidant that oxidises rapidly any arsenite present in the solution to arsenate (Eq. 1.8).

The oxidation process is rapid and completed within 30s. After arsenite in solution was oxidized to arsenate, the determination of total inorganic arsenic is carried out by ASV measurements. The reactions on the surface of a gold electrode are shown as following equations.

$$H^+ + 2e^- \rightleftharpoons H_{2(g)} \quad (1.5)$$

$$2H_2O \rightleftharpoons O_{2(g)} + 4H^+ + 4e^- \quad (1.6)$$

$$Cl^- + H_2O \rightleftharpoons HOCl^- + H^+ + e^- \quad (1.7)$$

$$HOCl^- + As^{III}(OH)_3 \rightleftharpoons As^{V}O(OH)_3 + 2e^- + H^+ + Cl^- \quad (1.8)$$

$$As^{V}O(OH)_3 + 5e^- + 5H^+ \rightleftharpoons As^0 + 4H_2O \quad (1.9)$$

$$As^0 + 3H_2O \rightleftharpoons As^{III}(OH)_3 + 3H^+ + 3e^- \quad (1.10)$$

The determination of arsenate and arsenite in various types water samples using a vibrated gold microwire electrode have been reported by Salaün et al., [88, 89, 91]. This electrode can directly measure arsenic in the water without any sample pretreatment requirements and also working in high concentrations of iron and mercury without any interferences on the analytical peak signal of arsenic [88, 89].

1.6 Aims and Objectives

The aim of this PhD project was to characterize the interaction of arsenic with TiO_2/Fe_2O_3 bicomposites synthesized with three different methods including the photocatalytic oxidation of arsenic(III) to arsenic(V) and to identify the most suitable synthetic method for subsequent development of commercial sorbent.

To achieve this overall aim, the following specific research objectives were tackled:

(i) To assess adsorption capacity and kinetics of arsenite on three different TiO_2/Fe_2O_3 binary mixed oxides

(ii) To establish and compare the binding modes of arsenate and arsenite onto the three different types of TiO_2/Fe_2O_3 binary mixed oxide surfaces

(iii) To study the photocatalytic oxidation mechanism and compare the photocatalytic oxidation rate of As^{III} to As^{V} onto the surface of three different TiO_2/Fe_2O_3 binary mixed oxides

References

(1) Han, M. J.; Hao, J.; Xu, Z.; Meng, X. *Anal. Chim. Acta* **2011**, *692 (1-2)*, 96–102.

(2) Thermo, Application note AN40653 E 01/04C

(3) Muñoz, E.; Palmero, S. *Talanta* **2005**, *65 (3)*, 613–620.

(4) Sarkar, P.; Banerjee, S.; Bhattacharyay, D.; Turner, A. P. F. *Ecotoxicol. Environ. Saf.* **2010**, *73 (6)*, 1495–1501.

(5) Wang, J. P.; Qi, L.; Moore, M. R.; Ng, J. C. *Toxicol. Lett*. **2002**, *133*, 17–31.

(6) International Agency for Research on cancer. *Monographs on the evlution of the carcinogenic risk to humans and their supplements: some metals and metallic compounds*. **1980**, *23*, 1.

(7) The U.S. Environmental Protection Agency. *EPA625-3-87-013*. **1988.**

(8) Bang, S.; Patel, M.; Lippincott, L.; Meng, X. *Chemosphere*. **2005**, *60*, 389-397.

(9) Smedley, P. L.; Kinniburgh, D. G. *Appl. Geochemistry.* **2002**, *17*, 517.

(10) Naujokas, M. F.; Anderson, B.; Ahsan, H.; Aposhian, H. V.; Graziano, J. H.; Suk, W. A. *Environ. Health Perspect.* **2013**, *121*, 295.

(11) Rodríguez-Lado, L.; Sun, G.; Berg, M.; Zhang, Q.; Xue, H.; Zheng, Q.; Johnson, C. A. *Science.* **2013**, *341*, 866.

(12) Kinniburgh, D. G.; Newell, a. J.; Davies, J.; Smedley, P. L.; Milodowski, a. E.; Ingram, J. a.; Merrin, P. D. *Geol. Soc. London, Spec. Publ.* **2006**, *263*, 265.

(13) Drinking Water Inspectorate. *Drinking water 2012 - Private water supplies in England*; 2012; p. 46.

(14) Sánchez, J.; Rivas, B. L. *Desalination*. **2011**, *270 (1-3)*, 57–63.

(15) Hong, S.; Park, S.; Lee, S.; Yang, Y. I.; Song, H. D.; Yi, J. *Anal. Chim. Acta.* **2011**, *694*, 136-141.

(16) Guan, X.; Du, J.; Meng, X.; Sun, Y.; Sun, B.; Hu, Q. *Journal of Hazardous Materials*. **2012**, *215*, 1-16.

(17) Mondal, P.; Bhowmick, S.; Chatterjee, D.; Figoli, A.; Van der Bruggen, B. *Chemosphere.* **2013**, *92*, 157.

(18) Garelick, H.; Dybowska, A.; Valsami-Jones, E.; Priest, N. *J. Soils Sediments.* **2005**, *5*, 182.

(19) Ng, K.; Ujang, Z.; Le-clech, P. *Rev. Environ. Sci. Biotechnol.* **2004**, 43.

(20) Choong, T. S. Y.; Chuah, T. G.; Robiah, Y.; Gregory Koay, F. L.; Azni, I. *Desalination.* **2007**, *217(1-3)*, 139-166.

(21) Mohan, D.; Pittman, C. U. *J. Hazard. Mater.* **2007**, *142*, 1-53.

(22) Jain, C. K.; Singh, R. D. *J. Environ. Manage.* **2012**, *107*, 1.

(23) Mondal, P.; Majumder, C. B.; Mohanty, B. *J. Hazard. Mater.* **2006**, *137*, 464.

(24) Jiang, J. Q. *Water Sci. Technol.* **2001**, *44*, 89.

(25) Kartinen, E. O.; Martin, C. J. *Desalination.* **1995**, *103*, 79.

(26) Sutherland, D.; Swash, P. M.; Macqueen, a C.; McWilliam, L. E.; Ross, D. J.; Wood, S. C. *Environ. Technol.* **2002**, *23*, 1385.

(27) Ngo, H. H.; Vigneswaran, S.; Hu, J. Y; Thirunavukkarasu, O.; Viraraghava, T. *Water. Sci. Technol.: Water Supply 2.* **2002**, *5-6*, 119-125.

(28) Lin, T. F.; Wu, J. K. *Water Res.* **2001**, *35*, 2049-2057.

(29) Hao, J.; Han, M. J.; Meng, X. *J. Hazard. Mater.* **2009**, *167* (1-3), 1215–1221.

(30) Pirilä, M.; Martikainen, M.; Ainassaari, K.; Kuokkanen, T.; Keiski, R. L. *J. Colloid Interface Sci.* **2011**, *353*, 257-262.

(31) Borho, M.; Wilderer, P. *Water Sci. Technol.* **1996**, *34* (9), 25–31.

(32) Lee, H.; Choi, W. *Environ. Sci. Technol.* **2002**, *36*, 3872-3878.

(33) Kim, Y.; Kim, C.; Choi, I.; Rengaraj, S.; Yi, J. *Environ. Sci. Technol*. **2004**, *38* (3), 924–931.

(34) Xu, Z.; Li, Q.; Gao, S.; Shang, J. K. *Water Res.* **2010**, *44*, 5713-5721.

(35) Dutta, P. K.; Ray, A. K.; Sharma, V. K.; Millero, F. J. *J. Colloid Interface Sci.* **2004**, *278*, 270-275.

(36) Mato, J. T.; Yavuz, C.; Yean, S. *Sci. Technol. Adv. Mater.* **2007**, *8*, 71-75.

(37) Ndur, S. A.; Norman, D. J. Abstracts with Programs-Geological Society of America. **2003**, *35(6)*, 5-12.

(38) Choi, W.; Yeo, J.; Ryu, J.; Tachikawa, T.; Majima, T. *Environ. Sci. Technol.* **2010**, *44*, 9099-9104.

(39) Li, Y.; Liu, J. R.; Jia, S. Y.; Guo, J. W.; Zhuo, J.; Na, P. *Chem. Eng. J.* **2012**, *191*, 66-74.

(40) Sun, H.; Zhang, X.; Zhang, Z.; Chen, Y.; Crittenden, J. C. *Environ. Pollut.* **2009**, *157*, 1165-1170.

(41) Gupta, K.; Ghosh, U. C. *J. Hazard. Mater.* **2009**, *161*, 884-892.

(42) Pal, B.; Sharon, M.; Nogami, G. *Mater. Chem. Phys.* **1999**, *59(3),* 254-261.

(43) Barringer, E. A.; Bowen, H. K. *Langmuir*. **1985**, *1(4)*, 414-420.

(44) Kim, K. D.; Kim, H. T. *J. Industrial Eng. Chem.* **2000**, *6(5),* 281-286.

(45) Tsuzuki, a.; Murakami, H.; Kani, K.; Kawakami, S.; Torii, Y. *J. Mater. Sci. Lett.* **1990**, *9(6)*, 624-626.

(46) Funakoshi, K.; Nonami, T. *J. American Ceramic Soc.* **2006**, *89(8)*, 2681-2386.

(47) Raileany, M.; Crisan, M.; Dragan, N.; Crisan, D.; Galtayries, A.; Braileanu, A.; Ianculescu, A.; Teodorescu, V. S.; Nitoi, I.; Anastasescu, M. *J. Sol-Gel Sci. Tech.* **2009**, *51(3),* 315-329.

(48) Liu, K.; Fu, H.; Shi, K.; Xiao, F.; Jing, L.; Xin, B. *J. Phys. Chem. B.* **2005**, *109*, 18719-18722.

(49) Zhou, W.; Fu, H.; Pan, K.; Tian, C.; Qu, Y.; Lu, P.; Sun, C. C. *J. Phys. Chem. C*. **2008**, *112 (49)*, 19584–19589.

(50) D'Arcy, M.; Weiss, D.; Bluck, M.; Vilar, R. *J. Colloid Interface Sci.* **2011**, *364*, 205-212.

(51) Kang, M.; Choung, S.J.; Park, J. Y. **2003**, *87(1-4)*, 87-97.

(52) Zhu, J.; Zheng, W.; He, B.; Zhang, J.; Anpo, M. *J. Mol. Catal. A Chem.* **2004**, *216(1)*, 35-43.

(53) Stumm, W. *Aquatic Chemistry.* 3rd ed, New York: Wiley. **1996**, 1022.

(54) McCash, E. M. *Surface Chemistry*, Oxford: Oxford University Press. **2001**, 177.

(55) Pena, M. E.; Korfiatis, G. P.; Patel, M.; Lippincott, L.; Meng, X. *Water Res.* **2005**, *39(11)*, 2327-2337.

(56) Hristovski, K.; Baumgardner, A.; Westerhoff, P. *J. Hazard. Mater.* **2007**, *147(1-2)*, 256-274.

(57) Sabbatini, P.; Rossi, F.; Thern, G.; Marajofsky, A.; Fidalgo de Cortalezzi, M.M. *Desalination*. **2009**, *248*, 184-192.

(58) Zhang, S.; Niu, H.; Cai Y.; Zhao, X.; Shi, Y. *Chem. Eng. J.* **2010**, *158(3)*, 599-607.

(59) Benavente, M.; Arévalo, M.; Martínez, J. *Water Pract. Technol.* **2006**, 1.

(60) Guo, H.; Stuben, D.; Berner, Z.; Yu, Q. *Appl. Geochem*. **2009**, *24(4)*, 657-663.

(61) Sherman, D. M.; Randall, S. R. *Geochim. Cosmochim. Acta*. **2003**, *67*, 4223-4230.

(62) Fendorf, S.; Eick, M. J.; Grossl, P.; Sparks, D. L. *Environ. Sci. Technol.* **1997**, *31(2)*, 315-320.

(63) Manning, B. A.; Fendorf, S. E.; Goldberg, S. *Environ. Sci. Technol.* **1998**, *32*, 2383-2388.

(64) Manning, B. A.; Hunt, M. L.; Amrhein, C.; Yarmoff, J. A. *Environ. Sci. Technol.* **2002**, *36*, 5455-5461.

(65) Ona-Nguema, G.; Morin, G.; Juillot, F.; Calas, G.; Brown, G. E. *Environ. Sci. Technol.* **2005**, *39*, 9147-9155.

(66) Pena, M.; Meng, X.; Korfiatis, G. P.; Jing, C. *Environ. Sci. Technol.* **2006**, *40*, 1257-1262.

(67) Jegadeesan, G.; Al-Abed, S. R.; Sundaram, V.; Choi, H.; Scheckel, K. G.; Dionysiou, D. D. *Water Research*. **2010**, *44*, 965-973.

(68) Morin, G.; Ona-Nguema, G.; Wang, Y.; Menguy, N.; Juillot, F.; Proux, O.; Guyot, F.; Calas, G.; Brown, G. E. *Environ. Sci. Technol.* **2008**, *42*, 2361-2366.

(69) Guan, X. H.; Wang, J.; Chusuei, C. C. *J. Hazard. Mater.* **2008**, *156*, 178-185.

(70) Jönsson, J.; Sherman, D. M. *Chem. Geol.* **2008**, *255*, 173-181.

(71) Jing, C.; Cui, J.; Huang, Y.; Li, A. Appl. Mater.Interfaces. **2012**, *4*, 714-720.

(72) Hashimoto, K.; Iries, H.; Fujishima, A. *Jpn. J. Appl. Phys.* **2005***, 44(12),* 8269-8285.

(73) Bahnemann, D. *Solar Energy*. **2004**, *77(5)*, 445-459.

(74) Ferguson, M. A.; Hoffmann, M. R.; Hering, J. G. *Environ. Sci. Technol.* **2005**. *39*, 1880-1886.

(75) Ranby, B.; Rabek, J. F. *Photodegradation*. Bristol: Wiley-Interscience. **1975**, 573.

(76) Hanaor, D. A. H.; Sorrell, C. C. *Journal of Materials Science*. **2011**, *46(4)*, 855-874.

(77) Bissen, M.; Vieillard-Baron, M. M.; Schindelin, A. J.; Frimmel, F. H. *Chemosphere*. **2001**, *44*, 751-757.

(78) Yang, H.; Lin, W. Y.; Rajeshwar, K. *J. Photochem. Photobio. Chem.* **1999**. *123(1-3)*, 137-143.

(79) Xu, T. L.; Kamat, P. V.; O'Shea, K. E. *J. Phys. Chem. A*. **2005**, *109*, 9070-9075.

(80) Ryu, J.; Choi, W. *Environ. Sci. Technol.* **2004**, *38*, 2928-2933.

(81) Jayaweera, P. M.; Godakumbura, P. I.; Pathiratne, K. A. S. Curr. Sci. **2003**, *84*, 541-543.

(82) Dutta, P. K.; Pehkonen, S. O.; Sharma, V. K.; Ray, A. K. *Environ. Sci. Technol.* **2005**, *39*, 1827-1834.

(83) Tsimas, E. S.; Tyrovola, K.; Xekoukoulotakis, N. P.; Nikolaidis, N. P.; Diamadopoulos, E.; Mantzavinos, D. *J. Hazard. Mater.* **2009**, *169*, 376-385.

(84) Xu, Z.; Meng, X. *J. Hazard. Mater.* **2009**, *168*, 747-752.

(85) Yoon, S. H.; Lee, J. H. *Environ. Sci. Technol.* **2005**, *39*, 9695-9701.

(86) Yoon, S. H.; Oh, S. E.; Yang, J. E.; Lee, J. H.; Lee, M.; Yu, S.; Pak, D. *Environ. Sci. Technol.* **2009**, *43*, 864-869.

(87) Leermakers, M.; Baeyens, W.; De Gieter, M.; Smedt, B.; Meert, C.; De Bisschop, H. C.; Morabito, R.; Quevauviller, P. Trac-Trends Anal. Chem. ***2006***, *25*, 1.

(88) Salaün, P.; Gibbon-Walsh, K. B.; Alves, G. M. S.; Soares, H. M. V. M.; van den Berg, C. M. G. *Anal. Chim. Acta*. **2012**, *746*, 53-62.

(89) Salaün, P.; Planer-Friedrich, B.; van den Berg, C. M. G. *Anal. Chim. Acta*. **2007**, *585*, 312-322.

(90) Alves, G. M. S.; Magalhães, J. M. C. S.; Salaün, P.; van den Berg, C. M. G.; Soares, H. M. V. M. *Anal. Chim. Acta*. **2011**, *703*, 1-7.

(91) Gibbon-Walsh, K.; Salaün, P.; van den Berg, C. M. G. *Anal. Chim. Acta*. **2012**, *710*, 50-57.

(92) Holler, F. J.; Skoog, D. A.; Crouch, S. R. *Principles of instrumental analysis;* Belmont: Thomson: **2007**; .

(93) Harris, D.;. *Quantitative Chemical Analysis;* Fremann: **2010**;.

Chapter 2

Experimental methods

This chapter presents the experimental methods for synthesis of the TiO_2/Fe_2O_3 binary mixed oxides, and their characterization using Scanning Electron Microscopy (SEM), Brunauer-Emmett-Teller (BET), X-ray diffraction spectroscopy (XRD). Details regarding the analytical techniques for the determination of arsenic using voltammetry and X-ray spectroscopy (XAS) are also provided.

2.1 Synthesis of TiO_2/Fe_2O_3 binary mixed oxides

Several synthetic methods have been published for the preparation of TiO_2/Fe_2O_3 binary mixed oxides including co-precipitation [1], impregnation [2], sol-gel [3], hydrothermal hydrolysis and crystallization [4], and ethanol-assisted hydrothermal method [5].

Our group has previously carried out a comparison of the five synthetic methods for the binary mixed oxides including co-precipitated commercial Ti/Fe, mesoporous Ti/Fe, organic precursor hydrolysis Ti/Fe, sol-gel Ti/nanoparticle Fe and sol-gel Ti/Fe. In that study, the costs of the synthetic method were compared and the effect of Ti/Fe ratio variation on $\%As^V$ removal were investigated. The results showed that co-precipitated, mesoporous and sol-gel are cost effective methods for producing TiO_2/Fe_2O_3 binary mixed oxides. Additionally, the $\% As^V$ removal was not much different when using Ti/Fe ratio 1:1 and 1:2 by mass. Therefore, these three synthetic methods were used for further study.

In this work, TiO_2/Fe_2O_3 binary mixed oxides were synthesized using a co-precipitation method, a mesoporous method or a sol-gel method, followed by calcination process. The three different types of bicomposite materials are subsequently called co-precipitated (CP), mesoporous (MB) and sol-gel (SG) TiO_2/Fe_2O_3 binary mixed oxides.

2.1.1 Synthesis of co-precipitated TiO_2/Fe_2O_3 binary mixed oxides (CP)

A commercial (1.5g, 0.019 mol) was added to an iron nitrate solution (30 mL, 0.6 M) to yield a mixture containing a 1:1 molar ratio of Ti and Fe. The beaker was sealed with parafilm and the reaction mixture stirred for 30 min. After this time, the ethanol in the solution was evaporated overnight on a hot plate at 50 ^oC. The residual product was then calcined in a furnace at 300 ^oC for 10 min. The solid residue was cooled and grounded with a clean mortar and pestle to get a homogenized powder and then again calcined at 300 ^oC for 6 h. The resulting material was kept in a desiccator until further experiments.

2.1.2 Synthesis of mesoporous TiO_2/Fe_2O_3 binary mixed oxides (MB)

The synthesis of MB was carried out in two steps by small modifications of a previously reported procedure [1, 2, 5].

Step1: First, mesoporous TiO_2 anatase was synthesised by a single-step method from a $Ti(OBu^n)_4$-Pluronic P123-EtOH-HCl system. The reacting solution were prepared in two separate beakers. The first beaker contained ethanol (12 g, 0.261 mol) and Pluronic P123 (1 g, 1.74×10^{-4} mol). The second beaker contained $Ti(OBu^n)_4$ (2.7 g, 8 mmol) and concentrated HCl (3.2 g, 30 mmol). The EtOH/ Pluronic P123 mixture was slowly added into the solution containing $Ti(OBu^n)_4$ and concentrated HCl. The resulting mixture was then aged at room temperature

and continuously stirred until the solution changed to a gel-like white film. The residual product was calcined at 350 ºC for 4 h (ramp of 1 ºC min^{-1}) and cooled to room temperature and then crushed to yield mesoporous TiO_2 anatase [6].

Step 2: The mesoporous TiO_2/Fe_2O_3 bicomposites were prepared by adding mesoporous TiO_2 (1.5 g) to an iron nitrate solution (30 mL, 0.6 M). The resulting mixture contained a 1:1 molar ratio of Ti and Fe. This mixture was stirred for 30 min and heated at 50 ºC overnight to evaporate ethanol. The resulting product was calcined in a furnace at 300 ºC for 10 min, then cooled and grounded to homogenize the compound in a clean mortar. After this, the product was again calcined at 300 ºC for 6 h. The material was stored in a desiccator until further experiments.

2.1.3 Synthesis of sol-gel TiO_2/Fe_2O_3 binary mixed oxides (SG)

Tetraethylorthotitanate (TEOT) (5 g or 1.47 M, 0.022 mol) was placed in a beaker and a solution of Fe $(NO_3)_3.9H_2O$ (8.86 g or 1.47 M, 1.47 M, 0.022 mol) in ethanol (12 g or 15 mL, 0.261 mol) was added. The resulting solution was stirred for 60 min at 50 ºC to evaporate the ethanol. Then, 10 drops of concentrated HNO_3 were added drop wise while stirring to initiate gelation. Stirring was continued until gelling was completed. The residual solid was calcined at 300 ºC for 3.5 h and then cooled to room temperature. The product was ground to a fine powder in a clean mortar and pestle. The material was stored in a desiccator until further experiments.

2.1.4 Characterization of TiO_2/Fe_2O_3 binary mixed oxides

X-ray diffraction patterns of all bicomposites were recorded using an Enraf Nonius PDS 120 X-ray diffractometer using either a Cu tube 40 kV and 35 mA or Co tube 35 kV and 30 mA source. These patterns were used to confirm the Ti

and Fe phases in the mixed oxides comparing with standard anatase, hematite and rutile. The morphology and size distribution of all mixed oxides were examined by LEO 1455 VP scanning electron microscope. The surface areas of these mixed oxides were obtained by a Micromeritics Tristar surface area and Porosity Analyser and Micromeritics FlowPrep 060 Sample Degases System with Brunauer-Emmett-Teller (BET) method by N_2 adsorption.

2.2 Voltammetry

The concentrations of arsenic in sample solutions were measured using square wave anodic stripping voltammetry (SWASV) on a Metrohm VA stand. An in house made 25 μm vibrated gold microwire electrode as working electrode, iridium wire as auxiliary electrode and a Metrohm Ag/AgCl electrode as reference electrode were used for the measurements [7, 8]. The 25 μm diameter of the gold microwire electrode was conditioned by cyclic voltammetry scan three times in 0.5 M H_2SO_4 by using a deposition potential of -3 V for 30 s before arsenic measurement. Using SWASV, the condition potential used for total arsenic measurement was 0.7 V for 3 s, the deposition potential was -1 V for 10 s. The anodic stripping voltammetric (ASV) scan was initiated at -0.2 V and finished at 0.1 V. The background current was measured either by scanning a cell containing only the background 0.1 M HCl, the background electrolyte, or by scanning the sample using a deposition time of 1 s. For As^{III} measurement, the condition potential was 0.7 V for 3 s, the deposition potential was -1.2 V for 10 s. The ASV scan started at -0.2 V and ended at 0.1 V. The background current was analyzed by scanning the sample in 50 mM borate buffer pH 9 using a deposition time of only 1 s. Two additions of analytical standard were spiked to the sample and the concentration was determined using the standard addition method. The voltammetric parameters for As^{III} and As^{V} determination by square wave anodic stripping voltammetry (SWASV) are shown in Table 2.1.

Table 2.1 *Voltammetric parameters for As^{III} and As^{V} analysis by SWASV using a vibrating gold microwire electrodes with background subtraction (BGS).*

Parameters	As^{III}	As^{V}
Pretreatment		
Purge time (s)	0	0
Conditioning potential (V)	0.7	0.7
Duration time (s)	5	5
Stirrer off during conditioning	-	-
Deposition potential (V)	-1.2	-1.0
Duration (s)	10	10
Stirrer off during deposition	-	-
Equilibration time (s)	1	1
Measurement		
Cell of after measurement	-	-
Frequency (8-2000 Hz)	50	50
Potentials		
Initial potential (V)	-0.2	-0.6
End potential (V)	0.6	0.4
Step potential (V)	0.00795	0.00795
Amplitude (V)	0.04995	0.04995
Standby potential (V)	0.55	0.55
Pretreatment		
Step equilibrium at threshold	-	-
Equilibrium threshold value (A)	0.05	0.05
Miscellaneous		
Number of scans	1	1

2.3 X-ray absorption spectroscopy (XAS)

X-ray absorption spectroscopy (XAS) was used to study the photocatalytic oxidation of As^{III} to As^{V} on the surfaces of the three different types of TiO_2/Fe_2O_3 binary mixed oxides synthesized in this project and to study the geometry of the surface complexes. X-ray absorption near edge structure (XANES) spectra was used to identify the oxidation state of arsenic. The structural parameters (e.g. interatomic distances) of arsenic adsorbed onto the binary mixed oxides were determined by extended X-ray absorption fine structure (EXAFS). These experiments were performed at the Diamond Light Source, UK.

The storage ring was operated at 3.0 GeV (electron energy). A Si 111 monochromator was used for the selection of the energy at arsenic K-edge. Ge detector in fluorescence mode was used to monitor analytical X-ray beam signal of samples. The XANES spectra of arsenic K-edge were obtained and calibrated

with standard As^{III} oxide (As_2O_3) and sodium arsenate dibasic heptahydrate ($Na_2HAsO_4.7H_2O$).

2.3.1 Solid samples

Standards or samples for XAS analysis were ground to a powder and then mixed with cellulose in a ratio of 1: 100 by mass. The mixing powders were then pressed into pellets and mounted onto the sample holder with kapton tape to hold them in position prior to measurements.

Arsenic was adsorbed on to the solid from the solution for 24 h: solid and solution were then separated and the solids were subsequently kept in sealed opaque tubes until the measurements at the beamline. At the beamline, the solids were pressed into pellet and covered using kapton tape prior to analysis using XAS. The sample set up at the beam line is presented in Figure 2.1.

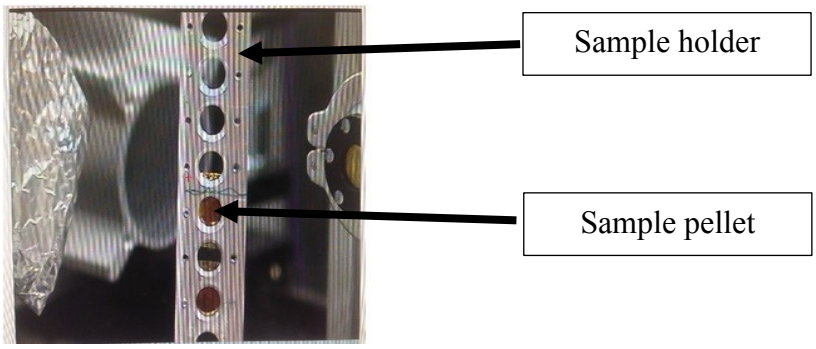


Figure 2.1 *The pellets of standard arsenic and arsenic bound TiO_2/Fe_2O_3 binary mixed oxides were sealed with kapton tape and set at the sample holder.*

2.3.2 Solution samples

In situ solution studies to determine the As^{III} adsorption and photocatalytic oxidation mechanism were conducted in a perspective photo reactor. As^{III} solutions (100 mg L^{-1}) were prepared in different buffers (acetate buffer pH 5, HEPES buffer pH 7 and borate buffer pH 9). In the first step, As^{III} (100 mg L^{-1})

samples were analyzed to determine the initial beam intensity. After this, the binary mixed oxide materials were added to the solution and XANES spectra in fluorescence mode were collected at different time intervals. A picture of the experimental set-up is shown in Figure 2.2.

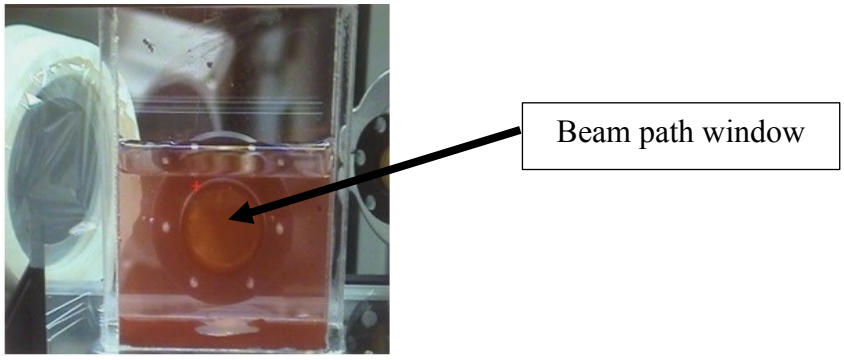


Figure 2.2 *Picture of the experimental set-up to carry out studies of As^{III} adsorption and photocatalytic oxidation by TiO_2/Fe_2O_3 binary mixed oxides in a perspective photo reactor. The synchrotron beam passed through the solution at the beam path window (diameter 4.0 cm).*

2.3.3 Data analysis

As^{III} and As^{V} K-edge XANES spectra were recorded using a Si 111 monochromator and Ge fluorescence detector. Instrumental conditions were optimized to minimize synchrotron X-ray beam induced oxidation of As^{III}. The reference materials used for As^{III} and As^{V} edge positions were As^{III} oxide (As_2O_3, Sigma-Aldrich) and sodium arsenate dibasic heptahydrate ($Na_2HAsO_4.7H_2O$, Sigma-Aldrich).

The oxidation states of the arsenic in this work were identified using arsenic K-edge XANES spectra of As^{III} and As^{V} standards. Initial XANES analyses of As^{III} bound to the TiO_2/Fe_2O_3 binary mixed oxides samples were done by scanning synchrotron X-ray beam on the samples and after that, individual XANES scans were obtained within approximately 30 s and collected continuously for 45 min. For the experiments where UV (18W) light was used to radiate the cells (Chapter

5), the XANES spectra were collected only for the first scan to avoid photocatalytic oxidation by the synchrotron beam.

The As^{III}/As^{V} ratio on the surface of the bicomposites was calculated by using XANES spectra combination fitting procedure in the Athena XAS data processing program. The XANES spectra of As^{III} or As^{V} adsorption on the surface of the binary mixed oxides were used as the references. The intensity of As^{III} XANES spectra on the binary mixed oxides at the first scan were used to refer 100% of As^{III} on the binary mixed oxides. Additionally, the last scan after synchrotron beam irradiation found that the sample had completely oxidized to As^{V}. The intensity of As^{V} at the last scan was used to refer 100% of As^{V} on the binary mixed oxides. The two intensity values were fitted in the Athena data processing program to calculate the ratio of As^{III}/As^{V} at different time intervals during photocatalytic oxidation reaction on the binary mixed oxides s' surface.

The EXAFS spectra of arsenic adsorbed on TiO_2/Fe_2O_3 binary mixed oxides were collected only for the first scan to avoid the effect of beam induced As^{III} oxidation on the surface of TiO_2/Fe_2O_3 binary mixed oxides. The EXAFS spectra in R-space were used to determine atomic distances and to identify the geometry of arsenic onto the surface of the binary mixed oxides. The K-edge XANES spectra of standard arsenic compounds (As_2O_3 and $Na_2HAsO_4.7H_2O$) were used as references to confirm oxidation state of arsenic on the binary mixed oxides.

2.4 Adsorption using batch and column experiments

2.4.1 Batch experiment

Batch adsorption experiments were carried out to investigate arsenic adsorption on all three types of TiO_2/Fe_2O_3 binary mixed oxides in 0.01 M HEPES buffer pH 7 at 25 ^{o}C (298 K). As^{V} concentrations of 100 mg L^{-1} with fixed adsorbent concentration (1 g binary mixed oxides L^{-1}) and in a solution of 0.01 M KNO_3

ionic strength were shaken for 24 h until equilibrium was reached. Arsenic concentrations in this part of study were determined by voltammetry.

As^{III} adsorption capacities on MB in 0.01 M acetate buffer (pH 5), 0.01 M HEPES buffer (pH 7) and 0.01 M borate buffer (pH 9) were determined using adsorption isotherms. The As^{III} concentrations ranged between 20 and 100 mg L^{-1}, the amount of MB was 1 g L^{-1} and the ionic strength of 0.01 M KNO_3. These batch experiments were carried out by shaking the mixtures for 24 h. Additionally, As^{III} adsorption in strongly alkaline solution (pH 12), in the presence of competitive phosphate anions and with different amounts of adsorbent were examined.

Adsorption kinetics were determined using initial As^{III} concentration of 40 mg L^{-1} with 1 g L^{-1} of MB and 0.01 M KNO_3 in 0.01 M HEPES (pH 7) at 25 ^oC. The As^{III} solutions in the reaction bottles were sampled at time intervals between 0 to 24 h.

2.4.2 Column experiment

The potential application of the sorbent in a continuous flow scavenging system, was tested using a fixed bed column. To that end, a glass column with 1.3 cm inner diameter and 30 cm height was used to contain the sorbent. Glass beads were used on top of the sorbent to act as a solution distributor. Arsenic sample concentration of 100 μg L^{-1} with 50 mL of volumes were used to optimize column conditions such as pH, amount of sorbent, flow rate and column recycle and the percentages of arsenic removal.

2.5 Photocatalytic oxidation

The photocatalytic oxidation process of As^{III} on the three types of binary mixed oxides surfaces and in the binary mixed oxides suspension were examined in a set of experiments described below. In situ experiments determined changes in

oxidation of arsenic on surface after irradiation with synchrotron or UV lamp using XANES. Ex situ experiment determined changes the oxidation of arsenic in the binary mixed oxides suspension after UV irradiation using voltammetry.

2.5.1 In situ photocatalytic oxidation

2.5.1.1 Photocatalytic oxidation of As^{III} on mineral surface using synchrotron beam

This set of experiments focused on determination of the photocatalytic oxidation rates of As^{III} bound to the three different binary mixed oxides using the energy of the synchrotron beam during the exposure onto the solid samples (hence in situ). Changing As^{III}/As^{V} ratios were determined using linear combination fitting of the resulting XANES spectra. The adsorption of As^{III} on TiO_2/Fe_2O_3 binary mixed oxides was conducted under N_2 atmosphere. The oxidation states of arsenic were monitored at the arsenic K-edge.

2.5.1.2 Photocatalytic oxidation of As^{III} on mineral surface using UV 18 watt light

This set of experiments focused on determination of the oxidation states of arsenic and the ratio of As^{III}/As^{V} bound to the three different TiO_2/Fe_2O_3 binary mixed oxides after exposure to UV light (18W) onto the solid samples. As^{III} was adsorbed onto the binary mixed oxides under N_2 atmosphere. The mineral surfaces were subsequently irradiated with UV light. The binary mixed oxides samples collected at different time intervals were subsequently analysed to observe the photocatalytic oxidation kinetics of As^{III} to As^{V} using UV light on the solid and taken to the beam line to analysis using XANES.

The photocatalytic oxidation rates of As^{III} in solution (100 mg L^{-1}) were assessed in two sets of experiments. The first set of experiments used a TiO_2/Fe_2O_3 binary mixed oxides packed tea-bag to carry on the photocatalytic oxidation of As^{III} in the solution. The second set of experiment suspended the solids in solution. XANES spectra were taken subsequently to determine how much As^{III} can be oxidized. The beam only passed through the solution, which was constantly stirred, and not the binary mixed oxides. Before the beam was switched on, As^{III} was left for 30 minutes standing in contact with the tea-bag (see Figure 2.3(B)) so that equilibrium between As^{III} in solution and adsorbed arsenic was reached. Then UV lamp was switched on and the change in arsenic fluorescence from the solution was monitored. This change corresponds to the rate of oxidation to As^{III} to As^{V} by binary mixed oxides (Experimental conditions: As^{III} solution concentration 100 mg L^{-1}, a tea-bag containing 2 g of binary mixed oxides bicomposites, solution pH at 5 and 9).

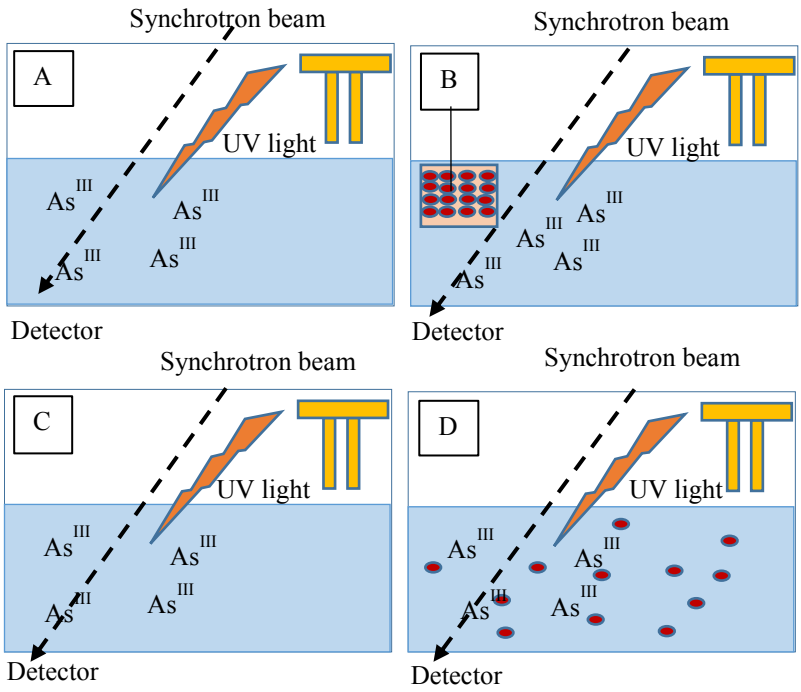


Figure 2.3 *Photocatalytic oxidation of As^{III} to As^{V} with UV light and synchrotron beam, (A) the intensity of As^{III} XANES spectra was analysis before adding tea-bag of binary mixed oxides and (B) tea-bag of binary mixed oxides added, (C) the intensity of As^{III} XANES spectra was analysis before adding binary mixed oxides in the solution and (D) suspension of binary mixed oxides*

The effect of a hydroxyl radical scavenger on the photo-oxidation of As^{III} in contact with a tea-bag containing binary mixed oxides was investigated. For this, the hydroxyl radical scavenger (salicylic acid) was added, and the photo-oxidation process monitored by XANES (Experimental conditions: As^{III} solution concentration 100 mg L^{-1}, 2 g teabag of binary mixed oxides, solution pH 9 and effect of 1:1 mass ratio of MB and salicylic acid hydroxyl scavenger) [2].

2.5.2 Ex situ photocatalytic oxidation

2.5.2.1 UV 18 watt and then As analysis using voltammetry

As the photocatalytic oxidation rates of As^{III} on all type of binary mixed oxides were similar (Chapter 5), detailed experiments were subsequently carried out with only one of them as a representative example (MB). In particular, the photocatalytic oxidation mechanism and kinetics of As^{III} to As^{V} using MB suspension was investigated. The study was divided into two stages: adsorption and photocatalytic reaction. For the first stage, an As^{III} solution (40 mg L^{-1}) was mixed with 1 g L^{-1} MB and stirred for 3 h. In the second step, the samples was irradiated with UV(18W) light and the concentrations of As^{III} and total arsenic were monitored using a gold microwire electrode at different time intervals. Both As^{III} and total As concentrations were used to calculate the total amount of As^{V} in solution. Additionally, the effect of hydroxyl radical scavenger, (i.e. salicylic acid) was also examined in this experimental set-up using 1:1 by mass MB and salicylic acid (1 g L^{-1}) in competition [2].

References

(1) D'Arcy, M.; Weiss, D.; Bluck, M.; Vilar, R. *J. Colloid Interface Sci.* **2011**, *364*, 205-212.

(2) Zhou, W.; Fu, H.; Tian, C.; Qu, Y.; Lu, P.; Sun, C. C. *J. Phys. Chem. C*. **2008,** *112*, 19584-19589.

(3) Trapalis, C. C.; Keivanidis, P.; Kordas, G.; Zaharescu, M.; Crisan, M.; Szatvanyi, A.; Gartner, M.

In *Thin Solid Films*; **2003**, *433*, 186-190.

(4) Zhu, J.; Zheng, W.; He, B.; Zhang, J.; Anpo, M. *J. Mol. Catal. A Chem.* **2004**, *216*, 35-43.

(5) Liu, H.; Shon, H. K.; Sun, X.; Vigneswaran, S.; Nan, H. *Applied Surface Science*. **2011**, *257*, 5813-5819.

(6) Liu, K.; Fu, H.; Shi, K.; Xiao, F.; Jing, L.; Xin, B. *J. Phys. Chem. B.* **2005**, *109*, 18719-18722.

(7) Gibbon-Walsh, K.; Salaün, P.; van den Berg, C. M. G. *Anal. Chim. Acta.* **2012**, *710*, 50-57.

(8) Salaün, P.; Planer-Friedrich, B.; van den Berg, C. M. G. *Anal. Chim. Acta.* **2007**, *585*, 312-322.

Chapter 3

Adsorption capacity, kinetics and mechanism of arsenite on mesoporous TiO_2/Fe_2O_3 binary mixed oxides

TiO_2/Fe_2O_3 binary mixed oxides have been suggested as potential novel sorbents for the removal of arsenic from polluted groundwater as they enable the photocatalytic oxidation of arsenite in waters using UV radiation (Chapter 5). Several synthetic methods have recently been published, however, a critical evaluation and comparision with respect to adsorption capacity, kinetics and mechanism have not been reported.

To this end, we prepared TiO_2/Fe_2O_3 binary mixed oxides using three widely used synthetic methods differing with respect to cost and synthesis time, namely co-precipitation (CP) [1], mesoporous (MB) [5] and sol-gel (SG) [5]. These binary mixed oxides were characterized by X-ray diffraction (XRD), scanning electron microscopy (SEM) and Brunauer-Emmett-Teller (BET) method. XRD patterns showed crystalline peaks of TiO_2 (anatase) and Fe_2O_3 (hematite). SEM revealed porous surfaces consistent with the formation of binary mixed oxides. The characterization results show these synthetic methods can produce binary mixed oxides with suitable features for arsenic removal. The adsorption capacities were constrained using the widely used Langmuir and Freundlich models and kinetic were assessed using the commonly used the pseudo-first, the pseudo second order and the intra-particle diffusion models. The MB showed the

highest removal capacities for arsenate (27.47 mg g^{-1}) compared to CP (13.89 mg g^{-1}) [1] and SG (7.45 mg g^{-1}) [5]. We consequently constrained the kinetics of the adsorption on MB using batch experiments. The pseudo- second order kinetic model showed the best fit (R^2= 0.999).

Continuous flow experiments were consequently conducted using a glass column and we showed that more than 93% of arsenic could be removed from a contaminated water sample with 100 µg L^{-1} of arsenic. The column was re-used five times with relatively small decrease its capacity to remove arsenic (100 µg L^{-1}).

3.1 Introduction

As discussed in chapter 1, many removal studies of arsenic from solution have been reported by adsorbing arsenic on various types of single metal oxides. Considerable research over the past few years has focused, in using metal oxide bicomposites to enhance the physical and chemical properties of the resulting materials for effective arsenic adsorption [1-40]. TiO_2/Fe_2O_3 bicomposite materials have been previously synthesized by using sol-gel [5], co-precipitation [1] and calcination methods [1, 5] and these materials have already been shown to be effective in removing toxic arsenic from contaminated water [1-5].

As^V (as its oxide-arsenate) can be adsorbed with the strong bond interaction on metal oxide active sites. The interaction depends upon the surface charges of metal oxide and As^V species charges-which in turn depends on the protonation level. On the other hand, As^{III} (as its oxide-arsenite) has zero charge at pH below 9, which makes it to display a weaker interaction with the surface of metal oxides. This intern, makes it significantly more difficult to remove As^{III} than As^V. Consequently, most treatment methods for As^{III} need to include a step for its pre-oxidation to As^V before adsorbing onto the metal oxide materials.

TiO_2/Fe_2O_3 bicomposite materials can overcome the complicated steps of As^{III} pre-treatment process since both the oxidation and adsorption process could be carried out on the surface of the bicomposites. Compared with a single metal oxide, bicomposites based on TiO_2 and Fe_2O_3 are more attractive since the photocatalytic oxidation properties of TiO_2 [33-40] can be combined with the good adsorption capabilities of Fe_2O_3 [28-32] – as well as those of TiO_2 itself [16-27] – for efficient scavenging of arsenic in water [1, 2].

TiO_2 materials have been applied for photodegradation of organic pollutants and used to remove arsenic from contaminated water [16-21]. Previous work with TiO_2 has also shown it can photocatalyse the oxidation of As^{III} to As^{V} using UV light activation in aqueous solution [33-36]. Therefore, we decided to explore the use of TiO_2 as a photocatalyst in TiO_2/Fe_2O_3 binary mixed oxides. We expected to use TiO_2/Fe_2O_3 binary mixed oxides to study the photocatalytic oxidation of As^{III} in the further study (Chapter 5). Before that the knowledge about adsorption mechanism and kinetics of arsenic on the bicomposites should be addressed. D'Arcy et al., [1] reported adsorption mechanism and kinetics of As^{V} on the bicomposites [1] and Zhou et al., [2] show the possibility of using the bicomposites for effective remove As^{III} through photocatalytic oxidation and adsorption. However, no report of As^{III} adsorption mechanism and kinetics was found. Therefore, in this chapter, we will report As^{III} adsorption mechanism and kinetics on the binary mixed oxides.

TiO_2 has been identified as an effective photocatalyst but it only works efficiently when irradiated with UV light (<380 nm). This is due to its wide band gap energy around 3.2 eV for anatase and 3.0 eV for rutile. The combination of Fe_2O_3 hematite which has narrower band gap energy around 2.2 eV, with TiO_2 anatase can yield a Ti/Fe-oxide bicomposites with a smaller band gap energy of around 2.6 – 2.9 eV [41-47]. The reduction of the band gap energy in bicomposite materials can therefore improve the photocatalytic property of TiO_2 and could potentially be used under visible or sunlight irradiation [41- 47].

As indicated above, several synthetic methods have been previously reported for the preparation of mixed Ti and Fe oxide materials which have different names depending on synthetic methods or products [1-15] (see Table 3.1).

Table 3.1 *Summary of mixed Ti and Fe oxide material synthetic methods*

Material name	Synthetic method (conditions)	Application	Method highlight	Ref.
a bifunctional TiO_2-Fe_2O_3 bi-composite	- co-precipitation and calcination (TiO_2/ $Fe(NO_3)_3.9H_2O$/EtOH/ Stir 30 min/sonicate 30 min/ calcine at 300^oC 6 h) -BET surface area 41.7 m^2/g	As^V adsorption	-simple synthetic procedure	[1]
mesoporous TiO_2/Fe_2O_3 bifunctional composites	-impregnation and calcination (meso-TiO_2/ $Fe(NO_3)_3.9H_2O$/EtOH/Stir 30 min/sonicate 30 min /calcine at 300^oC 6 h) -BET surface area 95.0 m^2/g	As^{III} and As^V adsorption	-simple synthetic procedure -high surface area	[2]
$TiO_2(Fe^{III})$ nanostructured thin films	-sol-gel method on glass substrate ($TiO(OC_2H_5)_4$/ $Fe(NO_3)_3.9H_2O$/ethyl glycol/HNO_3/densification at 300 and 400 ^oC 1 h and annealed from 450 to 500 ^oC 3 h)	Antibacterial properties	-	[3]
Iron-ion-doped TiO_2 (anatase)	-Hydrothermal hydrolysis and crystallisation ($Ti[OC(CH_3)_3]_4$/$FeCl_2$ or $FeCl_3$/n-octanol/autoclave/dried at 80 ^oC 8h/calcine 564 ^oC 1 h) -BET surface area 90.5-101.4 m^2/g	Photocatlytic reactivity	- high surface area - need to use autoclave	[4]
Slag-iron oxide-TiO_2 adsorbent	-aging and high temperature process (Iron oxide slag/NaOH/aging 2 day/stir 2 h/aged for 12 h/TiO_2/heat at 105^oC 2 h and 550^oC 1 h/vacuum dried at 105 ^oC 24 h)	Photocatalytic oxidation and removal of As^{III}	-	[6]
nanostructured Fe^{III}-Ti^{IV} binary mixed oxide	-sol-gel and low temperature process ($TiCl_4$/$FeCl_3$/HCl/NaOH/dried at 60-70 ^oC) -BET surface area 77.8 m^2/g)	As^{III} and As^V adsorption	- high surface area	[7]
Fe_2O_3-TiO_2 composites	-ethanol-assisted hydrothermal method ($Ti(SO_4)_2$/$Fe(SO_4)$/HNO_3/EtOH/NaOH/dried at 70 ^oC 4 h), BET surface area 43.03 m^2/g	Photocatalytic activity	- simple synthetic procedure	[10]

Table 3.1 (Continued) *Summary of mixed Ti and Fe oxide material synthetic methods*

Material name	Synthetic method (conditions)	Application	Method highlight	Ref.
γ-Fe_2O_3-TiO_2 magnetic nanoparticles	-oxidation and co-precipitation ($FeCl_3.6H_2O$/ $FeCl_2.4H_2O$/NH_4OH/stir 30min/dried 40°C 24 h/calcine in N_2 atmosphere at 400 °C 1 h) -BET surface area 153.9 m^2/g	As^{III} photocatalytic oxidation and adsorption	-high surface area -need N_2 atmosphere	[12]
Fe/Ti bimetal oxide sorbent	-co-precipitaion ($Ti_2(SO_4)_3$/$Fe_2(SO_4)_3$/NH_3/agitated 1 h/aged at 25°C 4 h/dried at 60°C) -BET surface area 32.9 m^2/g	Phosphate removal	-simple synthetic procedure	[15]

Bullough et al., [5] conducted an in-depth cost benefit analysis with respect to published adsorption capacities of TiO_2/Fe_2O_3 and the suggested co-precipitation (CP), mesoporous (MB) and sol-gel (SG) materials (see Table 3.1). Different Ti and Fe ratios in the bicomposites were tested and found that Ti:Fe at 1:1 by mass yielded highest adsorption suitable for arsenic removal. Adsorption isotherm studies of As^V on the bicomposites were subsequently determined and they fitted well with the Langmuir adsorption model.

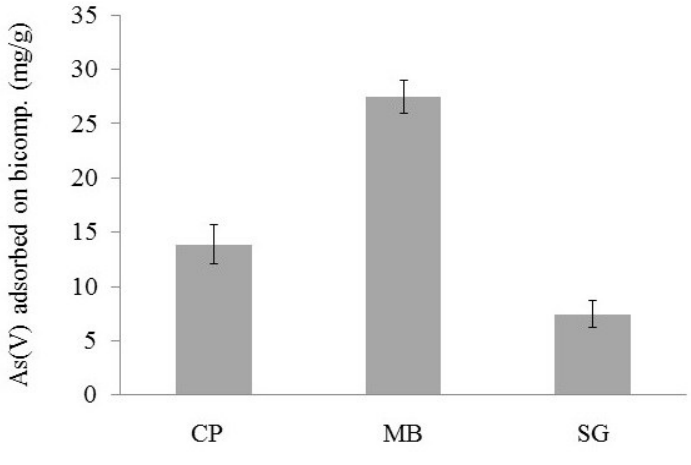


Figure 3.1 *The adsorption of As^V from solution at pH 7 by using CP, MB and SG, amounts of As^V adsorbed were compared to highlight the best bicomposite for arsenic removal, Figure taken from Bullough et al., [5]*

Figure 3.1 presents the results from the adsorption of As^V on the bicomposite materials [5], the amount of As^V adsorbed on CP, MB and SG (1:1) were found at 13.89, 27.47 and 7.45 mg g^{-1}, respectively. Following this study, D'Arcy et al., [1] studied the effect of the pH on adsorption capacities of As^V on CP (1:1) and found higher adsorption at pH 5 (12.14±0.42 mg g^{-1}) than at pH 9 (6.48±0.30 mg g^{-1}). The adsorption capacity of As^V for CP at pH was similar on to that found by Bullough et al., [5]

3.2 Aims and objectives

A better understanding of the adsorption capacities, kinetics and mechanism can be provide a rationale for the design of better materials for arsenic remediation. The adsorption mechanism and kinetics of arsenate on TiO_2/Fe_2O_3 bicomposites were described by D'Arcy et al., [1]. On the other hand, there is no analogous study for arsenite-which, as described in Chapter 1 has higher toxicity than arsenate and is more difficult to separate from contaminated waters. Therefore, the overall aim of the work presented in this chapter was to investigate the synthetic method to produce mesoporous TiO_2/Fe_2O_3 binary mixed oxides and to identify the adsorption capacity, kinetics and mechanism of As^{III} onto mesoporous TiO_2/Fe_2O_3 binary mixed oxides.

The specific objectives required to reach this aims were as follows:

i) To synthesize and characterize mesoporous TiO_2/Fe_2O_3 binary mixed oxides

ii) To determine the capacities and describe mechanism of As^{III} adsorption on mesoporous TiO_2/Fe_2O_3 binary mixed oxides

iii) To examine the kinetics and determine rate constant of As^{III} adsorption on mesoporous TiO_2/Fe_2O_3 binary mixed oxides

3.3 Results and discussion

3.3.1 Mesoporous TiO_2/Fe_2O_3 binary mixed oxides (MB) synthetic method

Since the mesoporous TiO_2/Fe_2O_3 binary mixed oxides (MB) was previously identified as the best adsorbent for arsenic removal [2], a large-scale synthesis was developed and more detailed characterisation of these material was carried out. The XRD can confirm the crystalline peaks of TiO_2 anatase and Fe_2O_3 hematite comparing with standards. First, mesoporous TiO_2 anatase (named MT) was prepared and then used for the synthesis of MB. The characterisation results are presented in Figure 3.2 and 3.3.

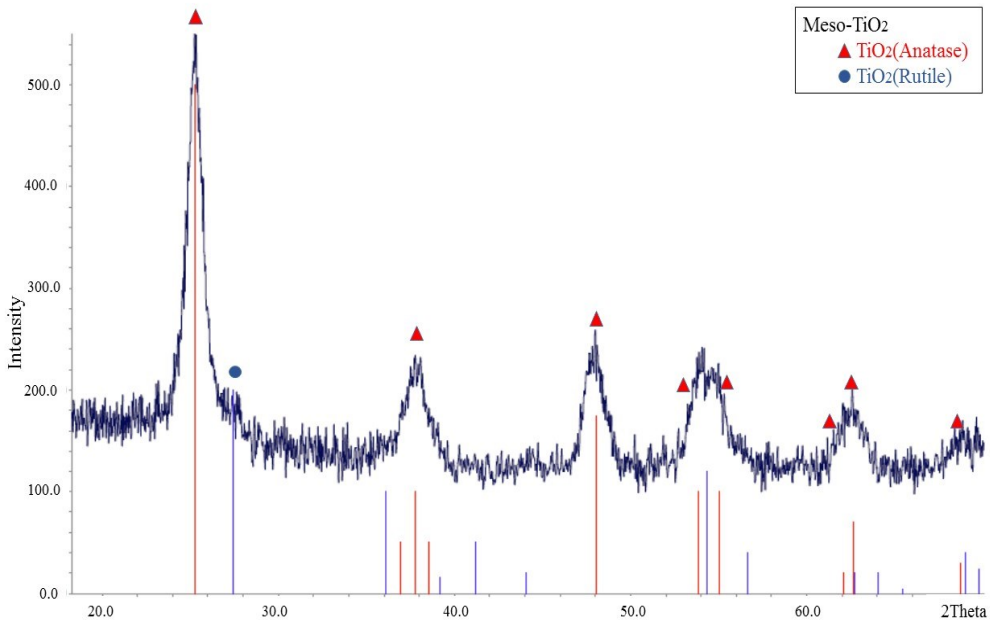


Figure 3.2 *XRD patterns of mesoporous TiO_2 anatase synthesised by using a $Ti(OBu^n)_4$-P123-EtOH-HCl system, calcination at 350°C for 4 h. This material is called MT.*

The XRD pattern shown in Figure 3.2 represents mesoporous TiO_2 synthesised by using a one-step synthesis procedure in a $Ti(OBu^n)_4$-P123-EtOH-HCl system.

The XRD pattern in Figure 3.2 shows crystal peaks of TiO_2 anatase which can confirm this synthetic method can be used to produce mesoporous TiO_2 anatase.

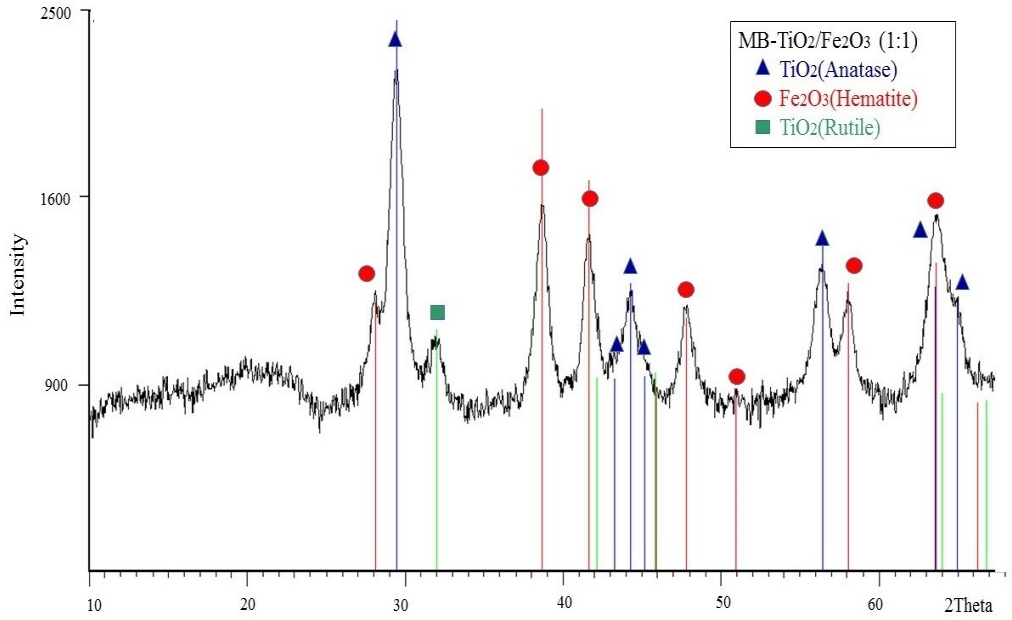


Figure 3.3 *XRD patterns of MB- TiO_2/Fe_2O_3 binary mixed oxides (1:1 molar ratio) synthesised by using co-precipitation of mesoporous TiO_2 (anatase) and Fe_2O_3 (hematite), calcination at 300 ^oC for 6 h.*

The XRD pattern in Figure 3.3 shows sharp peaks for both TiO_2 (anatase) and Fe_2O_3 (hematite) so they could be compared to references and assess the synthetic method. The formation of the MB TiO_2/Fe_2O_3 binary mixed oxides prepared by mesoporous and calcination process was confirmed by XRD as shown in Figure 3.3. The diffraction pattern of the MB sample was compared to those of standard TiO_2 anatase, TiO_2 rutile and Fe_2O_3 hematite. This comparison of the XRD patterns allowed us to conclude that the MB sample is a TiO_2/Fe_2O_3 binary mixture (rather than a bicomposite) with segregated phases corresponding to TiO_2 anatase (with peaks at $2\theta = 29.5^o$, 43.2^o, 44.2^o, 45.2^o, 56.5^o, 63.5^o and 65.0^o) and Fe_2O_3 (with peaks at $2\theta = 28.2^o$, 38.8^o, 41.8^o, 47.8^o, 51.0^o, 58.2^o and 63.8^o).

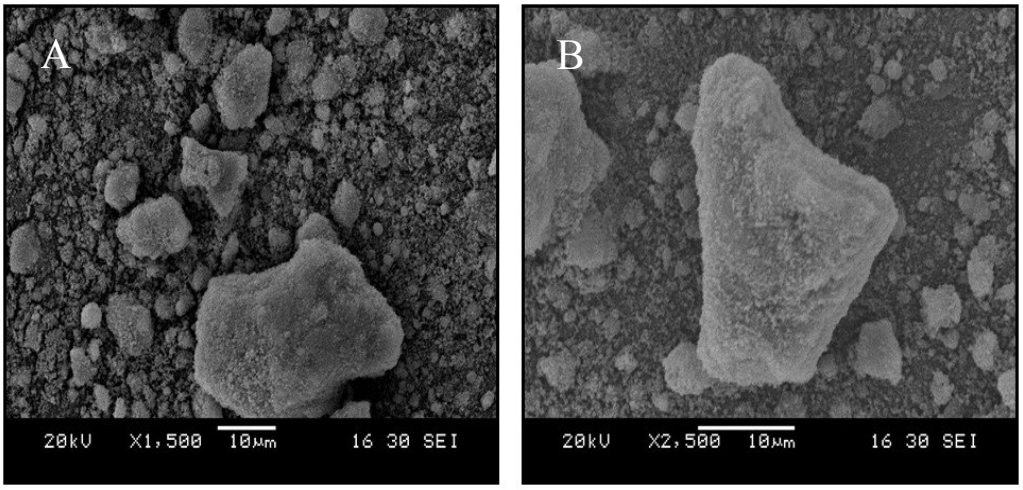


Figure 3.4 *Scanning Electron Microscope (SEM) images of mesoporous TiO_2/Fe_2O_3 binary mixed oxides (MB) at different magnifications (A) x1,500 (B) x2,500 presenting porous surfaces and size distribution of MB produced by studied method*

The MB prepared by the MT-mediated technology was also characterized by SEM which confirmed that both Ti and Fe minerals are exposed on the surface of the material (see Figure 3.4). Figure 3.4 (A) and (B) show the porosity of MB surface and the size distribution. There are both Ti and Fe on the surface. Fe mineral has particle size in micrometer and Ti has particle size in nanometer. From Figure 3.4, the images show the particle of mesoporous Ti on the surface of Fe mineral. It can be confirmed that this simple synthetic method can be used to produce TiO_2/Fe_2O_3 binary mixed oxides. The porous surface can also increase adsorption capacity of MB.

3.3.2 BET surface area and pore size of mesoporous TiO_2 (MT) and mesoporous TiO_2/Fe_2O_3 binary mixed oxides (MB)

The total surface area of the binary mixed oxides is one of the key parameters that dictates the adsorption capacity of materials. Therefore, it can be used to approximate the surface active sites of the binary mixed oxides available for the

binding of arsenic. The BET surface area of MB was determined and compared with other materials from literature (see Table 3.2). The BET surface areas of mesoporous TiO_2 and mesoporous TiO_2/Fe_2O_3 binary mixed oxides are 113 and 63 m^2 g^{-1}, respectively. The pore size of mesoporous TiO_2 and binary mixed oxides are 8.6 and 10.2 nm, respectively.

Table 3.2 *BET surface area and pore size of mesoporous TiO_2, Fe_2O_3 and mesoporous TiO_2/Fe_2O_3 binary mixed oxides*

Materials	BET surface area (m^2 g^{-1})	Pore size (nm)	Ref.
Mesoporous TiO_2 anatase (synthesized)	112.9	8.6	This work
TiO_2 anatase (commercial)	133.5	-	[1]
TiO_2 anatase	134.0	8.3	[48]
Degussa P25 TiO_2 (*80% anatase, 20% rutile*)	50	21	[20]
Mesoporous TiO_2/Fe_2O_3 binary mixed oxides	63.1	10.2	This work
Co-precipitated TiO_2/Fe_2O_3 bicomposites	41.7	-	[1]
Mesoporous TiO_2/Fe_2O_3 bicomposites	95.0	-	[2]
Fe_2O_3	45.0	-	[2]
Fe_2O_3-Ti_2O_3 bimetal mixed oxide	77.8	11.0	[7]

Table 3.2 suggests that the BET surface area of mesoporous TiO_2 decrease after precipitation of Fe_2O_3 onto mesoporous TiO_2 surface. The BET surface areas of mesoporous TiO_2 in this work and TiO_2/Fe_2O_3 binary mixed oxides found at 112.9 and 63.1 m^2 g^{-1}. The surface area of the binary mixed oxides is less than the pure TiO_2. This is likely to be due to the precipitation of Fe_2O_3 on-to mesoporous TiO_2 decreasing the overall surface area of the material. In contrast, the pore size of mesoporous TiO_2 increased from 8.6 to 10.2 nm after formation

of binary mixed oxides. Additonally, the calcination process with higher temperature may change some TiO_2 anatase to rutile. Mixing TiO_2 anatase and rutile has more pore size than pure TiO_2 anatase [20]. The results in Table 3.2, show that Degussa P25 TiO_2 (80% anatase, 20% rutile) has large pore size at 20 nm and low BET surface area at 50 m^2 g^{-1} [20].

The BET surface area of mesoporous TiO_2 in this work is lower than commercial TiO_2 anatase. Because of TiO_2 that was prepared in this work found a small mixing of TiO_2 rutile. The XRD result in Figure 3.3 shows a small peak of TiO_2 rutile found at $2\theta = 32.0^o$. It may be make BET surface area in this work less than previous work [2].

BET surface areas of TiO_2/Fe_2O_3 binary mixed oxides in Table 3.2 of this work and previous work [1, 2, 7] were different due to the different sources of TiO_2 used to synthesis binary mixed oxides; also some steps in the preparation process were different. The binary mixed oxides prepared in this work has BET surface area and pore size very similar to those reported in previous work [7].

3.3.3 Adsorption isotherms of As^{III} on mesoporous TiO_2/Fe_2O_3 binary mixed oxides

The adsorption capacity of a sorbent is typically assessed using adsorption isotherms plotting the amounts of adsorbate adsorbed on the surface of adsorbent at constant temperature. Different isotherms models have been developed - but the Langmuir and Freundlich adsorption models are the most generally applied to evaluate the adsorption of analyte from a liquid phase onto a solid phase [1, 51-53]. The Langmuir model assumes that the solid surface is identical and one adsorbed molecule binds with one surface active site to form an adsorption mono-layer. Surface active sites are limited, therefore the adsorption declines at saturated point. The maximum capacity of the Langmuir isotherm is expressed by the following equation.

$$q_e = \frac{Q_{max}\, b\, C_e}{1 + b\, C_e}, \qquad (3.1)$$

where, C_e is the equilibrium concentration of adsorbate in solution (mg L^{-1}), q_e is the adsorption capacity, i.e. the amount of adsorbed analyte on the solid sorbent, at equilibrium (mg g^{-1} sorbent). Q_{max} is the maximum adsorption capacity (mg g^{-1} sorbent) and b is a constant (L mg^{-1}). Equation (3.1) can be re-written as (3.2):

$$\frac{C_e}{q_e} = \frac{1}{Q_{max}} + \frac{C_e}{Q_{max}} \qquad (3.2)$$

The Freundlich adsorption model, on the other hand, represents the adsorption of analyte on unlimited surface active sites. This model assumes that the analyte can bind to the surface of the solid sorbent without limit (equations 3.3 and 3.4).

$$q_e = K_f C_e^{1/n} \qquad (3.3)$$

$$\log q_e = \frac{1}{n} \log C_e + \log K_f \qquad (3.4)$$

The linear equation of log q_e as a function of log C_e can be applied to estimate K_f (adsorption capacity, mg g^{-1}) and 1/n from the intercept of log K_f and slope of straight lines. These two values are considered relative indicators of adsorption capacity and adsorption intensity, respectively [1, 51-54].

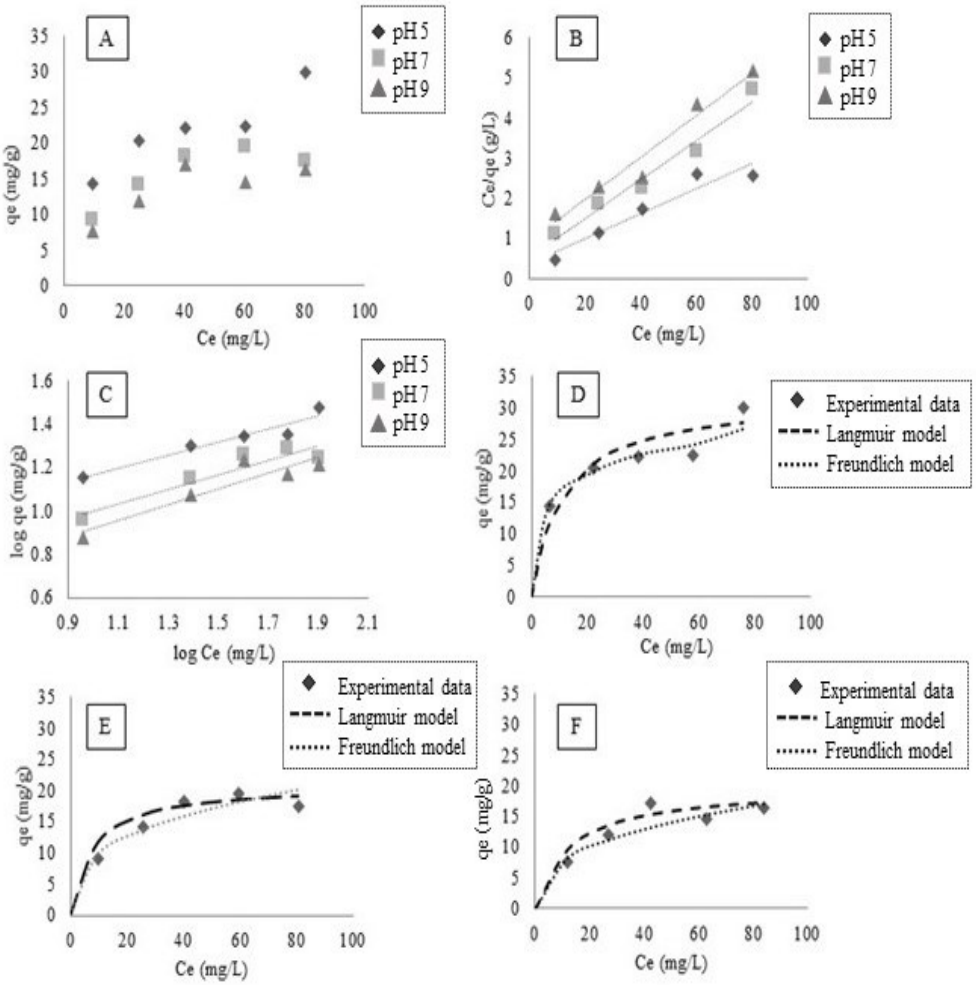


Figure 3.5 *Results of As^{III} adsorption on mesoporous TiO_2/Fe_2O_3 binary mixed oxides, As^{III} concentration ranged from 20 to 100 mg L^{-1} and sorbent concentration was 1 g L^{-1} in 0.01 M acetate buffer pH 5, 0.01 M HEPES buffer pH 7 and 0.01 M borate buffer pH 9 at temp. 25 ^{o} C (298 K), the plots show the average data from three replications of experiments, (±SD found in between 0.03 to 5.61), (A) adsorption isotherm plots at pH 5, pH 7 and pH 9, (B) Langmuir isotherm plots at pH 5, pH 7and pH 9 , (C) Freundlich isotherm plots at pH 5, pH 7 and pH 9. The experimental data plots were compared with the Langmuir and Freundlich models calculations at (D) pH 5, (E) pH7 and (F) pH 9.*

Table 3.3 *The Langmuir and Freundlich parameters for As^{III} adsorption isotherms on TiO_2/Fe_2O_3 binary mixed oxides in 0.01 M acetate buffer pH 5, 0.01 M HEPES buffer pH 7 and 0.01 M borate buffer pH 9 at temp. 25 ° C (298 K) (BET surface area of MB = 63.1 m^2 g^{-1})*

pH	Langmuir parameters					Freundlich parameters		
	Q_{max} (mg g^{-1})	Q_{max} (mg m^{-2})	Q_{max} (μmol m^{-2})	b (L mg^{-1})	R^2	K_f (mg g^{-1})	n (g L^{-1})	R^2
5	29.44±2.99	0.47±0.05	6.21±0.66	0.11±0.07	0.927	8.47±2.64	3.94±0.95	0.784
7	22.64±1.74	0.36±0.03	4.81±0.37	0.08±0.03	0.968	4.06±1.15	2.63±0.14	0.878
9	21.60±0.33	0.35±0.01	4.61±0.09	0.05±0.01	0.943	2.46±0.75	2.18±0.25	0.839

Adsorption performance of As^{III} on MB at pH 5, 7 and 9 at 25ºC were evaluated by employing the Langmuir and Freundlich adsorption isotherm models (Figure 3.5(A)). The adsorption of As^{III} on MB modelled by the Langmuir (Figure 3.5(B)), and Freundlich (Figure 3.5(C)) equations and experimental results are compared in Figure 3.5(D), (E), (F) and Table 3.3, which presents all model calculated parameters. The experimental data were fitted very well with the Langmuir model with R^2 between 0.927 to 0.968 in all pH conditions. The Langmuir adsorption capacities (Q_{max}) of As^{III} on MB are not much different at the different pH studied. This is not surprising since at pH below 9 As^{III} is primarily found as uncharged H_3AsO_3 species. The isotherm model can also provide insight into the possible mechanism of As^{III} adsorption on MB. The Langmuir model assumes that As^{III} can feasibly form mono-layer on limited surface active sites of MB which result in the plots reaching the plateau at equilibrium. In case of the Freundlich pattern, As^{III} can adsorb on unlimited surface active sites with multi-adsorption layer which can observe the slowly increase of adsorption plot. The adsorption behaviour of As^{III} on MB in these experimental conditions can better describe by the Langmuir model which agree with the previous research [7] that reported As^{III} adsorbed on Fe^{III}/Ti^{IV} binary mixed oxides.

The results above suggest that the interaction of As^{III} with the surface of MB involves the formation of a mono-adsorption layer. The adsorption capacities (Q_{max}) calculated by using the Langmuir model were found at 29.44±2.99, 22.64±1.74 and 21.60±0.33 mg g^{-1} at pH 5, 7 and 9, respectively. The Langmuir model indicate that As^{III} can adsorb on the surface of MB by forming monolayer. Additionally, As^{III} adsorption capacities at pH 5, 7 and 9 were similar suggesting that there is no pH dependency in this pH range.

In contrast to the little changes observed for the capacities between pH 5 and 9, we observed a significant decrease at pH 12. The adsorption amounts of As^{III} found around 17.76±1.31, 17.27±0.27, 14.82±1.69 and 8.79±1.65 mg g^{-1} at pH 5, 7, 9 and 12, respectively. This can be explained in the terms of As^{III} protonation state and charges on the adsorbent surface at different pH values. In the pH range between 0 and 9, As^{III} ions present themselves in the form of un-charge or zero-charge species, i.e. the fully protonated species H_3AsO_3 [1, 2, 22]; at values higher than pH 9, the arsenite is only partially protonated species, i.e. $H_2AsO_3^-$. The point of zero charge (PZC) of MB is between 7 and 9 which results from the combination of TiO_2 (anatase) which has PZC at 6.8 ± 0.2 and Fe_2O_3 (hematite) which found PZC at 8.0 ± 1.0 [56-58]. At pH lower than pH_{PZC}, the surface of MB is positively charge (pH < 7) but at pH > $pH_{PZC,}$ the surface is negatively charged Therefore, at pH > 9, As^{III} mainly present as $H_2AsO_3^-$ and hence there is a large electrostatic repulsion with the negative surface charge of MB reducing significantly the amount of As being adsorbed. As^{III} adsorption on MB at various pH ranges in this work show the similar adsorption mechanism compared with many studies on mixed oxides [2, 7, 8].

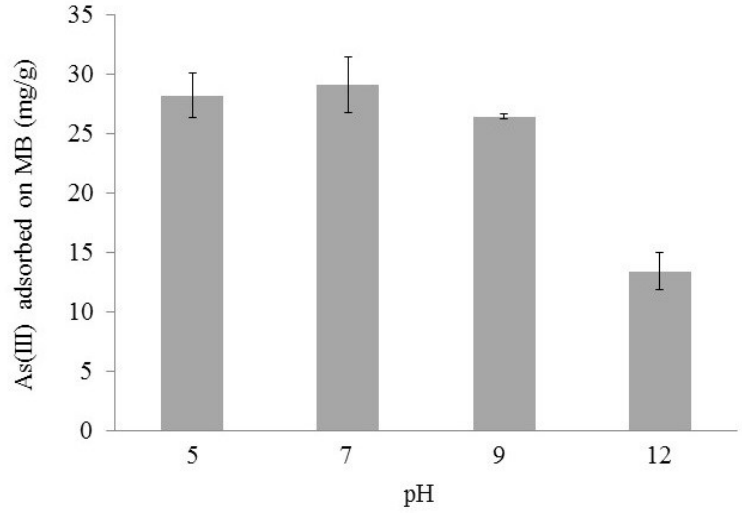


Figure 3.6 *Effect of pH on As^{III} adsorption on 1 g L^{-1} MB at 298 K at pH 5, 7, 9 and 12 using initial concentration of 40 mg L^{-1} (±SD calculated from three replication experiments)*

3.3.4 Evidence of competitive adsorption of As^{III} and phosphate on MB

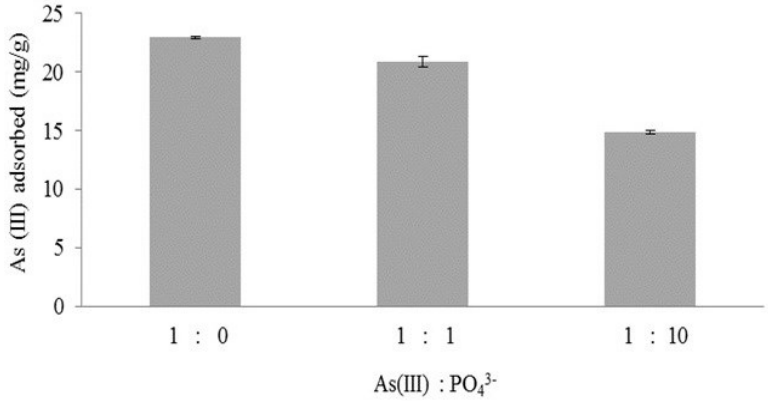


Figure 3.7 *Competitive adsorption of mixed As^{III} and phosphate (40 mg L^{-1}) solution on MB (As^{III} : Phosphate, 1:0, 1:1 and 1:10 mass ratio) at pH 7 and 298 K (±SD calculated from three replication experiments)*

Natural ground water has various types of oxyanion such as SO_4^{2-}, CO_3^{2-}, SiO_3^{2-} and PO_4^{3-} which may disturb arsenic oxyanion adsorption onto MB. Therefore, several previous studied with metal oxides have focused on the effect of co-existing oxyanions on arsenic removal [12, 30]. In particular, it has been found that phosphate is a strong competitor since it has the same number of oxygens, structure and very similar acid-base properties to arsenate. As described in Chapter 1, arsenic oxyanion are found as H_3AsO_4, $H_2AsO_4^-$, $HAsO_4^{2-}$, AsO_4^{3-} for arsenate and H_3AsO_3, $H_2AsO_3^-$, $HAsO_3^{2-}$, AsO_3^{3-} for arsenite, depending on the pH. Phosphate oxyanion presents in the form of H_3PO_4, $H_2PO_4^-$, HPO_4^{2-}, PO_4^{3-} which can interfere the adsorption of arsenic on the surface of the bicopmosites [1, 12]. Therefore, we were interested in studying the competitive effect of phosphate on As^{III} adsorption on MB. Figure 3.7 summarises the results of arsenic adsorption onto MB using solution containing only As^{III} and two different mixtures of As^{III} with phosphate (1:1 and 1:10 by mass). There is a decrease in the capacity of MB to bind As^{III} as the phosphate increases: 22.94±0.01 mg g^{-1} for the phosphate-free solution, 20.86±0.46 mg g^{-1} for the 1:1 solution (performance: 91.23% as compared to phosphate-free solution) and 14.87±0.18 mg g^{-1} for the 1:10 solution, (performance: 66.04% as compared to phosphate-free solution). These results clearly show that phosphate competes with As^{III} for binding sites on MB and therefore the performance of this material to remove As^{III} will decreases for water with a high phosphate content [1, 15].

3.3.5 Determination of the active sites of the MB

Determining the number of surface active sites on a given material's surface is important in order to estimate the adsorption capacity of the materials because arsenic adsorption reaction takes place on the surface of materials. In this work, the active sites on the MB surface were calculated using the method previously reported for hematite (Fe_2O_3) by Koretsky et al., [60]. They reported a method for estimating surface sites of oxide minerals by consideration of crystal surfaces

and calculated the number of surface sites per area (nm^2) (the most simple experimental method used in their work was acid-base titration). Moreover, they indicate the calculated numbers of surface sites of hematite by the method assuming that each bond (Fe-O) counted as one surface site. They found the surface sites of hematite ranging from 4.5 -27.3 sites nm^{-2} (or $4.5 \times 10^{18} – 2.73 \times 10^{19}$ sites m^{-2}). Therefore, this work used this hematite site calculation as reference to estimate the surface sites of the mixed oxide samples. The results from BET surface analysis found surface area of the MB synthesised in this work at 63.1 $m^2\ g^{-1}$ and from the model, hematite has 4.5-27.3 sites nm^{-2}(or $4.5 \times 10^{18} – 2.73 \times 10^{19}$ sites m^{-2}). Then, we used this information to calculate the theoretical sites on the MB which are shown in Table 3.4.

Table 3.4 *Surface active site of MB theoretical calculation by using hematite as reference model [60]*

Metal Oxide	Calculated number of active sites		
Hematite (Fe_2O_3) (Reference model)	4.5 – 27.3 sites nm^{-2} (or $4.5 \times 10^{18} – 2.73 \times 10^{19}$ sites m^{-2})		
MB (TiO_2/Fe_2O_3)	BET surface area ($m^2\ g^{-1}$)	Theoretical calculation	
		MB surface active sites	As-binding on MB sites
	63.11±0.51	$2.84\times10^{20} – 1.72\times10^{21}$ sites g^{-1}	0.035–0.215 g g^{-1} 35–215 mg g^{-1} $5.55\times10^{-4}–3.41\times10^{-3}$ g m^{-2}
		$4.50\times10^{18} – 2.70\times10^{19}$ sites m^{-2}	0.55–3.41 mg m^{-2} 7.40-45.51 µmol m^{-2}

Table 3.4 shows the number of theoretical surface active sites on MB calculated using MB's experimentally BET surface area (i.e. 63.11±0.51 $m^2\ g^{-1}$). These calculations show that the number of surface active sites on MB ranges between 4.50×10^{18} to 2.70×10^{19} sites m^{-2}. With this, it is also possible to estimate the amounts of bound arsenic, i.e. between 0.55 and 3.41 mg m^{-2} (or between 35 and

215 mg of As/g of material). From the experimental data in the adsorption isotherm studies found As^{III} adsorption capacities at 29.44±2.99, 22.44±1.74 and 21.60±0.33 mg g^{-1} at pH 5, 7 and 9, respectively. The adsorption capacities of As^{III} from adsorption experiment found close to the theoretical calculation of bound arsenic on MB active sites (adsorption capacity from theoretical calculation found 35 mg g^{-1} and from our experiment found maximum around 29.44±2.99 mg g^{-1}, pH 5).

Table 3.5 *MB surface active sites calculated from the Langmuir adsorption capacities*

Theoretical calculation		Experimental results calculation					
Surface active sites	As binding on MB sites	As adsorbed on MB			MB surface active sites		
		pH 5	pH 7	pH 9	pH 5	pH 7	pH 9
$2.84x10^{20}$ Sites/g	35 mg/g	29.44 mg/g	22.64 mg/g	21.60 mg/g	$2.39x10^{20}$ sites/g	$1.83x10^{20}$ sites/g	$1.75x10^{20}$ sites/g
$4.50x10^{18}$ Site/m^2	0.55 mg/m^2	0.47 mg/m^2	0.36 mg/m^2	0.35 mg/m^2	$3.85x10^{18}$ sites/m^2	$2.95x10^{18}$ sites/m^2	$2.86x10^{18}$ sites/m^2
	7.70 µmol/m^2	6.21 µmol/m^2	4.81 µmol/m^2	4.61 µmol/m^2	$3.63x10^{18}$ sites/m^2	$2.81x10^{18}$ sites/m^2	$2.69x10^{18}$ sites/m^2

The adsorption capacities of As^{III} on MB estimated by the Langmuir adsorption model were used to calculate MB active sites. The results in Table 3.5 presents the surface active sites of MB calculated by using the Langmuir adsorption capacities of As^{III} on MB at equilibrium (24 h). The calculation of results found the MB surface active sites in between $1.75x10^{20}$ to $2.39x10^{20}$ sites g^{-1} or $2.69x10^{18}$ to $3.85x10^{18}$ sites m^{-2}. This information can be used to predict the amount of MB needed for effective As^{III} removal process.

3.3.6 Adsorption Kinetics

The adsorption rate of As^{III} on the binary mixed oxides can be used to predict, design and control the water treatment process. Furthermore, the adsorption kinetics can describe the adsorption mechanism of As^{III} on the binary mixed oxides about the diffusion from aqueous solution to the surface and pore of the binary mixed oxides with different kinetic rate. In this section, the adsorption kinetics of As^{III} on MB are presented. This was studied by using a pseudo first and pseudo second order kinetic models. Additionally, the diffusion mechanism and kinetics of As^{III} adsorption onto MB was explained by intra-particle diffusion kinetic model. The pseudo first order kinetic model [12-16] can be determined by the Lagergren equation, which is depicted as:

$$\frac{dq}{dt} = k_1 (q_e - q_t) \qquad (3.5)$$

where q_e and q_t are the quantity of arsenic adsorbed on adsorbent at equilibrium and at time t (min), respectively and k_1 is the rate constant of the pseudo first order sorption (min^{-1}). The integrated form of equation (3.5) can be presented as:

$$\log(q_e - q_t) = log q_e - \frac{k_1}{2.303}\, t \qquad (3.6)$$

The pseudo second order kinetic rate equation is given as:

$$\frac{d_q}{d_t} = k_2 (q_e - q_t)^2 \qquad (3.7)$$

where k_2 is the pseudo second order rate constant (g $mg^{-1}min^{-1}$). The equation (3.7) can be integrated to give:

$$\frac{t}{q_t} = \frac{1}{k_2 q_e^2} + \frac{1}{q_e}\, t \qquad (3.8)$$

The intercept of the linear equation can be used to determine the k_2 value.

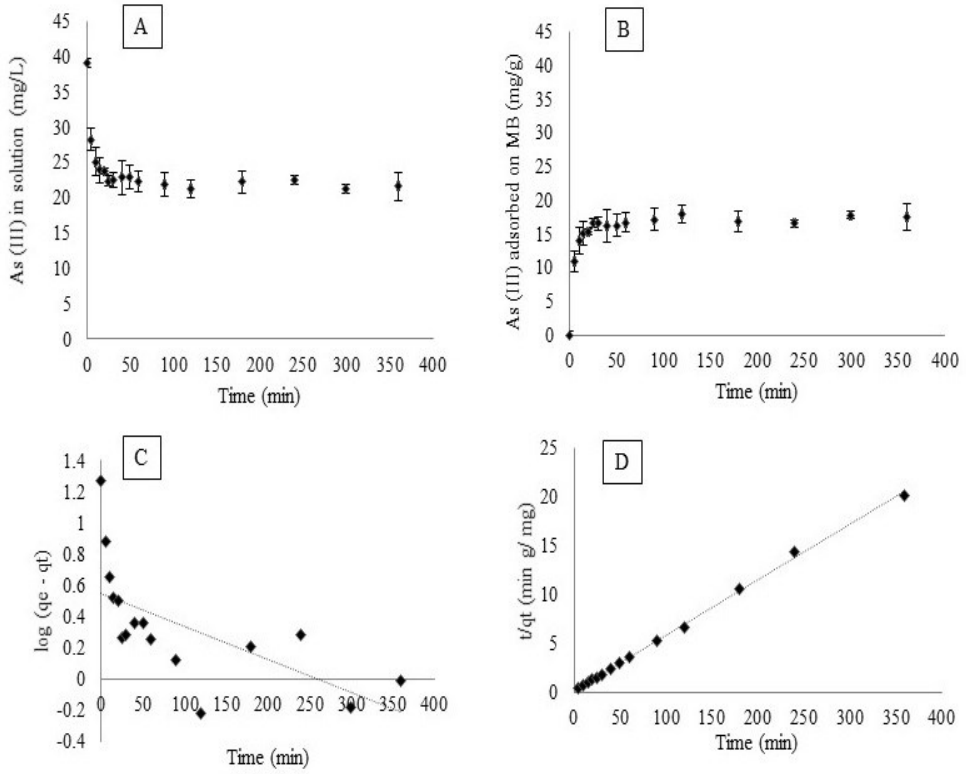


Figure 3.8 *As^{III} adsorption kinetics on MB at different times in 0.01 M HEPES buffer pH 7 (298 K) with initial As^{III} concentration 40 mg L^{-1} and MB concentration 1 g L^{-1}. As^{III} concentration in solution decrease very fast in the first 15 min and slowly decrease until reach equilibrium. (A) As^{III} concentration in solution (mg L^{-1}) determined by voltammetry, (B) amounts of As^{III} adsorbed on MB (mg g^{-1}), (C) the experimental data fitted with the pseudo-first order model and (D) the pseudo-second order model*

Figure 3.8(A) and 3.8(B) present the decrease of As^{III} concentration in solution and the concomitant increase of As^{III} adsorbed on MB as a function of time. The adsorption isotherm in Figure 3.8(A) and 3.8(B) demonstrates that within the first 5 min, As^{III} adsorbs very rapidly while after 25 min, it adsorbs at a significantly slower rate. The results are in agreement with previous work on arsenic adsorption on Ti/Fe binary mixed oxides [1, 7]. The results from this experiment were fitted with various kinetic models to investigate the rate of As^{III} adsorption

on MB. The data from this experiment were modelled with pseudo-first order equation expressed as follows,

$$\log(q_e - q_t) = \log q_e - \frac{k_1}{2.303} t \qquad (3.9)$$

in which, q_e and q_t are the amount of As^{III} adsorbed on MB (mg g^{-1}) at equilibrium and time t (min), respectively, k_1 represent the pseudo-first order adsorption kinetic constant in unit of min^{-1}. By plotting log ($q_e - q_t$) against t, it is possible to estimate the kinetic rate constant (k_1) and adsorption capacity (q_e). Figure 3.8(C) illustrates the pseudo-first order kinetic plots of As^{III} adsorption on MB. The low linearity R^2 value of 0.42 show that the pseudo-first order model is not suitable to estimate the kinetic adsorption rate (k_1) and adsorption capacity ($q_{e,cal}$) of As^{III} adsorption on MB.

Therefore, the pseudo-second order equation stated as follows was also applied.

$$\frac{t}{q_t} = \frac{1}{k_2 q_e^2} + \left(\frac{1}{q_e}\right) t \qquad (3.10)$$

where, k_2 (g mg^{-1} min^{-1}) is the rate constant of the pseudo-second order adsorption, q_e is the amount of As^{III} adsorption on MB (mg g^{-1}). Figure 3.8(D) displays an excellent fit (R^2 = 0.99) consistent with a pseudo-second model with the experimental data. The straight line can examine the pseudo-second rate constant (k_2) by the interception and adsorption capacity ($q_{e,cal}$) by slope.

Table 3.6 *The kinetic parameters of 40 mg L^{-1} As^{III} adsorption on 1 g L^{-1} MB in 0.01 M HEPES buffer pH 7 at 25°C (298 K)*

Model	Equation	Parameters,(unit)	As^{III}-MB
Pseudo-first order kinetic	$\log(q_e - q_t) = \log q_e - (\frac{k_1}{2.303}) \times t)$ Slope = $-\frac{k_1}{2.303}$, Intercept = $\log q_e$	$q_{e,cal}$ k_1 (min^{-1}) R^2	3.56 0.01 0.42
Pseudo-second Order kinetic	$\frac{t}{q} = \frac{1}{k_2 q_e^2} + (\frac{1}{q_e}) \times t$ Slope = $\frac{1}{q_e}$, Intercept = $\frac{1}{k_2 q_e^2}$ Initial adsorption rate (h), $h = k_2\, q_e^2$	$q_{e,cal}$ k_2 (g mg^{-1} min^{-1}) R^2 h (mg g^{-1} min^{-1})	17.54 0.02 0.999 6.993

The kinetic model parameters are depicted in Table 3.6. The results found in this work are in an agreement with previous reports [1, 7, 12] that suggest that the adsorption kinetic rate of arsenic on Ti^{IV}/Fe^{III} [12] and TiO_2/Fe_2O_3 bicomposites [1] follow a pseudo second order rate.

The previous work reported by D'Arcy et al., [1] presented the adsorption of As^V on TiO_2/Fe_2O_3 bicomposite with the modified two pathway rate law (the intra-particle diffusion model) and separate the observation range in two different time portions, early/rapid and later/slow reaction which can identify the kinetic rate of arsenic adsorption more accurately. Moreover, Goswami et al., [59] explained the adsorption kinetics of As^{III} on Cu^{II} oxide nanoparticle by using intra-particle diffusion kinetic model. This models describes the kinetic rate in three stages of reaction and the diffusion of As^{III} into pore of Cu^{II} oxide nanoparticle. They found that the adsorption rate of reaction is high at the bingining of the reaction and decreases as a time function until equilibrium. Therefore, the intra-particle

diffusion kinetic model can be used to accurately determine the adsorption rate of reaction at each portion of times.

In this section, the intra-particular diffusion kinetic model was used to identify the adsorption rate at three different stages of reaction (early, middle and later stages of reaction) and describe the adsorption the diffusion of As^{III} into the pore of MB. Additionally, intra-particle diffusion kinetic model can be applied to explain the kinetic adsorption with multi- linear step kinetic adsorption (see Figure 3.9) and the rate of mass transfer can be illustrated as a function of the square root of time ($t^{0.5}$). This kinetic model equation [59] can be presented by:

$$q_t = k_{IPD}\, t^{0.5} + I \qquad (3.11)$$

where, q_t represents adsorbate adsorption at time t ($min^{0.5}$), k_{IPD} is the intra-particle diffusion rate constant (mg g^{-1}. $min^{-0.5}$) and I represents the intercept (adsorption capacity, mg g^{-1}).

The intra-particle diffusion (IPD) model has been utilised in previous work [1] and also applied in this work. The IPD is a very successfully kinetic model used to specify the adsorption of a multi-step adsorption process in Figure 3.9.

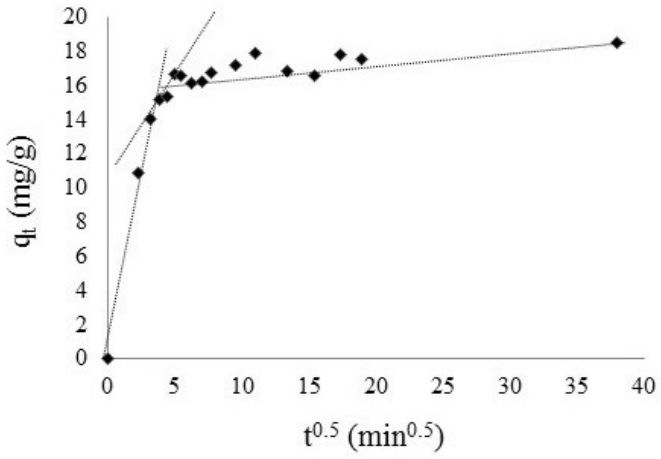


Figure 3.9 *The intra-particle diffusion (IDP) model for As^{III} adsorption on MB at pH 7 (25 °C)*

The plots in Figure 3.9 illustrate a multi-linear at different times which show similar results to previous report about arsenic adsorption on Cu^{II} oxide nanoparticle presented by Goswami et al., [59]. Cu^{II} has surface area of 52.11 m^2 g^{-1} and the Langmuir adsorption capacity of As^{III} found at 1.082 mg g^{-1}. MB produced in this work has surface area 63.1 m^2 g^{-1} and the Langmuir adsorption capacity of As^{III} found in between 21.60±0.33 (pH 9) to 29.44±0.33 (pH 5) mg g^{-1}. The results show MB has surface area and As^{III} adsorption capacity higher than Cu^{III}. The kinetic absorption data of As^{III} on MB is shown in Figure 3.9 is similar to that one reported previous work [59].

Table 3.7 *Intra-particle diffusion kinetic model parameters of 40 mg L^{-1} As^{III} adsorption on 1 g L^{-1} MB in 0.01 M HEPES buffer pH 7 at 25°C*

Adsorption reaction	Model equation	R^2	k_{IPD} (mg g^{-1} $min^{0.5}$)	I (mg g^{-1})	$q_{t,cal}$ (mg g^{-1})
Early reaction 0-10 min	$q_t = k_{IPD}\, t^{0.5} + I$	0.995	4.52	0.16	14.46
Middle reaction 10-20 min		0.997	1.43	9.56	15.96
Later reaction 25-1440 min		0.624	0.06	16.25	18.63

The three linear portions were separately fitted at different stages. The modelled data in Table 3.7 show that in the early stage of adsorption reaction (0-10 min). MB has the highest adsorption rate of As^{III} and this rate reduces as time goes by. The different rate of adsorption kinetic of As^{III} on MB at three different stages resulted from the specific adsorption mechanism at each one (Figure 3.10). In the rapid reaction (Figure 3.9), the slope of the plots is highest which is represent the diffusion of As^{III} from the bulk of solution to outer surface of MB. The initial

concentration of As ^{III} is highest (at t = 0 min) and all the surface active sites of MB are vacant, therefore the reaction is fastest. In the middle stage, the reaction rate is lower than at the early reaction stage and slowly decrease to equilibrium point at the later reaction stage. All slope information can be applied to identify the rate of adsorption. From the plots in Figure 3.9, there are three processes that control the rate of As^{III} adsorption but only one process is the rate limiting. The early stage is the fastest and is controlled by the diffusion of As^{III} in bulk phase to the external surface of MB. The middle stage is likely to be associated to the diffusion of As^{III} into the mesopores while the later stage has the lowest rate due to the diffusion of As^{III} into the micropores. This study can assume that the later stage is the rate-limiting stage in the adsorption of As^{III} on the surface of MB, especially over long period of adsorption.

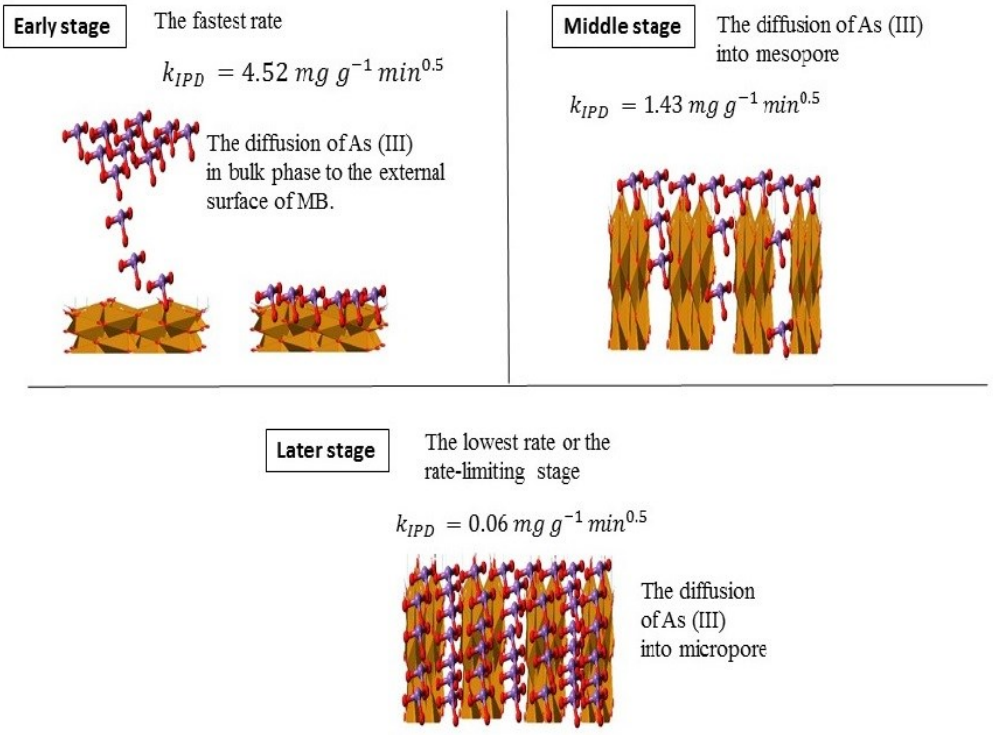


Figure 3.10 *Proposed As^{III} adsorption mechanism on the surface of MB describes by intra-particle diffusion kinetic model. The rate of adsorption relates to the diffusion of As^{III} from the solution to MB pore.*

3.3.7 Continuous flow system for scavenging of arsenic

As discussed in detail in the introduction, there are a wide range of different set-ups to for arsenic removal with absorbing materials [63]. Among these, column are most frequently applied for arsenic removal by packing sand [64, 65], iron oxide [66], nanomagnetite [67], soil [68], metal oxide nanoparticle [69], TiO_2 [70] or chitosan [71]. Mixed oxides (i.e. iron-manganese nanostructured materials) have also been reported as packing materials for column studies to improve the removal of arsenic [72], iron mineral-quartz sand [73], zerovalent iron-sand [74] and iron oxide coated sand [75]. Having established the arsenic adsorption properties of the different mixed oxide materials in batch (see previous sections), it was of interest to establish whether these materials would be suitable for continuous flow removal of arsenic as part of a column set up.

3.3.7.1 Effect of pH solution on As^V removal

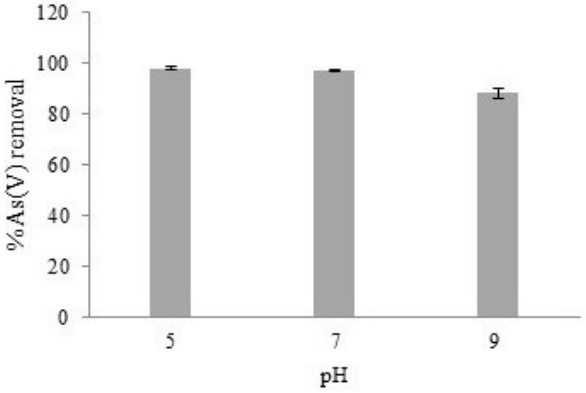
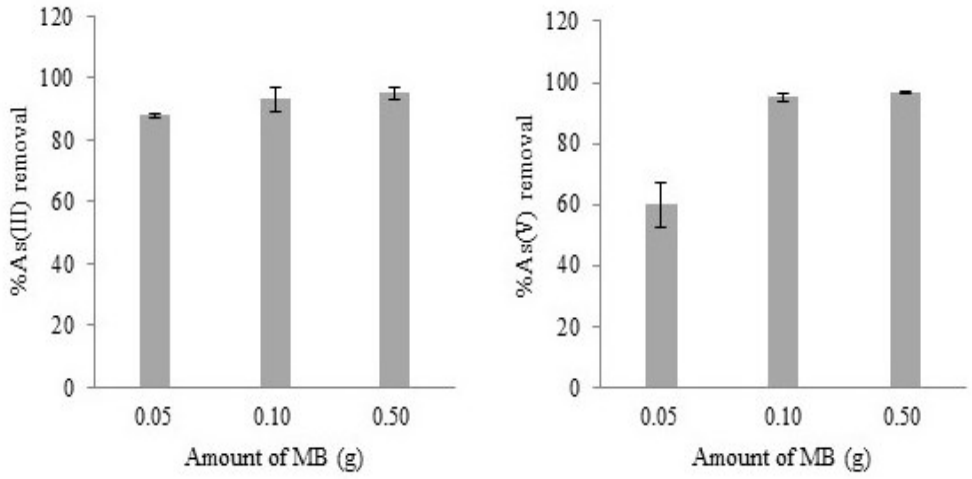


Figure 3.11 *Removal of 100 µg L^{-1} As^V using 0.5 g MB column at pH 5, 7 and 9 with solution flow rate at 1 mL min^{-1}. (±SD calculated from three replications of measurement)*

Figure 3.11 presents the percentages of As^V removal on 0.5 g MB column at pH 5, 7 and 9. At all pH points, the MB-packed column was shown to remove over 88% of As^V from aqueous solutions. The highest and the lowest removal point found at pH 5 and 9, respectively. Considering these results, pH 7 was selected to carry out further flow experiments.

3.3.7.2 Effect of MB amount on As^{III} and As^V removal

This experiment aims to test MB column on 100 µg L^{-1} arsenic removal at different amount of MB (or different volumes of MB). MB at 0.05, 0.10 and 0.50 g (0.13, 0.26, 0.66 cm^3 MB volumes) were used to study in this experiment.



(A) (B)

Figure 3.12 *Removal of 100 µg L^{-1} arsenic from solution by using different amounts of MB packed in column at pH 7 with 1 mL min^{-1}. Comparison of percent (A) As^{III} and (B) As^V removal using 0.05, 0.10, and 0.50 g MB column (±SD calculated from three repeats)*

The results in Figure 3.12 show that the percentage removal with 0.10 g (0.26 cm^3) and 0.50 g (0.66 cm^3) packed column were higher than 93% of both As^{III} and As^{V}. At this point, 0.10 g MB column was selected for further experiments. As already been shown in the batch experiments (see section 3.3.3) the amount of MB can affect the percent removal of an increase in the total surface active sites of MB.

3.3.7.3 Effect of flow rate on As^{V} removal

Optimising the contact time between the arsenic-contaning solutions and the MB packed in column is important to maximize the removal of arsenic. Therefore, several flow rates were studied in this experiment. As^{V} samples at concentration 100 µg L^{-1} were passed through 0.1 g MB column with different flow rates such as 1.0, 2.0 and 4.0 mL min^{-1}.

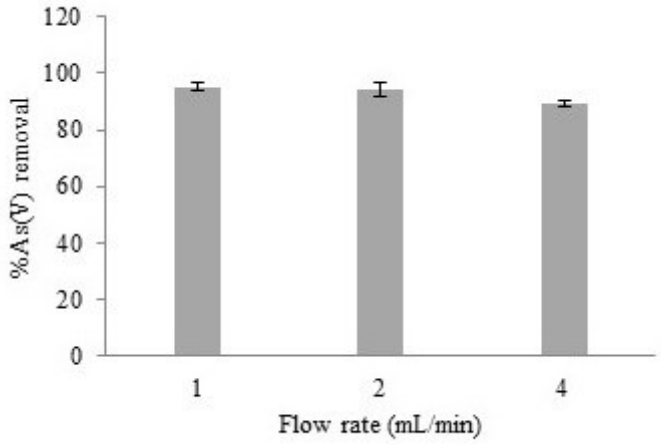


Figure 3.13 *Results of solution flow rates effect on 100 µg L^{-1} As^{V} removal using 0.1 g MB column at pH 7 (±SD calculated from three replications of measurement)*

Figure 3.13 shows the effect of flow rate on the percent removal of As^V by MB packed in a column. The highest percent removal at flow rate of 1 and 2 mL min^{-1} was practically the same while at, 4 mL min^{-1} this was lower. Thus, for further studies, we decided to use a flow rate of 2 mL min^{-1}.

3.3.7.4 MB column regeneration

A recycle of materials is considered to be a cost effective process for water treatment plants. Regeneration of γ-Fe_2O_3 /TiO_2 have been reported by Yu et al., [11] using 0.1 M NaOH solution in batch experiment. We explored regeneration of our MB columns by passing 50 mL of 0.1 M NaOH solution through 0.1g MB column with a flow rate of 2.0 mL min^{-1} to desorb arsenic. This was followed by a wash with 50 mL Milli-Q water to rinse the column again. The percentages of arsenic removal were used to examine the number of times that the material can be regenerated and re-used for effective As removal.

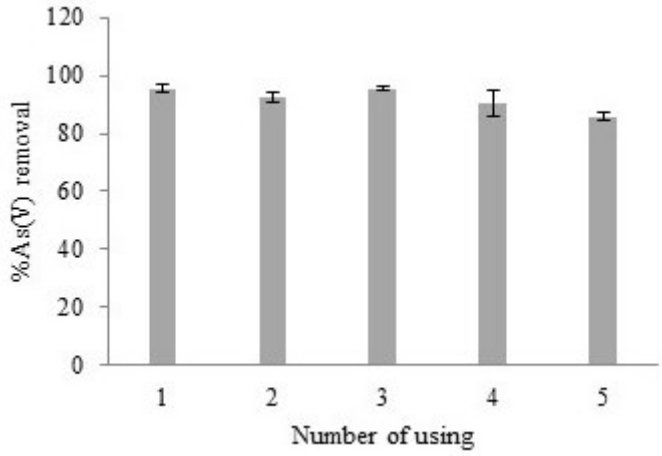


Figure 3.14 *Recycle of 0.1 g MB column for 100 µg L^{-1} As^V removal at pH 7, comparison of percent As^V removal over five uses (±SD calculated from three replications of measurement)*

As can be seen in Figure 3.14, we were able to regenerate and re-use the material five times without significant lose of capacity (in all cases 85% As removal was observed). When 0.1 M NaOH solutions passed through the MB column, it is likely that the hydroxyl group occupy the sites on MB where arsenic is adsorbed which leads to desorption of the arsenic and regeneration of the column. Additionally, at high pH values (pH > pH_{PZC} of MB) the surface charge of MB and arsenic species present in the form of negative charge. Therefore, the negative charge repulsion between arsenic species and surface charge of MB is found resulting in the less adsorption at high pH values. The results from these MB regeneration experiments are summarized in Table 3.8.

Table 3.8 *The optimum conditions for arsenic removal from aqueous solutions by using MB column with continuous flow system*

Parameters	Optimum conditions
Arsenic conc.	100 µg L^{-1}
pH	5, 7
Amount	0.10 g MB
Flow rate	2.0 mL min^{-1}
%Removal	85%
Recycle	At least 5 times

3.4 Conclusion

Mesoporous- TiO_2/Fe_2O_3 binary mixed oxides prepared by using in-lab synthesised mesoporous TiO_2 (anatase) co-precipitate with Fe_2O_3 (hematite) has the highest adsorption capacity for arsenic removal comparing with CP- and SG -TiO_2/Fe_2O_3 bicomposite materials [5]. The Langmuir isotherm model is the one that explains better the adsorption of As^{III} onto this material. Our data measured at several pH values (between 5 and 9) show that this material has adsorption capacities ranging between 21.60±0.33 (pH 9) and 29.99±2.99 (pH 5) mg g^{-1}.

The adsorption reaction was very fast in the first 10 min and approach equilibrium within 25 min. The experimental data fitted very well with a pseudo-second order kinetic model. The intra-particle diffusion kinetic model describes very well the adsorption mechanism of As^{III} on the surface of MB with three different stages of kinetic rates; these studies also show that the first stage has the highest adsorption rate.

The data herein presented suggests that this binary mixed oxide material can in principle be applied to remove As^{III} from contaminated water which is consistent with previously reported studies.

References

(1) D'Arcy, M.; Weiss, D.; Bluck, M.; Vilar, R. *J. Colloid Interface Sci.* **2011**, *364*, 205-212.

(2) Zhou, W.; Fu, H.; Tian, C.; Qu, Y.; Lu, P.; Sun, C. C. *J. Phys. Chem. C*. **2008**, *112*, 19584-19589.

(3) Trapalis, C. C.; Keivanidis, P.; Kordas, G.; Zaharescu, M.; Crisan, M.; Szatvanyi, A.; Gartner, M. In *Thin Solid Films*; **2003**, *433*, 186-190.

(4) Zhu, J.; Zheng, W.; He, B.; Zhang, J.; Anpo, M. *J. Mol. Catal. A Chem.* **2004**, *216*, 35-43.

(5) Bullough, F.; Berry, A.; Weiss, D.; Vilar, R. *PhD transfer report*. **2012**.

(6) Zhang, F. S.; Itoh, H. *Chemosphere*. **2006**, *65*, 125-131.

(7) Gupta, K.; Ghosh, U. C. *J. Hazard. Mater.* **2009**, *161*, 884-892.

(8) Gupta, K.; Basu, T.; Ghosh, U. C. *J. Chem. Eng. Data*. **2009**, *54*, 2222-2228.

(9) Smith, Y. R.; Joseph Antony Raj, K.; Ravi Subramanian, V.; Viswanathan, B. *Colloids Surfaces A Physicochem. Eng. Asp.* **2010**, *367*, 140-147.

(10) Liu, H.; Shon, H. K.; Sun, X.; Vigneswaran, S.; Nan, H. *Applied Surface Science*. **2011**, *257*, 5813-5819.

(11) Li, Y.; Liu, J. R.; Jia, S. Y.; Guo, J. W.; Zhuo, J.; Na, P. *Chem. Eng. J.* **2012**, *191*, 66-74.

(12) Yu, L.; Peng, X.; Ni, F.; Li, J.; Wang, D.; Luan, Z. *J. Hazard. Mater.* **2013**, *246*, 10-17.

(13) Pantoja, M. L.; Jones, H.; Garelick, H.; Mohamedbakr, H. G.; Burkitbayev, M. *Environ. Sci. Pollut. Res.* **2014**, *21*, 495-506.

(14) Chen, L.; Xin, H.; Fang, Y.; Zhang, C.; Zhang, F.; Cao, X.; Zhang, C.; Li, X. *Journal of Nanomaterials*. **2014**.

(15) Lu, J.; Liu, D.; Hao, J.; Zhang, G.; Lu, B. *Chem. Eng. Res. Des.* **2015**, *93*, 652-661.

(16) Dutta, P. K.; Ray, A. K.; Sharma, V. K.; Millero, F. J. *J. Colloid Interface Sci.* **2004**, *278*, 270-275.

(17) Bang, S.; Patel, M.; Lippincott, L.; Meng, X. *Chemosphere*. **2005**, *60*, 389-397.

(18) Pena, M. E.; Korfiatis, G. P.; Patel, M.; Lippincott, L.; Meng, X. *Water Res.* **2005**, *39*, 2327-2337.

(19) Liang, P.; Liu, R. *Anal. Chim. Acta*. **2007**, *602*, 32-36.

(20) Sun, H.; Zhang, X.; Zhang, Z.; Chen, Y.; Crittenden, J. C. *Environ. Pollut.* **2009**, 157, 1165-1170.

(21) Nabi, D.; Aslam, I.; Qazi, I. A. *J. Environ. Sci.* **2009**, 402-408.

(22) Na, P.; Jia, X.; Yuan, B.; Li, Y.; Na, J.; Chen, Y.; Wang, L. *J. Chem. Technol. Biotechnol.* **2010**, *85*, 708-714.

(23) Xu, Z.; Li, Q.; Gao, S.; Shang, J. K. *Water Res.* **2010**, *44*, 5713-5721.

(24) Miller, S. M.; Spaulding, M. L.; Zimmerman, J. B. *Water Res.* **2011**, *45*, 5745-5754.

(25) Pirilä, M.; Martikainen, M.; Ainassaari, K.; Kuokkanen, T.; Keiski, R. L. *J. Colloid Interface Science.* **2011**, *353,* 257-262.

(26) Guan, X.; Du, J.; Meng, X.; Sun, Y.; Sun, B.; Hu, Q. *Journal of Hazardous Materials*. **2012**, *215*, 1-16.

(27) Zhan, H.; Jiang, Y.; Ma, Q. *Anal. Lett.* **2014**, *47*, 871–884.

(28) Zeng, H.; Fisher, B.; Giammar, D. E. *Environ. Sci. Technol.* **2008**, *42*, 147-152.

(29) Kanematsu, M.; Young, T. M.; Fukushi, K.; Green, P. G.; Darby, J. L. *Geochim. Cosmochim. Acta.* **2013***, 106*, 404-428.

(30) Roy, P. K.; Choudhury, M. R.; Ali, M. A. *Int. J. Chem. Environ. Eng.* **2013**, *4*.

(31) Saharan, P.; Chaudhary, G. R.; Mehta, S. K.; Umar, A. *J. Nanosci. Nanotechnol.* **2013**, *14*, 627–643.

(32) Mohan, D.; Pittman, C. U. *Journal of Hazardous Materials*. **2007**, *142*, 1-53.

(33) Bissen, M.; Vieillard-Baron, M. M.; Schindelin, A. J.; Frimmel, F. H. *Chemosphere*. **2001**, *44*, 751-757.

(34) Lee, H.; Choi, W. *Environ. Sci. Technol*. **2002**, *36*, 3872-3878.

(35) Ryu, J.; Choi, W. *Environ. Sci. Technol.* **2004**, *38*, 2928-2933.

(36) Dutta, P. K.; Pehkonen, S. O.; Sharma, V. K.; Ray, A. K. *Environ. Sci. Technol.* **2005**, 39, 1827-1834.

(37) Nakajima, T.; Xu, Y. H.; Mori, Y.; Kishita, M.; Takanashi, H.; Maeda, S.; Ohki, A. *J. Hazard. Mater.* **2005**, *120*, 75-80.

(38) Xu, Z.; Meng, X. *J. Hazard. Mater.* **2009**, *168*, 747-752.

(39) Choi, W.; Yeo, J.; Ryu, J.; Tachikawa, T.; Majima, T. *Environ. Sci. Technol.* **2010**, *44*, 9099-9104.

(40) Li, X.; Leng, W. *Electrochem. commun.* **2012**, *22*, 185-188.

(41) Yu, X.; Liu, S.; Yu, J. *Appl. Catal. B Environ.* **2011**, *104*, 12–20.

(42) Slimen, H.; Houas, A.; Nogier, J. P. *J. Photochem. Photobiol. A Chem.* **2011**, *221*, 13–21.

(43) Peng, Y. H.; Huang, G. F.; Huang, W. Q. *Adv. Powder Technol.* **2012**, *23*, 8-12.

(44) He, M.; Li, D.; Jiang, D.; Chen, M. *Journal of Solid State Chemistry*. **2012**, *192*, 139-143.

(45) Shi, H.; Zhang, T.; An, T.; Li, B.; Wang, X. *J. Colloid Interface Sci.* **2012**, 380, 121-127.

(46) Li, F. T.; Zhao, Y.; Hao, Y. J.; Wang, X. J.; Liu, R. H.; Zhao, D. S.; Chen, D. M. *J. Hazard. Mater.* **2012**, *239*, 118-127.

(47) Bagwasi, S.; Tian, B.; Zhang, J.; Nasir, M. *Chem. Eng. J.* **2013**, *217*, 108-118.

(48) Liu, K.; Fu, H.; Shi, K.; Xiao, F.; Jing, L.; Xin, B. *J. Phys. Chem. B*. **2005**, *109*, 18719-18722.

(49) Carreon, M. A.; Choi, S. Y.; Mamak, M.; Chopra, N.; Ozin, G. A. *Journal of Materials Chemistry*.

2007, *17*, 82-89.

(50) Coakley, K. M.; McGehee, M. D. *Chemistry of Materials*. **2004**, *16*, 4533-4542.

(51) Watkins, R.; Weiss, D.; Dubbin, W.; Peel, K.; Coles, B.; Arnold, T. *J. Colloid Interface Sci.* **2006**, *303*, 639–646.

(52) Bullough, F.; Weiss, D. J.; Dubbin, W. E.; Coles, B. J.; Barrott, J.; Sengupta, A. K. *Ind. Eng. Chem. Res*. **2010**, *49*, 2521-2524.

(53) Wainipee, W.; Weiss, D. J.; Sephton, M. A.; Coles, B. J.; Unsworth, C.; Court, R. *Water Res.* **2010**, *44*, 5673-5683.

(54) Liu, Y. *J. Chem. Eng. Data*. **2009**, *54*, 1981-1983.

(55) Singh, T. S.; Pant, K. K. *Sep. Purif. Technol.* **2004**, *36*, 139–147.

(56) Dutta, P. K.; Ray, A. K.; Sharma, V. K.; Millero, F. J. *J. Colloid Interface Sci.* **2004**, *278*, 270-275.

(57) Parks, G. a.; Bruyn, P. L. De. *J. Phys. Chem.* **1962**, *66*, 967–973.

(58) Fernández-Ibáñez, P.; De Las Nieves, F. J.; Malato, S. *J. Colloid Interface Sci.* **2000**, *227*, 510–516.

(59) Goswami, A.; Raul, P. K.; Purkait, M. K. *Chem. Eng. Res. Des.* **2012**, *90*, 1387–1396.

(60) Koretsky, C.M.; Sverjensky, D.A.; Sahai, N. *American Journal of Science*. **1998**, 298, 349-438.

(61) Yang, H.; Sun, W.; Ge, H.; Yao, R. *Environ. Technol.* **2015**, 1-8.

(62) Lescano, M.; Zalazar, C.; Brandi, R. *Environ. Sci. Pollut. Res.* **2015**, *22*, 3865-3875.

(63) Singh, R.; Singh, S.; Parihar, P.; Singh, V. P.; Prasad, S. M. *Ecotoxicol. Environ. Saf.* **2014**, *112*, 247–270.

(64) Trois, C.; Cibati, A. *Chem. Eng. J.* **2015**, *259*, 981-989.

(65) Altun, M.; Sahinkaya, E.; Durukan, I.; Bektas, S.; Komnitsas, K. *J. Hazard. Mater.* **2014**, 269, 31-37.

(66) Azhdarpoor, A.; Nikmanesh, R.; Samaei, M. R. *Environ. Technol.* **2015**, *36*, 2525-2531.

(67) Farrell, J. W.; Fortner, J.; Work, S.; Avendano, C.; Gonzalez-Pech, N. I.; Zá Rate Araiza, R.; Li, Q.; Lvarez, P. J. J.; Colvin, V.; Kan, A.; Tomson, M. *Environ. Eng. Sci.* **2014**, *31*, 393-402.

(68) Carro Perez, M. E.; Francisca, F. M. *J. Environ. Eng.* **2013**, 788-795.

(69) Hristovski, K.; Baumgardner, A.; Westerhoff, P. *J. Hazard. Mater.* **2007**, 147, 265-274.

(70) Huang, C.; Hu, B.; Jiang, Z. *Spectrochim. Acta - Part B At. Spectrosc.* **2007**, *62*, 454–460.

(71) Benavente, M.; Arévalo, M.; Martínez, J. *Water Pract. Technol.* **2006**, 1.

(72) Kong, S.; Wang, Y.; Zhan, H.; Yuan, S.; Liu, M.; Zhou, C. *Environ. Eng. Sci.* **2013**, *30*, 689-696.

(73) Guo, H.; Stüben, D.; Berner, Z. *Sci. Total Environ.* **2007**, *377*, 142-151.

(74) Leupin, O. X.; Hug, S. J.; Badruzzaman, A. B. M. *Environ. Sci. Technol.* **2005**, *39*, 8032-8037.

(75) Thirunavukkarasu, O. S.; Viraraghavan, T.; Subramanian, K. S. *Water Air and Soil Pollution*. **2003**, *142*, 95-111.

Chapter 4

Binding mode of arsenic oxides onto the surface of TiO_2/Fe_2O_3 binary mixed oxides

The binding modes of arsenic oxides onto the surface of co-precipitated (CP)-, mesoporous (MB)- and sol-gel (SG) - TiO_2/Fe_2O_3 binary mixed oxides were investigated using X-ray absorption spectroscopy (XAS). The initial oxidation state of arsenic on TiO_2/Fe_2O_3 binary mixed oxides was confirmed using X-ray absorption near edge structure spectroscopy (XANES). The geometries of arsenic oxides adsorbed to the surface of the different binary mixed oxides were investigated using extended X-ray absorption fine structure spectroscopy (EXAFS). These studies indicated that the arsenic binds to the TiO_2/Fe_2O_3 binary mixed oxides as a bidentate mononuclear edge sharing (^2E) complex and bidentate binuclear corner sharing (^2C) complex. The binding mode was found to be the same at adsorption pH of 5, 7, and 9. We also carried out adsorption kinetic studies which showed that there is no effect on the molecular structure of the adsorbed arsenic on the binary mixed oxides at adsorption time 2 and 24 hours and also found the same geometry of arsenic surface complexes. Additionally, the studies show that the three types of TiO_2/Fe_2O_3 binary mixed oxides (i.e. CP, MB and SG) under study can adsorb arsenic via the same binding mode.

4.1 Introduction

Nanostructure Fe^{III}-Ti^{IV} binary mixed oxides reported by Gupta and Ghosh [1] have the ability to remove arsenic from contaminated water. The adsorption energy of arsenic onto the binary mixed oxide surface has been previously calculated using the Dubinin-Radushkevich model and found to be higher for As^{V} than for As^{III}. The interaction of As^{V} on the surface of nanostructure Fe^{III}-Ti^{IV} binary mixed oxides has been proposed to be via chemisorption. In addition, the adsorption mechanism of As^{V} on co-precipitated TiO_2/Fe_2O_3 bicomposites reported by D'Arcy et al., [2] found the interaction of As^{V} on the bicomposites in the form of chemisorption which is similar to the report of Gupta and Ghosh [1]. Furthermore, this study found that the bifunctional TiO_2-Fe_2O_3 bicomposites displays a rapid adsorption rate in the initial stages of the adsorption process and slow rate after 2 h until equilibrium point at 24 h.

Mixed Ti and Fe oxides including slag-Fe-TiO_2 adsorbent [3] and mesoporous TiO_2/Fe_2O_3 bicomposites [4] have also been used for effective removal of As^{III} from contaminated water. The removing process in these cases used UV light to improve the remediation process through photocatalytic oxidation of As^{III} to As^{V} and subsequently adsorbed on their surfaces [3, 4].

While the use of Fe-Ti mixed metal oxides to remove arsenic is now well documented, there is very limited information of the detailed binding mode of arsenate and arsenite to these materials. Several previous reports have used adsorption models to rationalize the data. But yet, very little information is known at an atomic level. The adsorption of arsenic on the surface of Fe oxide or Ti oxide (but not bi-composites) have been previously studied using extended X-ray absorption fine structure (EXAFS) [5-27].

EXAFS is a technique that can be used to estimate the interatomic distances of arsenic with the atoms present in the metal oxides; in addition, it can also give insights into the geometry of arsenic once adsorbed onto the metal oxide surfaces.

Previously, Sherman and Randall [5] presented the possible complexes of arsenate on the surface of goethite and proposed different types of binding modes between As^V and the metal oxide surface (see Figure 4.1).

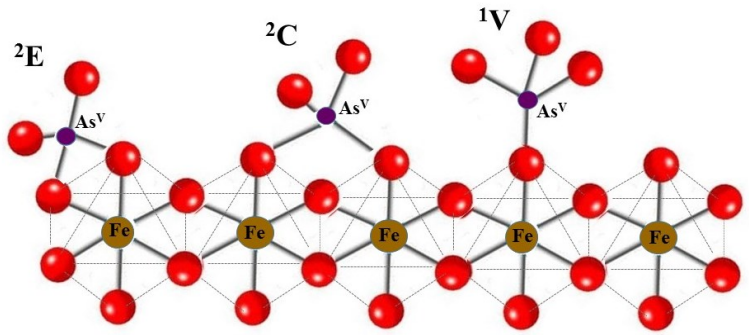


Figure 4.1 *Possible binding modes of AsO_4^{3-} upon adsorption onto the surface of goethite (α-FeOOH), ^1V is a monodentate mononuclear corner sharing complex with an As-Fe distance of around 3.6 Å; ^2C is a bidentate binuclear corner sharing complex with an As-Fe distance of around 3.26 Å; ^2E is a bidentate mononuclear edge-sharing complex with an As-Fe distance of around 2.8 Å; Figure taken from Sherman and Randall [5].*

This EXAFS study found that arsenate $(AsO_4)^{3-}$ strongly adsorbed onto α-Fe_2O_3 and α-, γ- FeOOH. Three possible surface binding modes between tetrahedral AsO_4 and FeO_6 were proposed: bidentate binuclear corner sharing (^2C), bidentate mononuclear edge-sharing (^2E) and monodentate mononuclear corner sharing (^1V) (see Figure 4.1). A different EXAFS analysis by Fendorf et al., [6] described the molecular structure of arsenate (As^V) on the surface of goethite (α-FeOOH). The EXAFS analysis results based on As^V-Fe distance specify the geometry of As^V on goethite surface in three different surface complexes including a mono-dentate complex, a bidentate-binuclear complex and a bidentate-mononuclear complex. At low surface coverages, the mono-dentate surface complex is favored while at high surface coverages the bidentate-binuclear complex is the main binding mode. Additionally, the surface structure of As^{III} on goethite surface was studied by Manning et al., [7]. The EXAFS spectra indicated As^{III} formed

bidentate binuclear surface complexes on goethite. The complexation of As^{III} on goethite is similar to other oxyanions which adsorb on the surface of goethite by an inner-sphere mechanism. Furthermore, Manning et al., [8] described the adsorption mechanism of As^{III} and As^{V} on zerovalent iron (Fe^{0}) surfaces using EXAFS analysis. The interatomic distances of As-Fe at 3.30-3.36 Å were attributed to inner-sphere, bidentate As^{III} and As^{V} surface complexes.

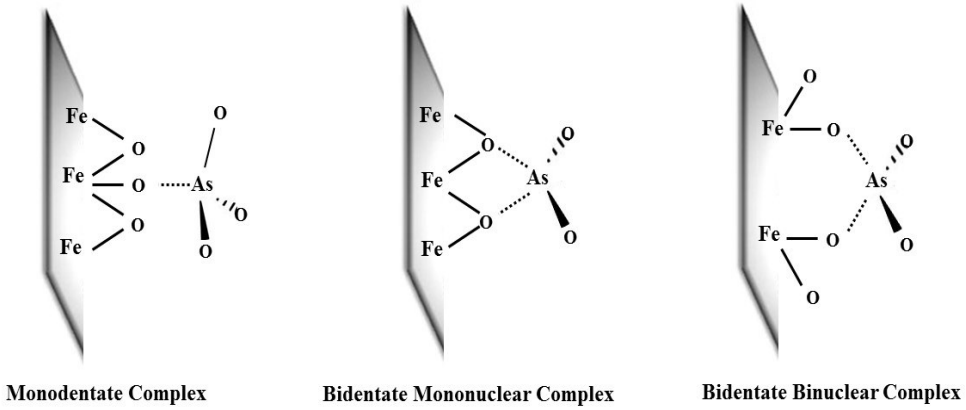


Figure 4.2 *The surface structure of As^{V} adsorption on goethite, Figure taken from Fendorf et al., [6].*

The adsorption mechanism of As^{III} onto two-line ferrihydrite, hematite, goethite and lepidocrocite were reported by Ona-Nguema et al., [9]. The EXAFS analysis indicates that As^{III} form similar inner sphere complexes on ferrihydrite and hematite surfaces. At high surface coverage, As^{III} form bidentate mononuclear edge sharing (^{2}E) on ferrihydrite and bidentate binuclear corner sharing (^{2}C) on hematite, goethite and lepidocrocite.

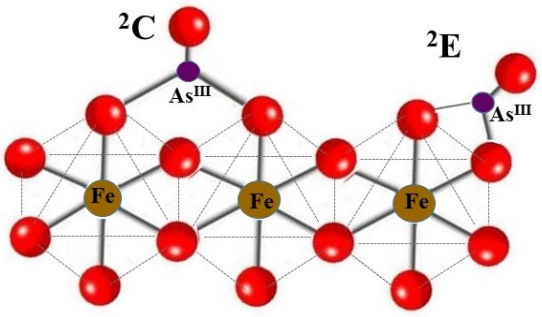


Figure 4.3 *As^{III} adsorption complexes on the surface of hematite (α-Fe$_2$O$_3$), ^{2}C is bidentate binuclear corner sharing complex, ^{2}E is bidentate mononuclear edge-sharing complex, Figure taken from Ona-Nguema et al., [9].*

As^{III} and As^{V} adsorption complexes onto the surface of nanocrystalline TiO_2 were previously reported by Pena et al., [10] and Jegadeesan et al., [11] and found that both As^{III} and As^{V} form only bidentate binuclear corner sharing (^{2}C) complexes on TiO_2 surfaces in contrast to the wider range of binding modes observed with iron oxides.

The geometries of arsenic on iron oxides and titanium dioxide from the literature can be used to forecast the binding modes of arsenic onto the surface of these metal oxides. The interatomic distances and the geometric types of arsenic surface complexes from literature are summarized in Table 4.1.

Table 4.1 *The interatomic distances and surface complexes of arsenic on Fe or Ti metal oxides*

Sample	pH	Interatomic shell	R(Å)	Geometry of surface complex	Ref.
As^{III}-fougerite	9.6	As^{III}-O	1.78	Arsenite trigonal pyramidal molecule	[14]
		As^{III}-Fe	3.43	Bidentate binuclear corner sharing (^{2}C)	
As^{III}-goethite	7.4	As^{III}-O	1.79±0.02	Arsenite trigonal pyramidal molecule	[7]
		As^{III}-Fe	3.38±0.01	Bidentate binuclear corner sharing (^{2}C)	
As^{III}-goethite	3.0	As^{III}-O	1.76	Arsenite trigonal pyramidal molecule	[14]
		As^{III}-Fe	3.33	Bidentate binuclear corner sharing (^{2}C)	
As^{III}-goethite	9.9	As^{III}-O	1.76	Arsenite trigonal pyramidal molecule	[14]
		As^{III}-Fe	3.34	Bidentate binuclear corner sharing (^{2}C)	
As^{III}-goethite	7.0	As^{III}-O	1.76±0.03	Arsenite trigonal pyramidal molecule	[27]
		As^{III}-Fe	3.33±0.03	Bidentate binuclear corner sharing (^{2}C)	
As^{III}-goethite	7.0	As^{III}-O	1.76±0.03	Arsenite trigonal pyramidal molecule	[27]
		As^{III}-Fe	3.33±0.03	Bidentate binuclear corner sharing (^{2}C)	
As^{III}-hematite	7.4	As^{III}-O	1.76±0.03	Arsenite trigonal pyramidal molecule	[9]
		As^{III}-Fe_1	2.89±0.03	Bidentate mononuclear edge sharing (^{2}E)	
		As^{III}-Fe_2	3.36±0.03	Bidentate binuclear corner sharing (^{2}C)	
As^{III}-iron(0)	5	As^{III}-O	1.70±0.06	Arsenite trigonal pyramidal molecule	[8]
		As^{III}-Fe_1	3.08±0.06	Bidentate mononuclear edge sharing (^{2}E)	
		As^{III}-Fe_2	3.39±0.06	Bidentate binuclear corner sharing (^{2}C)	
As^{III}-iron hydroxide	7.0	As^{III}-O	1.77	Arsenite trigonal pyramidal molecule	[21]
		As^{III}-Fe	3.37	Bidentate binuclear corner sharing (^{2}C)	
As^{III}-maghemite	7.5	As^{III}-O	1.77±0.03	Arsenite trigonal pyramidal molecule	[12]
		As^{III}-Fe_1	2.90±0.03	Bidentate mononuclear edge sharing (^{2}E)	
		As^{III}-Fe_2	3.45±0.03	Bidentate binuclear corner sharing (^{2}C)	
As^{III}-maghemite nanoparticle	7.0	As^{III}-O	1.76±0.02	Arsenite trigonal pyramidal molecule	[22]
		As^{III}-Fe	3.41±0.02	Bidentate binuclear corner sharing (^{2}C)	
As^{III}-magnetite	7.0	As^{III}-O	1.79	Arsenite trigonal pyramidal molecule	[14]
		As^{III}-Fe	3.39	Bidentate binuclear corner sharing (^{2}C)	
As^{III}magnetite	7.1	As^{III}-O	1.78±0.02	Arsenite trigonal pyramidal molecule	[19]
		As^{III}-Fe	3.50±0.05	Bidentate binuclear corner sharing (^{2}C)	
As^{III}-siderite	7.0	As^{III}-O	1.71±0.03	Arsenite trigonal pyramidal molecule	[27]
		As^{III}-Fe	3.35±0.03	Bidentate binuclear corner sharing (^{2}C)	
As^{III}-titanium	4-12	As^{III}-O	1.77	Arsenite trigonal pyramidal molecule	[10]
		As^{III}-Ti	3.35	Bidentate binuclear corner sharing (^{2}C)	
As^{III}-titanium	4-9	As^{III}-O	1.76±0.02	Arsenite trigonal pyramidal molecule	[11]
		As^{III}-Ti	3.33±0.02	Bidentate binuclear corner sharing (^{2}C)	
As^{V}-ferrihydrite	-	As^{V}-O	1.68	Arsenate tetrahedral molecule	[16]
		As^{V}-Fe	3.46	Bidentate binuclear corner sharing (^{2}C)	

Table 4.1 (Continued) *The interatomic distances and surface complexes of arsenic on Fe or Ti metal oxides*

Sample	pH	Interatomic shell	R(Å)	Geometry of surface complex	Ref.
As^V-ferric hydroxide	7.4	As^V-O As^V-Fe	1.65±0.01 3.32±0.01	Arsenate tetrahedral molecule Bidentate binuclear corner sharing (^{2}C)	[13]
As^V-fougerite	9.3	As^V-O As^V-Fe	1.69 3.43	Arsenate tetrahedral molecule Bidentate binuclear corner sharing (^{2}C)	[14]
As^V-goethite	4.0	As^V-O As^V-Fe_1 As^V-Fe_2 As^V-Fe_2	1.67 2.85 3.24 3.60	Arsenate tetrahedral molecule Bidentate mononuclear edge sharing (^{2}E) Bidentate binuclear corner sharing (^{2}C) Monodentate mononuclear (^{1}V)	[6]
As^V-goethite	4.0	As^V-O As^V-Fe	1.69 3.30	Arsenate tetrahedral molecule Bidentate binuclear corner sharing (^{2}C)	[14]
As^V-goethite	7.0	As^V-Fe	3.3	Bidentate binuclear corner sharing (^{2}C)	[25]
As^V-goethite	7.0	As^V-O As^V-Fe	1.69±0.03 3.34±0.03	Arsenate tetrahedral molecule Bidentate binuclear corner sharing (^{2}C)	[27]
As^V-hematite	4.0	As^V-O As^V-Fe_1 As^V-Fe_2	1.70 2.85 3.26	Arsenate tetrahedral molecule Bidentate mononuclear edge sharing (^{2}E) Bidentate binuclear corner sharing (^{2}C)	[5]
As^V-hematite	7.0	As^V-Fe	3.3	Bidentate binuclear corner sharing (^{2}C)	[25]
As^V-iron(0)	5	As^V-O As^V-Fe_1 As^V-Fe_2	1.69±0.06 3.05±0.06 3.36±0.06	Arsenate tetrahedral molecule Bidentate mononuclear edge sharing (^{2}E) Bidentate binuclear corner sharing (^{2}C)	[8]
As^V-iron(0)	5	As^V-O As^V-Fe_1 As^V-Fe_2	1.69±0.06 3.05±0.06 3.36±0.06	Arsenate tetrahedral molecule Bidentate mononuclear edge sharing (^{2}E) Bidentate binuclear corner sharing (^{2}C)	[8]
As^V-iron hydroxide	7.0	As^V-O As^V-Fe_1 As^V-Fe_2	1.68 2.86 3.28	Arsenate tetrahedral molecule Bidentate mononuclear edge sharing (^{2}E) Bidentate binuclear corner sharing (^{2}C)	[21] [4.17]
As^V-maghemite	7.5	As^V-O As^V-Fe	1.69±0.03 3.35±0.03	Arsenate tetrahedral molecule Bidentate binuclear corner sharing (^{2}C)	[12]
As^V-magnetite	10.6	As^V-O As^V-Fe	1.69 3.42	Arsenate tetrahedral molecule Bidentate binuclear corner sharing (^{2}C)	[14]
As^V-magnetite	7.1	As^V-O As^V-Fe	1.69±0.02 3.33±0.05	Arsenate tetrahedral molecule Bidentate binuclear corner sharing (^{2}C)	[19]
As^V-siderite	6.2	As^V-O As^V-Fe	1.69 3.35	Arsenate tetrahedral molecule Bidentate binuclear corner sharing (^{2}C)	[14]
As^V-siderite	8.4	As^V-O As^V-Fe	1.69 3.36	Arsenate tetrahedral molecule Bidentate binuclear corner sharing (^{2}C)	[14]

Table 4.1 (Continued) *The interatomic distances and surface complexes of arsenic on Fe or Ti metal oxides*

Sample	pH	Interatomic shell	R(Å)	Geometry of surface complex	Ref.
As^V-siderite	7.0	As^V-O As^V-Fe	1.69±0.03 3.35±0.03	Arsenate tetrahedral molecule Bidentate binuclear corner sharing (^{2}C)	[27]
As^V-titanium	4-12	As^V-O As^V-Ti	1.69 3.30	Arsenate tetrahedral molecule Bidentate binuclear corner sharing (^{2}C)	[10]
As^V-titanium	4-9	As^V-O As^V-Ti	1.69±0.01 3.34±0.01	Arsenate tetrahedral molecule Bidentate binuclear corner sharing (^{2}C)	[11]
As^V-titanium	7.0	As^V-O As^V-Ti	1.69 3.34	Arsenate tetrahedral molecule Bidentate binuclear corner sharing (^{2}C)	[15]

The geometries of arsenic adsorption complexes in Table 4.1 are divided in two groups, As^{III} and As^V, which interact with Fe or Ti atom on different kinds of materials including ferrihydrite [16], fougerite [14], goethite [7, 14, 27], hematite [9], iron hydroxide [8, 21], maghemite [12, 14], magnetite [14, 19], siderite [27] and titanium [10]. From all these reports, it can be concluded that the interatomic distances at around 1.71-1.79 Å identify the distance between As^{III} and oxygen atom in arsenite trigonal pyramidal molecule. For As^V, the interatomic distances at around 1.65-1.69 Å indicate the distance between As^V and oxygen atom in arsenate tetrahedral molecule. The geometric types of arsenic adsorption complexes on iron oxides or titanium oxide found mainly in two types, bidentate mononuclear edge sharing (^{2}E) and bidentate binuclear corner sharing (^{2}C), which are indicated by the interatomic distances presenting in Table 4.1. These interatomic distances can be used as referent values to indicate the geometry of arsenic adsorption complex on TiO_2/Fe_2O_3 binary mixed oxides.

In this chapter, the molecular structure of arsenic adsorption on TiO_2/Fe_2O_3 binary mixed oxides are described based on EXAFS analysis results. Furthermore, the interatomic distance of As-Fe and As-Ti indicating the surface complexes are presented in the results and discussion.

4.2 Aims and objectives

As discussed in previous chapters, TiO_2/Fe_2O_3 binary mixed oxides synthesized using commercial TiO_2 anatase co-precipiated with Fe_2O_3 demonstrated to be good adsorbents for As^V. The adsorption isotherm model reported by D'Arcy et al., [2] suggested that As^V forms a monolayer upon adsorption onto the TiO_2/Fe_2O_3 bicomposites and that the process involves chemisorption. It was also found that the arsenic is adsorbed at different rates depending on the time of exposure. This could be related to different binding modes of the arsenic on the surface of the binary mixed oxides. While the adsorption model can forecast the adsorption mechanism and possible surface complexes of arsenic on the TiO_2/Fe_2O_3 binary mixed oxides, it can provide an atomistic picture of the binding mode. Therefore, the aim of the research presented in this chapter is to provide atomistic insights into the molecular structure of arsenic on the surface of these binary mixed oxides.

The specific objectives fulfilled in order to reach this aim were as follows:

i) To understand the geometry of arsenic on the surface of TiO_2/Fe_2O_3 binary mixed oxides

ii) To investigate the effect of pH on the molecular structure of arsenic adsorbed on the surface of TiO_2/Fe_2O_3 binary mixed oxides

iii) To examine whether the binding mode of arsenic with the three synthesized TiO_2/Fe_2O_3 binary mixed oxides is retained or varies

iv) To compare the molecular structure of arsenic on TiO_2/Fe_2O_3 binary mixed oxides at different adsorption times

4.3 Results and discussion

4.3.1 Confirmation of arsenic oxidation states on the surface of TiO_2/Fe_2O_3 binary mixed oxides using XANES analysis

In this experiment, the XANES spectra of standard As_2O_3 (arsenite) and $HNa_2AsO_4.7H_2O$ (arsenate) were recorded as standard for the arsenic K-edge (E^0) positions of both oxidation states. The standard values of E^0 can be used to indicate the initial arsenic oxidation state before studying the binding modes of arsenic onto the binary mixed oxides. The XANES spectra from this experiment are presented in Figure 4.4.

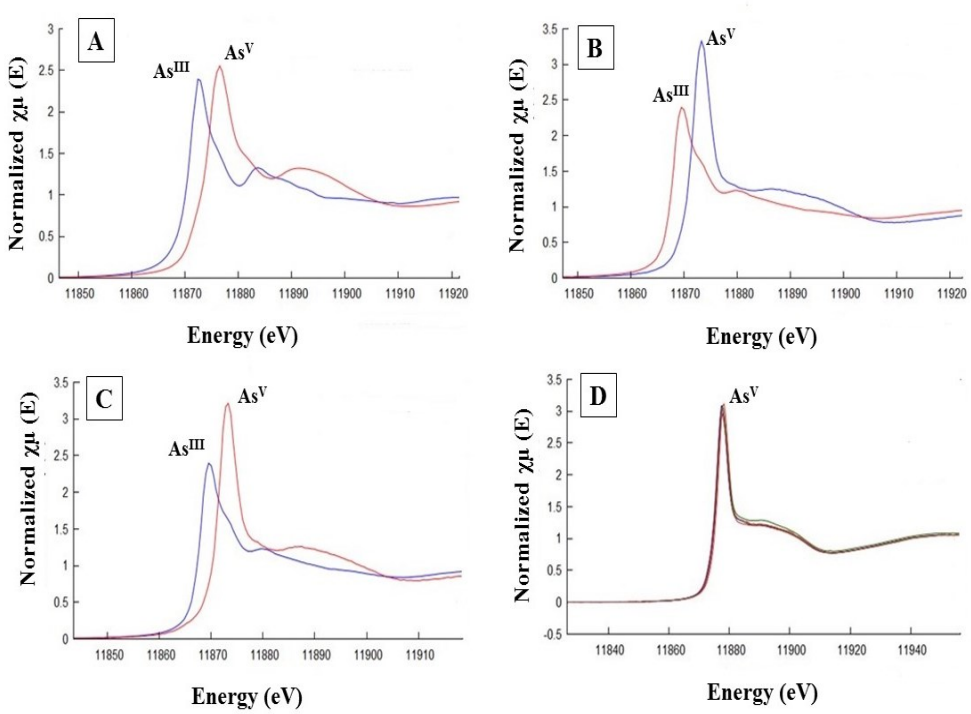


Figure 4.4 *Arsenic K-edge X-ray Absorption Near Edge Structure (XANES) spectra, (A) standard As^{III}, As_2O_3 and As^{V}, $HNa_2AsO_4.7H_2O$, arsenic adsorbed binary mixed oxides at (B) pH 5 and (C) pH 9, (D) Overlay of XANES spectra of As^{V} adsorbed CP-, MB-, SG- TiO_2/Fe_2O_3 binary mixed oxides at pH 7 for 2 and 24 h (spectra of six samples were found in the same position)*

The binding modes of As^{III} and As^{V} onto TiO_2/Fe_2O_3 binary mixed oxides was studied by XANES after the material had been exposed to arsenic for 24 h under nitrogen atmosphere to protect As^{III} pre-oxidation. XANES spectra of arsenic K-edge were recorded and compared with standard As_2O_3 (arsenite) and $HNa_2AsO_4.7H_2O$ (arsenate). The As^{III} and As^{V} K-edge spectra in Figure 4.4 (A) show ^0E of As^{III} at 11871.4 and As^{V} at 11874.5 eV which can be used to determine the original oxidation states of arsenic adsorbed onto TiO_2/Fe_2O_3 binary mixed oxides prior to the EXAFS analysis. The XANES spectra (1st scan) of arsenic bound to the surface of TiO_2/Fe_2O_3 binary mixed oxides at pH 5 and 9 are shown in Figure 4.4 (B) and 4.4 (C), respectively and the K-edge positions of As^{III} at E^0 = 11870.1 eV and As^{V} at E^0 = 11873.7 eV.

The XANES spectra in Figure 4.4 (B)-4.4 (D) indicated that As^{III} and As^{V} adsorbed to TiO_2/Fe_2O_3 binary mixed oxides retained their original oxidation states. Furthermore, XANES spectra of As^{V} adsorbed TiO_2/Fe_2O_3 binary mixed oxides at 2 and 24 h in Figure 4.4 (D) confirmed that there is no change in the oxidation state after 24 h under these conditions.

4.3.2 EXAFS analysis of As^{III} adsorbed TiO_2/Fe_2O_3 binary mixed oxides

In this section, extended X-ray absorption fine structure (EXAFS) spectra of As^{III} adsorbed on TiO_2/Fe_2O_3 binary mixed oxides were studied to describe the structure and surface complexation of As^{III} onto the binary mixed oxides. The EXAFS results for As^{III} adsorbed onto CP and MB are illustrated in Figure 4.5 EXAFS spectra were simulated using combination models including arsenic-scorodrite, arsenic-fetiasite, arsenic-hematite and arsenic-anatase crystal structural models. The results of the theoretical EXAFS calculation (dotted lines) compared with experimental data (solid lines) are also presented in Figure 4.5 and K-edge EXAFS fitted parameters are given in Table 4.2.

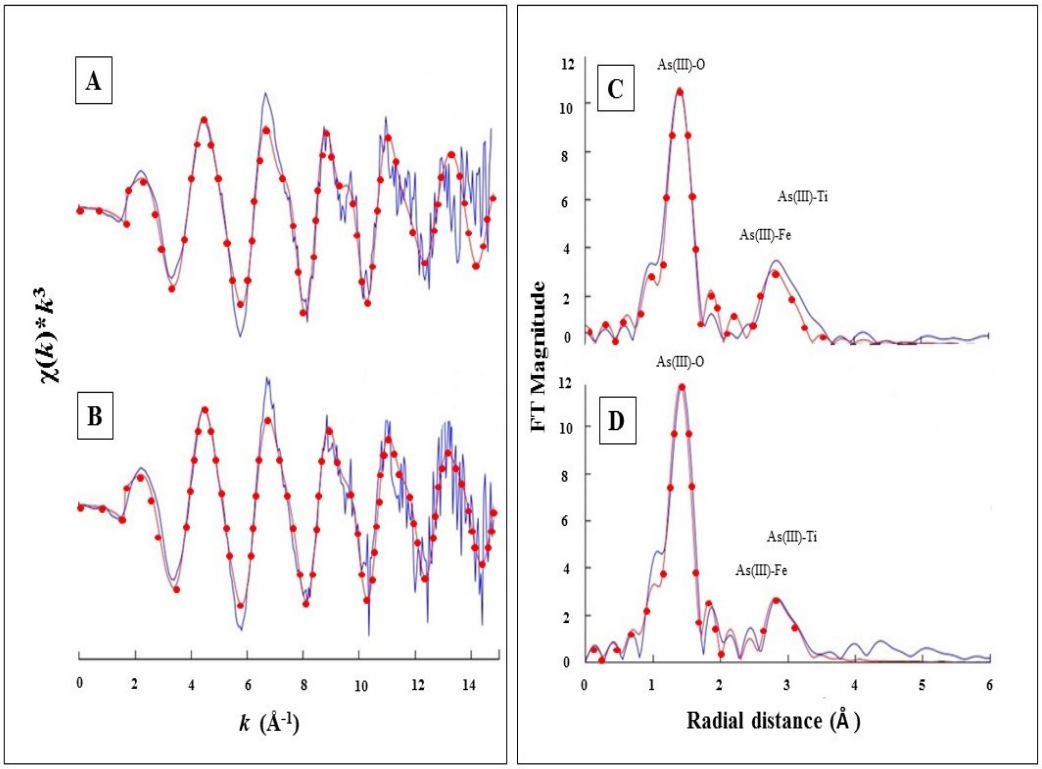


Figure 4.5 *Arsenic K-edge EXAFS spectra for As^{III} adsorbed onto TiO_2/Fe_2O_3 binary mixed oxides (CP and MB), K-edge EXAFS function (solid lines) and theoretical EXAFS calculation (dotted lines) for (A) As^{III}-CP and (B) As^{III}-MB. Radial structure Fourier transformed EXAFS spectra (solid lines) and theoretical EXAFS calculation (dotted lines) for (C) As^{III}-CP and (D) As^{III}-MB.*

Figure 4.5(A) and 4.5(B) shows fits in K-edge EXAFS function and Figure 4.5(C) and 4.5(D) show fits in radial function. Both sets of experimental results fitted very well with the theoretical EXAFS calculations. EXAFS spectra of As^{III} adsorbed binary mixed oxides in Figure 4.5(B) and 4.5(C) presents two dominant peaks called the first and second shells. The first peak corresponds to As^{III}-O shell which presents As^{III} coordinated with three oxygen atoms (CN= 3.0) at As^{III}-O interatomic distance 1.78±0.03 Å, characteristic of arsenite trigonal pyramidal molecule [6, 9, 10]. The interatomic distances in this study (see Table 4.2) were consistent with previously reported EXAFS studies of As^{III} adsorption on Fe or Ti metal oxides (Table 4.1).

Table 4.2 *Arsenic K-edge EXAFS fitting parameters for As^{III} and As^{V} adsorbed on TiO_2/Fe_2O_3 binary mixed oxides*

Sample	pH	Interatomic shell	R(Å)	CN	σ^2 (Å^2)	ΔE_0 (eV)	Adsorption time (h)
As^{III}-CP	5	As^{III}-O	1.78±0.03	3.0	0.0001	9.32	24
		As^{III}-Fe_1	2.93±0.03	0.5	0.0001	-	
		As^{III}-Fe_2	3.31±0.05	0.5	0.0009	-	
		As^{III}-Ti	3.35±0.31	1.5	0.0009	-	
As^{III}-MB	5	As^{III}-O	1.78±0.02	3.0	0.0006	9.62	
		As^{III}-Fe_1	2.94±0.02	0.5	0.0057	-	24
		As^{III}-Fe_2	3.31±0.07	0.5	0.0057	-	
		As^{III}-Ti	3.35±0.30	1.5	0.0083	-	
As^{III}-CP	9	As^{III}-O	1.78±0.02	3.0	0.0020	10.61	
		As^{III}-Fe_1	2.97±0.00	0.5	0.0030	-	24
		As^{III}-Fe_2	3.32±0.03	0.5	0.0030	-	
		As^{III}-Ti	3.35±0.00	1.5	0.0030	-	
As^{III}-MB	9	As^{III}-O	1.77±0.01	3.0	0.0015	9.90	
		As^{III}-Fe_1	2.99±0.03	0.5	0.0081	-	24
		As^{III}-Fe_2	3.16±0.32	0.5	0.0081	-	
		As^{III}-Ti	3.33±0.29	1.5	0.0038	-	
As^{V}-CP	5	As^{V}-O	1.69±0.07	3.7	0.0003	6.16	
		As^{V}-Fe_1	2.89±0.08	0.5	0.0035	-	24
		As^{V}-Fe_2	3.30±0.41	0.5	0.0035	-	
		As^{V}-Ti	3.43±0.39	1.5	0.0096	-	
As^{V}-MB	5	As^{V}-O	1.69±0.06	3.7	0.0003	7.71	
		As^{V}-Fe_1	2.76±0.20	0.5	0.0030	-	24
		As^{V}-Fe_2	3.15±0.06	0.5	0.0030	-	
		As^{V}-Ti	3.25±0.05	1.5	0.0084	-	
As^{V}-CP	7	As^{V}-O	1.69±0.07	3.7	0.0015	6.30	
		As^{V}-Fe_1	2.77±0.20	0.5	0.0019	-	24
		As^{V}-Fe_2	3.33±0.03	0.5	0.0019	-	
		As^{V}-Ti	3.00±0.08	1.5	0.0046	-	
As^{V}-MB	7	As^{V}-O	1.69±0.07	3.7	0.0017	6.06	
		As^{V}-Fe_1	2.79±0.18	0.5	0.0016	-	24
		As^{V}-Fe_2	3.34±0.01	0.5	0.0016	-	
		As^{V}-Ti	3.00±0.07	1.5	0.0050	-	
As^{V}-CP	9	As^{V}-O	1.69±0.06	3.7	0.0007	7.21	
		As^{V}-Fe_1	2.76±0.21	0.5	0.0009	-	24
		As^{V}-Fe_2	3.11±0.25	0.5	0.0009	-	
		As^{V}-Ti	3.00±0.08	1.5	0.0013	-	

(R(Å) = Interatomic distances, CN = Coordination number, σ^2 (Å^2) = Debye Waller Factor, ΔE_0 (eV) = Threshold E^0 shift in electron volt use for all shell)

Table 4.2 (Continued) *Arsenic K-edge EXAFS fitting parameters for As^{III} and As^{V} adsorbed on TiO_2/Fe_2O_3 binary mixed oxides*

Sample	pH	Interatomic shell	R(Å)	CN	σ^2 (Å^2)	ΔE_0 (eV)	Adsorption time (h)
As^V-MB	9	As^V-O	1.69±0.07	3.7	0.0001	7.27	
		As^V-Fe_1	2.76±0.20	0.5	0.0024	-	24
		As^V-Fe_2	3.29±0.06	0.5	0.0024	-	
		As^V-Ti	3.00±0.06	1.5	0.0046	-	
As^V-SG	7	As^V-O	1.69±0.07	3.7	0.0012	6.29	
		As^V-Fe_1	2.77±0.20	0.5	0.0027	-	24
		As^V-Fe_2	3.28±0.09	0.5	0.0027	-	
		As^V-Ti	3.00±0.08	1.5	0.0053	-	
As^V-CP	7	As^V-O	1.69±0.07	3.7	0.0016	6.39	2
		As^V-Fe_1	2.84±0.13	0.5	0.0018	-	
		As^V-Fe_2	3.33±0.04	0.5	0.0018	-	
		As^V-Ti	3.00±0.00	1.5	0.0130	-	
As^V-MB	7	As^V-O	1.69±0.07	3.7	0.0010	6.67	2
		As^V-Fe_1	2.77±0.20	0.5	0.0019	-	
		As^V-Fe_2	3.33±0.04	0.5	0.0019	-	
		As^V-Ti	3.00±0.08	1.5	0.0048	-	
As^V-SG	7	As^V-O	1.69±0.07	3.7	0.0012	6.29	2
		As^V-Fe_1	2.77±0.20	0.5	0.0027	-	
		As^V-Fe_2	3.28±0.09	0.5	0.0027	-	
		As^V-Ti	3.00±0.08	1.5	0.0053	-	

(R(Å) = Interatomic distances, CN = Coordination number, σ^2 (Å^2) = Debye Waller Factor, ΔE_0 (eV) = Threshold E^0 shift in electron volt use for all shell)

The second shell in the Fourier transformed plots shown in Figure 4.5(C) and 4.5(D) and the data summarized in Table 4.2 can be used to explain the As^{III} interaction with Fe and Ti of the binary mixed oxides. The interatomic distances at 2.94±0.02 Å and 3.31±0.07 Å can be assigned to As^{III}-Fe_1 and As^{III}-Fe_2. The coordination number (CN) calculated from EXAFS modeling found at 0.5 for As^{III} binding Fe_1 (As^{III}-Fe_1) and As^{III} binding Fe_2 (As^{III}-Fe_2) and the EXAFS fitting results are shown in Table 4.2.

The results of EXAFS fitting gives interatomic distances of As^{III}-Ti at 3.35±0.30 Å and the coordination number (CN) of As^{III} binding Ti is 1.5. The interatomic

distances and CN were calculated from EXAFS modelling (the EXAFS fitting parameters are shown in Table 4.2).

The EXAFS fitting results in this work were also compared with the data previously reported (Table 4.1). The interatomic distances of As^{III}-Fe_1, As^{III}-Fe_2 and As^{III}-Ti are all in agreement with previous studies. All Fourier transformed EXAFS spectra in Figure 4.5(C) and 4.5(D) of As^{III} on TiO_2/Fe_2O_3 binary mixed oxides found the second neighbor shell to be weaker and smaller when compared with the first shell supporting the occurrence of arsenic surface complexes instead of precipitations. The results found in this work are in agreement with the explanation of As^{III} adsorption on ferrihydrite and hematite reported by Ona-Nguema et al.,[9].

4.3.3 EXAFS analysis of As^V adsorbed on TiO_2/Fe_2O_3 binary mixed oxides

The molecular structures of As^V onto the surface of TiO_2/Fe_2O_3 binary mixed oxides including CP, MB and SG were investigated. Arsenic K-edge EXAFS data (K-function) are displayed in Figure 4.6(A), 4.6(B) and 4.6(C) and Fourier transformation of EXAFS spectra in radial structure functions (RSF) are presented in Figure 4.6(D), 4.6(E) and 4.6(F). The EXAFS spectra of As^V adsorbed onto TiO_2/Fe_2O_3 binary mixed oxides at pH 5, 7 and 9 (Figure 4.6) were fitted using the crystal structure models. The As-O, As-Fe and As-Ti distances of arsenic adsorbed binary mixed oxides were simulated from the crystal structures of scorodite, arsenic-fetiasite and arsenic-anatase, respectively. The fits of the theoretical EXAFS calculation (dotted lines) and the experimental data (solid lines) are also presented. The K-edge and Fourier transformed EXAFS spectra of all samples in Figure 4.6 show very good fits and present two significant peaks in the first and second shells.

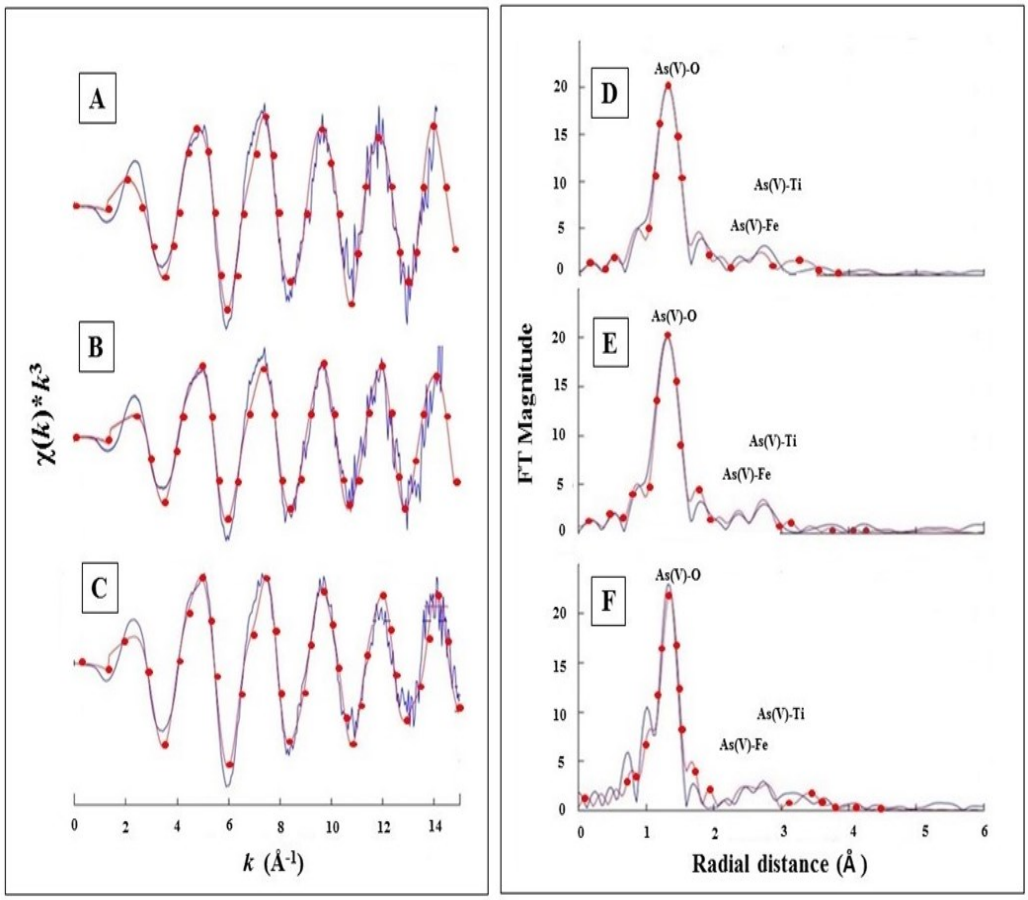


Figure 4.6 *Arsenic K-edge EXAFS spectra for As^V adsorbed TiO_2/Fe_2O_3 binary mixed oxides (CP MB and SG), K-edge EXAFS function (solid lines) and theoretical EXAFS calculation (dotted lines) for (A) As^V-CP, (B) As^V-MB, and (C) As^V-SG. Radial structure Fourier transformed EXAFS spectra (solid lines) and theoretical EXAFS calculation (dotted lines) for (D) As^V-CP, (E) As^V-MB, and (F) As^V-SG*

The first dominant peaks in the Fourier transformed plots shown in Figure 4.6(D), 4.6(E) and 4.6(F) are As^V binding with oxygen atoms of arsenate tetrahedral molecules (see Table 4.2). The interatomic distance of As^V-O found at 1.69±0.06 Å. The coordination number (CN) from EXAFS fitting model of As^V binding with oxygen atoms found at 3.7. These results are in the same range to those values previously reported for As^V adsorbed onto Fe or Ti oxides.

The second peaks in the Fourier transformed plots in Figure 4.6(D), 4.6(E) and 4.6(F) are As^V binding with Fe and Ti atoms on the surface of TiO_2/Fe_2O_3 binary mixed oxides. The interatomic distances of As^V-Fe_1, As^V-Fe_2 and As^V-Ti are 2.76±0.20, 3.29±0.06 and 3.25±0.06 Å, respectively. The coordination numbers (CN) from EXAFS fitting model of As^V binding with Fe_1, Fe_2 and Ti are found at 0.5, 0.5 and 1.5, respectively.

The Fourier transformed EXAFS spectra of As^V adsorbed TiO_2/Fe_2O_3 binary mixed oxides in Figure 4.6(D), 4.6(E) and 4.6(F) also show the lower magnitude in the second peak which suggests that As^V can form adsorption complexes onto the surface of the binary mixed oxides.

4.3.4 Geometry of arsenic TiO_2/Fe_2O_3 binary mixed oxide surface complexes.

The As-Fe_1, As-Fe_2 and As-Ti (for the three materials, i.e. CP, MB, and SG) interatomic distances determined by EXAFS (Table 4.2) can be used to gain insight into the surface complexes formed between As and the binary mixed oxides. As discussed above, we did not find significant differences between the three binary mixed oxide materials. Therefore, the discussion of arsenic-binary mixed oxide surface complexes in this section will focus only on MB as a representative example of the arsenic binding mode to Ti/Fe binary mixed oxides.

There are several possible binding modes between As^{III}/As^V and surface of TiO_2/Fe_2O_3 binary mixed oxides which are illustrated in Figure 4.7. The main binding modes found from this study are bidentate mononuclear edge sharing (^2E) complexes (As-Fe_1) and bidentate binuclear corner sharing (^2C) complexes (As^V-Fe_2 and As-Ti).

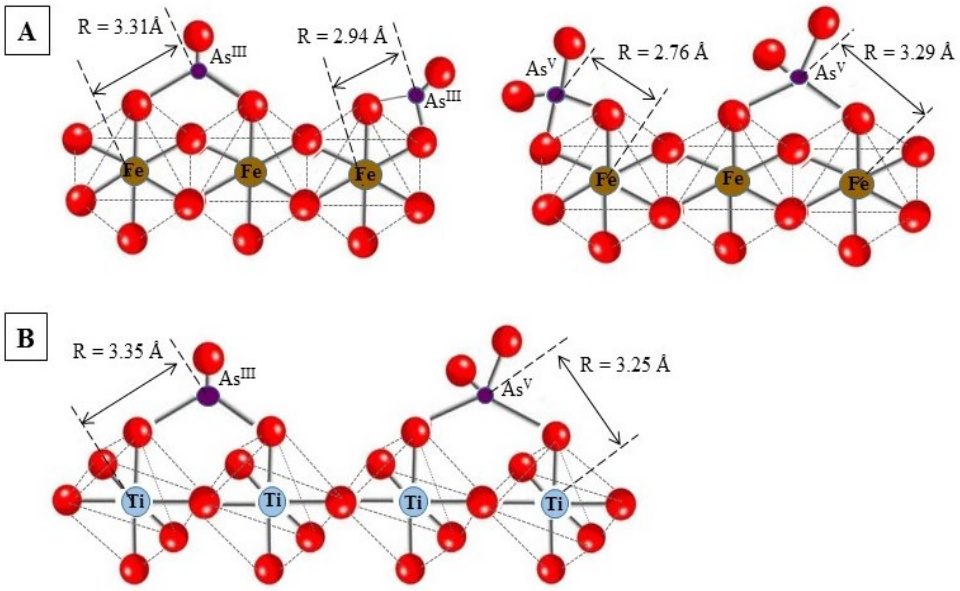


Figure 4.7 *The possible binding modes of As^{III} and As^{V} onto the surface of TiO_2/Fe_2O_3 binary mixed oxides indicated from our experimental results using EXAFS analysis, the interatomic distances of (A) As^{III}-Fe and As^{V}-Fe, (B) As^{III}-Ti, and As^{V}-Ti onto binary mixed oxides surfaces.*

The EXAFS spectra of As^{III} adsorption on the binary mixed oxides found As^{III}-Fe_1 interatomic distance around 2.94±0.20 Å. This short distance is consistent with As^{III} forming a bidentate mononuclear edge sharing (^{2}E) complex with the octahedral Fe_1 on the surface of binary mixed oxides. The interatomic distance of As^{III}-Fe_2 at 3.31±0.14 Å can be ascribed to bidentate binuclear corner sharing (^{2}C) complex. The EXAFS also show that As^{III}-Ti interatomic distance 3.35±0.30 Å resulted from As^{III} form bidentate binuclear corner sharing (^{2}C) complex with octahedral Ti on the surface of the binary mixed oxides as shown in Figure 4.7(A). The interatomic distances of As^{III}-Fe_1, As^{III}-Fe_2 and As^{III}-Ti distances and corresponding geometries found in this study agree with previous works by Ona-Nguema et al., [9] and Pena et al., [10] that report As^{III}-Fe_1, As^{III}-Fe_2 distances

on hematite at 2.89±0.03 Å and 3.36±0.03Å [9], respectively and As^{III}-Ti distance on anatase at 3.35 Å [10].

EXAFS analysis of As^{V} adsorption on TiO_2/Fe_2O_3 binary mixed oxides are presented in Table 4.2. The interatomic distances of As^{V}-Fe_1, As^{V}-Fe_2 and As^{V}-Ti are found at 2.76±0.20 Å, 3.29±0.06 Å and 3.25±0.06 Å, respectively. The geometry of As^{V} adsorbed TiO_2/Fe_2O_3 binary mixed oxide surface complexes found in the same types of As^{III} surface complexes on the TiO_2/Fe_2O_3 binary mixed oxides. As^{V}-Fe_1 short distance at 2.76±0.20 Å describes that As^{V} form bidentate mononuclear edge sharing (^{2}E) complex and As^{V}-Fe_2 interatomic distance around 3.29±0.06 Å represent As^{V} form bidentate binuclear corner sharing (^{2}C) complex. Moreover, at As^{V}-Ti around 3.25±0.06 Å resulted from bidentate binuclear corner sharing (^{2}C) complex of As^{V} on the surface of the binary mixed oxides as shown in Figure 4.7(B). The interatomic distances of As^{V}-Fe_1, As^{V}-Fe_2 and As^{V}-Ti and corresponding geometries found in this work agree with previous studies by Fendorf et al., [6] and Pena et al., [10]. They found As^{V}-Fe_1, As^{V}-Fe_2 on Fe oxides at 2.85Å and 3.24 Å [6], respectively and As^{V}-Ti distance on anatase at 3.0 Å [10].

EXAFS analysis of As^{III} and As^{V} adsorption on TiO_2/Fe_2O_3 binary mixed oxides show that the interatomic distances of As^{V} with iron oxide and titanium dioxide are shorter than those display by As^{III}. On the other hand, the binding modes of both As^{III} and As^{V} on the binary mixed oxides are, including a bidentate mononuclear edge sharing (^{2}E) complex and a bidentate binuclear corner sharing (^{2}C) complex.

4.3.5 Effect of pH on geometry of arsenic adsorbed TiO_2/Fe_2O_3 binary mixed oxide surface complexes

In this experiment, the adsorption of arsenic on CP, MB and SG at pH 5, 7 and 9 was carried out and the surface complexes of arsenic on these binary mixed

oxides under these conditions investigated. The second neighbor shell of Fourier transformed EXAFS spectra is particularly relevant to identify the surface complexation of arsenic with Fe and Ti metal oxides.

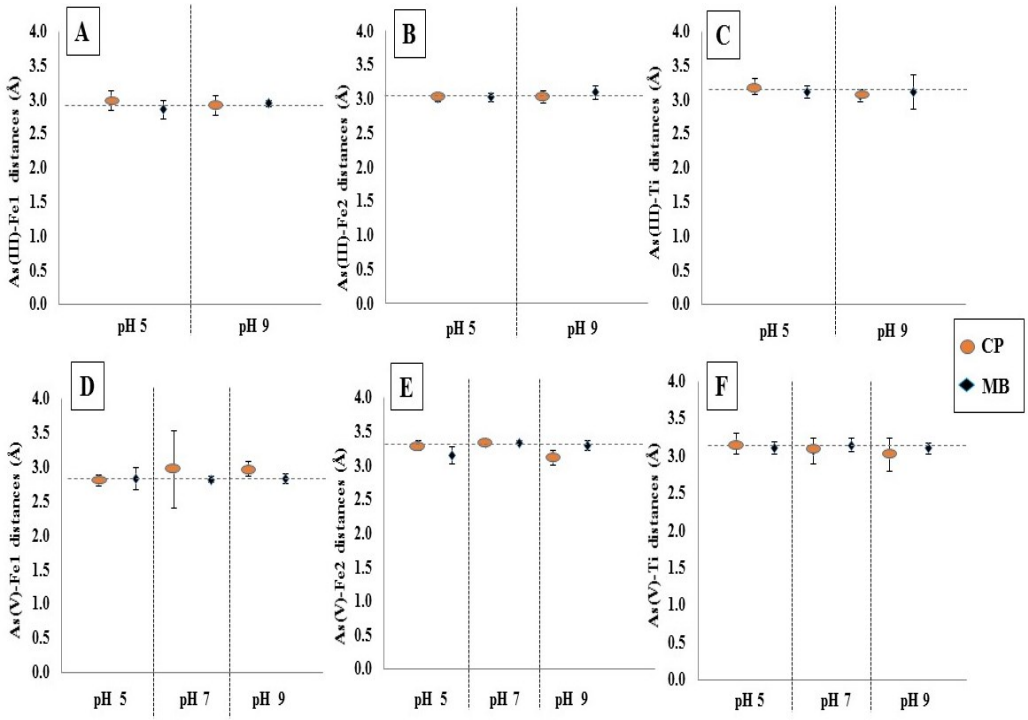


Figure 4.8 *Interatomic distances from EXAFS fitting results of arsenic adsorption on CP and MB at pH 5, 7 or 9. (A) As^{III}-Fe_1 distances, (B) As^{III}-Fe_2 distances, (C) As^{III}-Ti distances, (D) As^{V}-Fe_1 distances, (E) As^{V}-Fe_2 distances and (F) As^{V}-Ti distances*

The interatomic distances of As-Fe_1, As-Fe_2 and As-Ti of different binary mixed oxide types and pH values are plotted and presented in Figure 4.8(A) - 4.8(F). The interatomic distances of As^{III}-Fe_1, As^{III}-Fe_2 and As^{III}-Ti of CP and MB at pH 5 and 9 in Figure 4.8(A) to 4.8(C) were found in the same range and no significant differences were observed at both pH values. Therefore, the binding mode of As^{III} on the surface of CP and MB at pH 5 and 9, is namely bidentate mononuclear edge sharing (^{2}E) surface complexes (at As^{III}-Fe_1 distance) and bidentate

binuclear corner sharing (^{2}C) surface complex (at As^{III}-Fe_2 and As^{III}-Ti distances).

The interatomic distances of the second neighbor shell of As^V adsorption on CP, MB and SG at pH 5, 7 and 9 are shown in Figures 4.8(D) - 4.8(F) (data shown in Table 4.2). The interatomic distances of As^V-Fe_1, As^V-Fe_2 and As^V-Ti of CP, MB and SG at pH 5, 7 and 9, are in the same range for all pH values studied. These are consistent with a bidentate mononuclear edge sharing (^{2}E) surface complex (for the As^V-Fe_1 distance) and bidentate binuclear corner sharing (^{2}C) surface complex (for the As^V-Fe_2 and As^V-Ti distances). The similarity of arsenic binding modes at pH 5, 7 and 9 indicated that the adsorption pH in this study have no effect on the geometry of arsenic adsorption onto the surface of binary mixed oxides.

4.3.6 Effect of adsorption time on geometry of arsenic adsorbed on TiO_2/Fe_2O_3 binary mixed oxide surface complexes

The adsorption kinetic study in previous work found two different kinetic rates of arsenic on TiO_2/Fe_2O_3 binary mixed oxides [2] was hypothesized that this kinetics could be due to different binding modes of arsenic onto the binary mixed oxide surface at different adsorption times. Therefore, the binding modes at 2 and 24 h were analyzed by using EXAFS analysis.

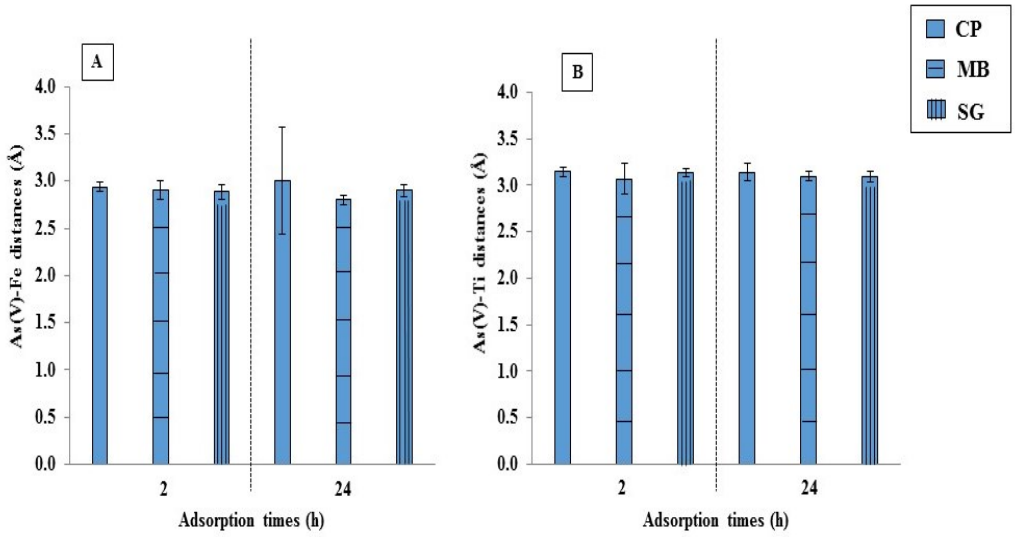


Figure 4.9 *Interatomic distances from EXAFS fitting results of arsenic adsorption on CP, MB or SG for 2 or 24 h at pH 7. (A) As^{V}-Fe_1 distances and (B) As^{V}-Ti distances*

The interatomic distances of As^{V}-Fe_1, As^{V}-Fe_2 and As^{V}-Ti for CP, MB and SG at 2 and 24 h are no significantly different (see Figure 4.9 and Table 4.2). Therefore, it can be concluded that the surface complexes of As^{V} adsorbed onto TiO_2/Fe_2O_3 binary mixed oxides at both adsorption times are the same, namely bidentate mononuclear edge sharing (^{2}E) complex (at As^{V}-Fe_1 distance) and bidentate binuclear corner sharing (^{2}C) complexes (at As^{V}-Fe_2 and As^{V}-Ti distances).

4.3.7 Discussion of binding modes of arsenic oxides on binary mixed oxides

4.3.7.1 Molecular structure of arsenic on TiO_2/Fe_2O_3 binary mixed oxides

The binding mode of arsenic on the surface of TiO_2/Fe_2O_3 binary mixed oxides including CP, MB and SG were investigated. The geometries of As^{III} binding onto all types of TiO_2/Fe_2O_3 binary mixed oxides were found in similar surface complexes. As^{III}-O distances between 1.77±0.03 to 1.78±0.03 Å indicate As^{III} bonding with oxygen atom in arsenite molecules [6, 9, 10]. The interatomic distances for As^{III}-Fe_1 between 2.93±0.03 and 2.99±0.03 Å are consistent with a bidentate mononuclear edge sharing (^{2}E) complex [5, 6, 9]. This suggests that arsenite binds in a pyramidal geometry on the iron oxide octahedral molecule on the surface of binary mixed oxides. For the As^{III}-Fe_2 shell, the interatomic distances around 3.16±0.32 to 3.32±0.03 Å indicate that the arsenite binds in a pyramidal geometry forming a bidentate binuclear corner sharing (^{2}C) complex with the iron oxide octahedral molecule on the binary mixed oxide surface. The bidentate binuclear corner sharing (^{2}C) complex also represents the geometries of arsenite adsorption on octahedral titanium oxide present on the surface of binary mixed oxides which can be indicated by As^{III}-Ti interatomic distances between 3.33±0.29 to 3.35±0.31 Å.

Furthermore, the interatomic distances of As^{V}-O around 1.69±0.07 Å are consistent with a tetrahedral geometry for the As^{V} centre. The investigation of As^{V}-binary mixed oxide interatomic distances found As^{V}-Fe_1, As^{V}-Fe_2 and As^{V}-Ti at around 2.76±0.20 to 2.89±0.08 Å, 3.11±0.25 to 3.34±0.01 Å, and 3.00±0.08 to 3.43±0.39 Å, respectively.

The interatomic distances of As^{V}-Fe_1 between 2.76±0.02 to 2.89±0.08 Å can be used to indicate that As^{V} form bidentate mononuclear edge sharing (^{2}E) complex and As^{V}-Fe_2 distances between 3.11±0.02 to 3.34±0.01 Å can be used to explain

that As^V form bidentate binuclear corner sharing (^2C) complex onto the binary mixed oxide surfaces. Moreover, the interatomic distances between 3.00±0.08 to 3.43±0.39 Å can be assigned to As^V binding with Ti onto the surface of binary mixed oxides. The binding modes of arsenic onto the binary mixed oxides found in this research (see Table 4.2) are in agreement with previous reports in the literature [5, 6] (see Table 4.1).

4.3.7.2 Comparison of arsenic molecular structure adsorption on TiO_2/Fe_2O_3 binary mixed oxides at different pH values

As discussed above, our studies show that at the three pH values studied, there is no difference in the As^{III} binding mode to the three types of TiO_2/Fe_2O_3 binary mixed oxides under study (i.e. for As^{III}-Fe_1 shell, As^{III}-Fe_2 and As^{III}-Ti shells). This is likely due to the fact that As^{III} is electrostatically neutral in aqueous solution at pH values below 9.

On the other hand, As^V is naturally present as different oxyanions at different pH values; this can have an important effect on its adsorption onto TiO_2/Fe_2O_3 binary mixed oxides. It has been previously shown that the adsorption capacities of As^V on TiO_2/Fe_2O_3 binary mixed oxides highest at pH 7. Therefore, in this research the molecular structure of As^V on the binary mixed oxides were investigated at pH 5, 7 and 9. Similar to our observations for As^{III}, the EXAFS analysis indicate there are no significant differences to the binding mode of As^V with the binary mixed oxides at these pH values. In the three cases, the data suggests a bidentate mononuclear edge sharing (^2E) complex for As^V-Fe_1 shell, and bidentate binuclear corner sharing (^2C) complex for As^V-Fe_2 and As^V-Ti shells.

4.3.7.3 Relationship between nature of binary mixed oxides and molecular structure of arsenic adsorption on TiO_2/Fe_2O_3 binary mixed oxides

The EXAFS results indicate that the geometry of arsenite pyramidal molecules with iron oxide octahedral molecule are bidentate mononuclear edge sharing (^{2}E) complex at the short distance of As^{III}-Fe_1 shell and bidentate binuclear corner sharing (^{2}C) complex. The similar molecule structure of As^{III} on CP, MB and SG surfaces were observed in this research.

Furthermore, the molecular structure of As^V on the surface of CP, MB and SG found no significant differences presenting in the form of bidentate mononuclear edge sharing (^{2}E) complex for As^V-Fe_1 shell and bidentate binuclear corner sharing (^{2}C) complex for As^V-Fe_2 and As^V-Ti shells. All synthetic methods used in this work can be used to provide TiO_2/Fe_2O_3 binary mixed oxides which can form the same molecular structure of arsenic on their surfaces.

4.3.7.4 Comparison of kinetic adsorption and molecular structure of arsenic on TiO_2/Fe_2O_3 binary mixed oxides

The adsorption kinetics of As^V on TiO_2/Fe_2O_3 binary mixed oxides was previously found to be faster at the initial stages of the adsorption process (first 2 h) and slower after 2 h until equilibrium point at 24 h [2]. From EXAFS analysis, As^V adsorption on CP, MB, and SG at 2 and 24 h found similar molecular structure of As^V on these binary mixed oxides surfaces namely bidentate mononuclear edge sharing (^{2}E) complex for As^{III}-Fe_1 shell and bidentate binuclear corner sharing (^{2}C) complex for As^V-Fe_2 and As^V-Ti shells on the surface of the binary mixed oxides. Thus, the adsorption times do not seem to have and effect on the binding modes of arsenic onto the binary mixed oxides.

4.4 Conclusion

The EXAFS analysis provides very valuable insights to elucidate the binding mode of As^{III} and As^{V} adsorbed onto the surface of TiO_2/Fe_2O_3 binary mixed oxides. The following key conclusions have been reached:

i) The adsorption of arsenic on TiO_2/Fe_2O_3 binary mixed oxides occurs by the formation of arsenic-binary mixed oxide surface complexes resulting from bidentate mononuclear corner sharing (^{2}E) complexes and bidentate binuclear corner sharing (^{2}C) complexes. The evidences from EXAFS analysis show arsenic molecules can form complexes with iron oxides and titanium dioxide molecules on the surface of the binary mixed oxides.

ii) The binding modes of arsenic on the surface of TiO_2/Fe_2O_3 binary mixed oxides at pH 5, 7 and 9 are the same, namely bidentate mononuclear edge sharing (^{2}E) complex and bidentate binuclear corner sharing (^{2}C) complex.

iii) The binding mode of arsenic to the surface of the Ti/Fe-binary mixed oxides, is not dependent on the method by which the bicomposites were prepared. For the three different TiO_2/Fe_2O_3 binary mixed oxides (i.e. CP, MB and SG) the binding mode of the arsenic onto the binary mixed oxide surfaces includes bidentate mononuclear edge sharing (^{2}E) complex and bidentate binuclear corner sharing (^{2}C) complex.

iv) The adsorption times (at 2 and 24 h) do not have an effect on the molecular structure of the adsorbed arsenic. The evidences in this study present the similarity of arsenic surface complexes on the binary mixed oxides. Arsenic molecules adsorb on the surface of TiO_2/Fe_2O_3 binary mixed oxides by forming bidentate mononuclear edge sharing (^{2}E) complex and bidentate binuclear corner sharing (^{2}C) complex on the binary mixed oxide surfaces at both time intervals.

References

(1) Gupta, K.; Ghosh, U. C. *J. Hazard. Mater.* **2009**, *161*, 884-892.

(2) D'Arcy, M.; Weiss, D.; Bluck, M.; Vilar, R. *J. Colloid Interface Sci.* **2011**, *364*, 205-212.

(3) Zhang, F. S.; Itoh, H. *Chemosphere*. **2006**, *65*, 125-131

(4) Zhou, W.; Fu, H.; Tian, C.; Qu, Y.; Lu, P.; Sun, C. C. *J. Phys. Chem. C*. **2008**, *112*, 19584-19589.

(5) Sherman, D. M.; Randall, S. R. *Geochim. Cosmochim. Acta*. **2003**, *67*, 4223-4230.

(6) Fendorf, S.; Eick, M. J.; Grossl, P.; Sparks, D. L. *Environ. Sci. Technol.* **1997**, *31(2)*, 315-320.

(7) Manning, B. A.; Fendorf, S. E.; Goldberg, S. *Environ. Sci. Technol.* **1998**, *32*, 2383-2388.

(8) Manning, B. A.; Hunt, M. L.; Amrhein, C.; Yarmoff, J. A. *Environ. Sci. Technol.* **2002**, *36*, 5455-5461.

(9) Ona-Nguema, G.; Morin, G.; Juillot, F.; Calas, G.; Brown, G. E. *Environ. Sci. Technol.* **2005**, *39*, 9147-9155.

(10) Pena, M.; Meng, X.; Korfiatis, G. P.; Jing, C. *Environ. Sci. Technol.* **2006**, *40*, 1257-1262.

(11) Jegadeesan, G.; Al-Abed, S. R.; Sundaram, V.; Choi, H.; Scheckel, K. G.; Dionysiou, D. D. *Water Research*. **2010**, *44*, 965-973.

(12) Morin, G.; Ona-Nguema, G.; Wang, Y.; Menguy, N.; Juillot, F.; Proux, O.; Guyot, F.; Calas, G.; Brown, G. E. *Environ. Sci. Technol.* **2008**, *42*, 2361-2366.

(13) Guan, X. H.; Wang, J.; Chusuei, C. C. *J. Hazard. Mater.* **2008**, *156*, 178-185.

(14) Jönsson, J.; Sherman, D. M. *Chem. Geol.* **2008**, *255*, 173-181.

(15) Jing, C.; Cui, J.; Huang, Y.; Li, A. Appl. Mater.Interfaces. **2012**, *4*, 714-720.

(16) Waychunas, G. A.; Davis, J. A.; Fuller, C. C. *Geochimica et Cosmochimica Acta*. **1995**, *59(17)*, 3655-3661.

(17) Waychunas, G. A.; Fuller, C. C.; Rea, B. A.; Davis, J. A. *Geochim. Cosmochim. Acta*. **1996**, *60(10)*, 1765-1781.

(18) Foster, A. L.; Brown Jr, G. E.; Tingle, T. N.; Parks, G. A. *Am. Mineral.* **1998**, *83*, 553–568.

(19) Coker, V. S.; Gault, A. G.; Pearce, C. I.; Van Der Laan, G.; Telling, N. D.; Charnock, J. M.; Polya, D.

A.; Lloyd, J. R. *Environ. Sci. Technol.* **2006**, *40*, 7745-7750.

(20) Huggins, F. E.; Senior, C. L.; Chu, P.; Ladwig, K.; Huffman, G. P. *Environ. Sci. Technol.* **2007**, *41*, 3284-3289.

(21) Guo, X.; Du, Y.; Chen, F.; Park, H. S.; Xie, Y. *J. Colloid Interface Sci.* **2007**, *314*, 427-433.

(22) Auffan, M.; Rose, J.; Proux, O.; Borschneck, D.; Masion, A.; Chaurand, P.; Hazemann, J. L.; Chaneac, C.; Jolivet, J. P.; Wiesner, M. R.; Van Geen, A.; Bottero, J. Y. *Langmuir* **2008**, *24*, 3215-3222.

(23) Loring, J. S.; Sandstrom, M. H.; Noren, K; Person, P. *Chem. Eur. J.* **2009**, *15*, 5063-5072.

(24) Wang, Y.; Morin, G.; Ona-Nguema, G.; Juillot, F.; Guyot, F.; Calas, G.; Brown, G. E. *Environ. Sci. Technol.* **2010**, *44*, 109-115.

(25) Catalano, J. G.; Luo, Y.; Otemuyiwa, B. *Environ. Sci. Technol.* **2011**, *45*, 8826-8833.

(26) Guo, H.; Ren, Y.; Liu, Q.; Zhao, K.; Li, Y. *Environ. Sci. Technol.* **2013**, *47*, 1009-1016.

(27) Luo, T.; Tian, H.; Guo, Z.; Zhuang, G.; Jing, C. *Environ. Sci. Technol.* **2013**, 47, 10939-10946.

Chapter 5

Surface promoted photocatalytic oxidation of As^{III} to As^{V} using TiO_2/Fe_2O_3 binary mixed oxides

Most arsenic remediation processes based on adsorbing materials require the pre-oxidation of As^{III} to As^{V}. One approach that has been previously investigated to tackle this issue is the photo-oxidation of As^{III} to As^{V} prior to the adsorption process taking place. TiO_2/Fe_2O_3 binary mixed oxides are a type of material that has already been shown to achieve this by combining, the pre-oxidation and adsorption steps on their surfaces. However, the detailed mechanism of how this takes place is still not known. Thus, the work in this chapter describes photocatalytic oxidation mechanism of As^{III} on the surfaces of the three different TiO_2/Fe_2O_3 binary mixed oxides described in Chapter 3. The photocatalytic oxidation mechanisms of As^{III} to the less toxic As^{V} on the surface of TiO_2/Fe_2O_3 binary mixed oxides including CP, MB and SG under synchrotron beam or UV light irradiation were investigated. Valence band hole (h_{vb}^{+}), conduction band electron (e_{cb}^{-}), superoxide (O_2^{*-}) and hydroxyl radical ($^{*}OH$) can be generated on the solid surfaces of TiO_2/Fe_2O_3 binary mixed oxides activated by synchrotron or UV light. The photocatalytic oxidation kinetics on the solid surfaces were investigated; we confirm that the photo-oxidation of As^{III} to As^{V} take place on the surface of the binary mixed oxides under synchrotron beam irradiation, reaching photocatalytic oxidation equilibrium within 45 min. The oxidation rate constants were used to compare the photocatalytic properties of each types of TiO_2/Fe_2O_3 binary mixed oxides. Furthermore, two sets of experiments to observe the photocatalytic oxidation mechanisms of As^{III} to As^{V} in aqueous

solution systems were examined. For this, aqueous solutions of As^{III} were irradiated in the presence/absence of binary mixed oxides with synchrotron beam in a 'Perspective' photo-reactor. Changes in the oxidation state of As were monitored by using X-ray absorption near edge structure (XANES). With the synchrotron beam, XANES spectra at K-edge position of As^{III} shifted to K-edge position of As^{V}, indicating that a photocatalytic oxidation facilitated by the TiO_2/Fe_2O_3 binary mixed oxides has taken place. A second experiment was carried using the same reactor and binary mixed oxides but irradiating the aqueous solution of As^{III} with UV light. In this case, the decrease of As^{III} was determined using a voltammetric method (i.e. square wave anodic stripping voltammetry (SWASV)). The experimental results show As^{III} can photocatalytic oxidize to As^{V} in TiO_2/Fe_2O_3 binary mixed oxides suspension with UV irradiation.

5.1 Introduction

As has been already discussed in Chapter 1, As^{III} is more toxic and more mobile than As^{V} [1, 2]. Furthermore, it is more difficult to adsorbed onto solid (and hence remove from contaminated water) due to zero charge species of As^{III} at pH below 9. Thus, most remediation methods for As^{III} contaminated water need pre-oxidation of As^{III} to As^{V} before adsorption. Chemicals such as chloride, chloramine and ozone are often used as oxidants in contaminated water treatment. However, issues related to the generation of toxic byproducts from these oxidants such as trihalomethane, *N*-nitrosodimethylamine and bromate are of concern [3]. To overcome these problems, one approach is to facilitate the oxidation process of As^{III} to As^{V} by photocatalysis using metal oxides. Table 5.1 summarizes previously reported materials/processes used for the photo-oxidation of As^{III} to As^{V}.

TiO_2 is frequency used as photocatalyst in water treatment process and, as highlighted in Table 5.1, it has also been applied to study the photocatalytic oxidation of As^{III} to As^{V} [7, 8, 9]. The photocatalytic oxidation mechanism using TiO_2 has been explained as follows: when a photon interacts with the surface of TiO_2 a valence band hole (h_{vb}^+) and a conduction band electron (e_{cb}^-) are generated. h_{vb}^+ combines with hydroxide to produce hydroxyl radical ($^*OH$) and e_{cb}^- reacts with oxygen to create superoxide (O_2^{*-}). In turn, it has been proposed that $^*OH$ and O_2^{*-} are responsible for As^{III} photocatalytic oxidation to As^{V}. TiO_2 has a wide band gap energy at 3.2 eV and therefore UV light needs to be used to induce the photocatalytic activity of this material, which limits its applications. One approach to reduce this bandgap is to use a TiO_2/Fe_2O_3 binary mixed oxides which have a band-gap energy of 2.6 eV reducing the energy required to trigger the photocatalytic process (possibly into the visible range).

Table 5.1 *Summary of previously reported photocatalytic methods to oxidize arsenic(III)*

Materials	Methods	Study phase	Analysis	Ref.
Ferrihydrite	Surface oxidation	Solid	XANES	[4]
Goethite	Photo-induce oxidation	Solid suspended solution	XANES	[5]
Kaolinite clay	Photocatalytic oxidation	Solid	STXM	[6]
TiO_2	Photocatalytic oxidation	Solid suspended solution	ICP-MS	[7]
TiO_2	Photocatalytic oxidation	Solid suspended solution	IC	[8]
TiO_2	Photocatalytic oxidation	Solid suspended solution	FAAS	[9]
Fe/Ti co-pillared clay	Photocatalytic oxidation	Solid suspended solution	AFS	[10]
Mesoporous Fe-Ce bimetal oxides (MMTC)	Photocatalytic oxidation	Solid suspended solution	ICP-MS	[11]
MoO_x/TiO_2	Photocatalytic oxidation	Solid suspended solution	UV-vis spectroscopy	[12]
Slag-iron/TiO_2	Photocatalytic oxidation	Solid suspended solution	ICP-AES	[13]
TiO_2/MMT	Photocatalytic oxidation	Solid suspended solution	AFS	[14]
ɤ-Fe_2O_3-TiO_2 magnetic nanoparticle	Photocatalytic oxidation	Solid suspended solution	HG-AFS	[15]

Several groups have previously reported the photocatalytic properties of TiO_2 mixed with iron oxides. For example, Zhu and co-workers [16] first demonstrated the combination of Fe_2O_3 with TiO_2 reduces the band gap energy of TiO_2. This was followed by a report which demonstrated the use of mesoporous TiO_2/Fe_2O_3 bicomposites to effectively remove As^{III} by simultaneous photocatalytic

oxidation and adsorption; this study also found that superoxide radicals are important species for photocatalytic oxidation of As^{III} to As^{V} [17].

Liu and co-workers [18] have also reported the photocatalytic study of mixing Fe_2O_3 solution with TiO_2 and found the photocatalytic activities of mixing solution has higher than pure TiO_2 under visible and solar irradiation.

While these reports show that mixing Fe_2O_3 with TiO_2 can improve the photoctalytic properties of pure TiO_2, there is still a lack of detailed mechanistic understanding of the process by which. As^{III} is photocatalytically oxidised to As^{V}.

5.2 Aims and objectives

The aim of the work presented in this chapter was to investigate the photocatalytic oxidation of As^{III} using TiO_2/Fe_2O_3 binary mixed oxides. The specific objectives required to reach the aims were as follows:

i) To determine the photocatalytic oxidation rates of As^{III} bound to the surfaces of three different types of TiO_2/Fe_2O_3 binary mixed oxides and study the mechanism of this process.

ii) To study the photocatalytic oxidation mechanism of As^{III} to As^{V} using TiO_2/Fe_2O_3 binary mixed oxides in aqueous solutions by irradiation with synchrotron beam and UV light.

iii) To identify the best TiO_2/Fe_2O_3 binary mixed oxides for the photocatalytic oxidation of As^{III} to As^{V} and the concomitant scavenging of arsenic.

5.3 Results and discussion

5.3.1 XANES analysis of As^{III} and As^{V} standards

Before studying the oxidation of As^{III} to As^{V} with our binary mixed oxides, it was necessary to carry out measurements of some known arsenic samples adsorbed onto our binary mixed oxides. As described in Chapter 4 (section 4.3.1) we first recorded the XANES of As_2O_3 and $HNa_2AsO_4.7H_2O$ as standard to determine the K-edge (E^0) positions of both oxidation states (see Figure 5.1).

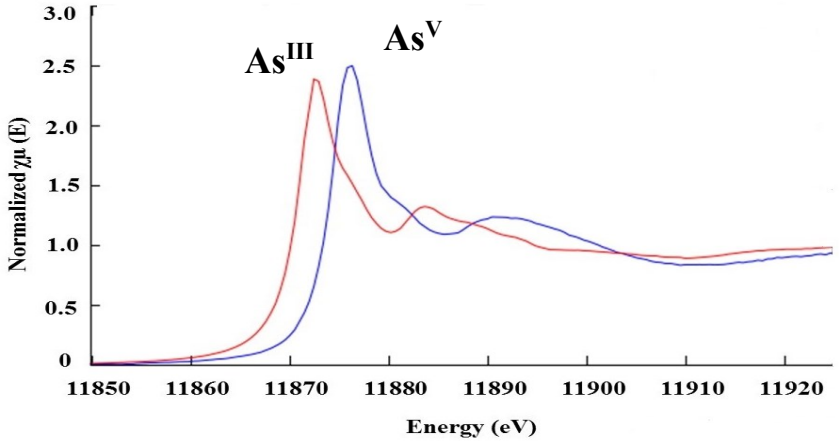


Figure 5.1 *XANES spectra at K-edge of As_2O_3 and $HNa_2AsO_4.7H_2O$ used to confirm oxidation states of arsenic on binary mixed oxides*

As was shown in section 4.3.1 the edge positions are at E^0 11871.4 and 11875.1 eV for As^{III} and As^{V}, respectively (which is consistent with previously reported values of 11871.7 and 11875.3 eV for As^{III} and As^{V}, respectively [19].

5.3.2 Effect of irradiation on photooxidation of As^{III} to As^{V} in the absence of binary mixed oxides

Possible oxidation of As^{III} in solution by radiation (UV and synchrotron) was first examined.

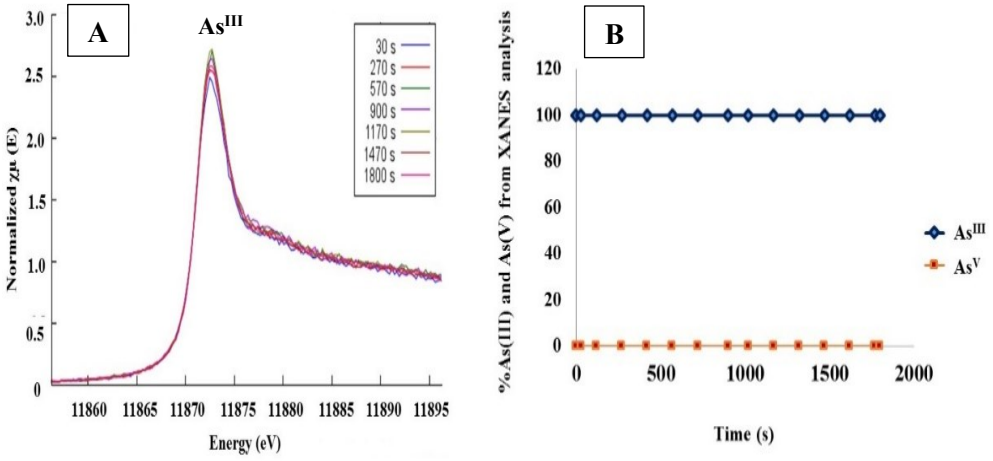


Figure 5.2 *100 mg As^{III} L^{-1} solution irradiated using synchrotron beam during 30 min (A) XANES spectra of As^{III} solution, (B) percentage of As^{III} and As^{V} in solution*

It has been previously reported by Canche-Tello et al., [20] that synchrotron beam with high energy can photocatalytically oxidise As^{III} to As^{V} (up to 40% conversion in 70 min) in aqueous solution (without the need of photocatalysts). Therefore, we were interested in determining the percentage of As^{III} in solution that is photo-oxidised by the synchrotron beam under the conditions used in our experiments. The XANES spectra (Figure 5.2 A) show that As^{III} is found at the same edge position after radiation of an aqueous solution without TiO_2/Fe_2O_3 binary mixed oxides for 30 minutes. This indicates that the synchrotron beam under these conditions cannot photo-oxidise As^{III} in solution to As^{V}. The results in Figure 5.2 (B) also show the ratio of As^{III}/As^{V} in solution is 1:0 (or 100:0 %, As^{III}: As^{V}).

The next control experiment was to confirm whether, the synchrotron beam combined with UV(18W) irradiation (30 min) would photo-oxidize As^{III} in solution (and in the absence of bicomposites).

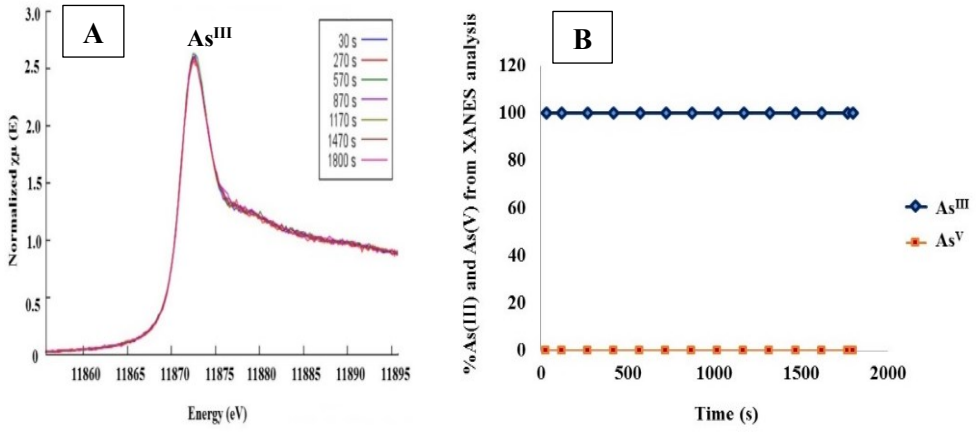


Figure 5.3 *100 mg As^{III} L^{-1} solution irradiated using UV(18W) up to 30 minutes and subsequent determination of As^{III} using synchrotron beam, (A) K-edge of As^{III} in the XANES spectra of the solution, (B) percentage of As^{III} and As^{V} in solution*

Similarity to what was observed in the previous control experiment, the XANES spectra (Figure 5.3) confirmed that the combination of synchrotron and UV irradiation did not photo-oxidise As^{III} to As^{V} in solutions.

5.3.3 Photocatalytic oxidation of As^{III} to As^{V} on the surface of TiO_2/Fe_2O_3 binary mixed oxides with UV(18W) irradiation

Having confirmed that the As^{III} is not oxidized by UV or synchrotron irradiation in the absence of binary mixed oxides, we then moved on to the catalytic properties of the different binary mixed oxides synthesized in this project (see Chapter 3). CP, MB and SG- TiO_2/Fe_2O_3 binary mixed oxides were exposed to solutions of As^{III} so that this species would adsorb. Subsequently, As^{III} bound

TiO_2/Fe_2O_3 binary mixed oxides were irradiated with a UV(18W) lamp for 6 h and changes in As^{III}/As^{V} levels monitored by XANES at different time points.

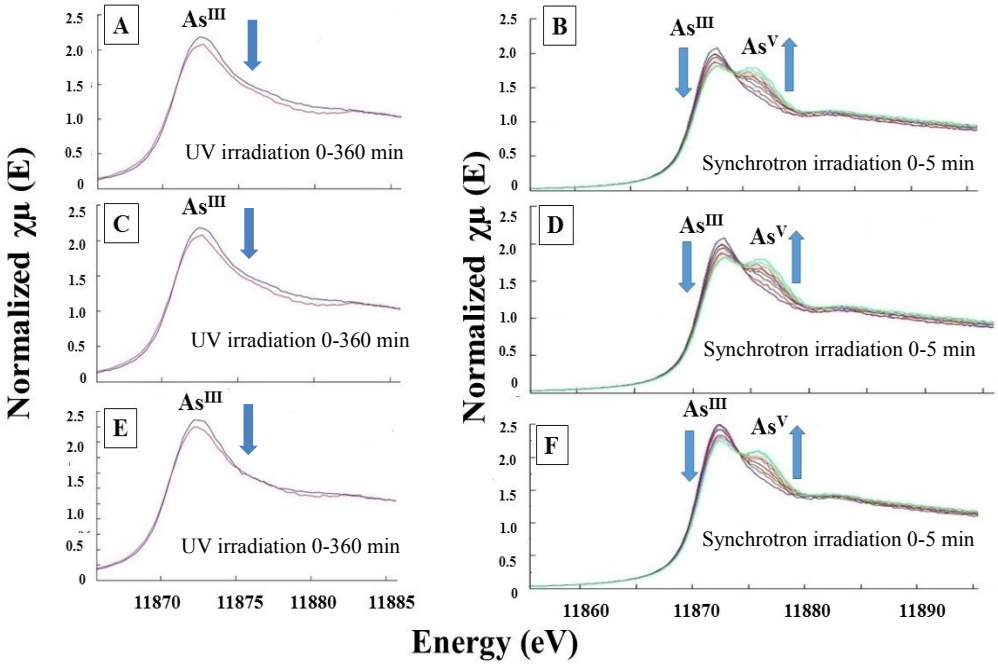


Figure 5.4 *Effect of UV (18W) irradiation on photocatalytic oxidation of As^{III} to As^{V} after adsorption on the surface of TiO_2/Fe_2O_3 binary mixed oxides. XANES spectra of the surface of: (A) CP-, (C) MB- and (E) SG- TiO_2/Fe_2O_3 binary mixed oxides with 6 h of UV(18W) irradiation. XANES spectra of the surface after exposure to synchrotron beam on the same samples to confirm the peak of As^{V} on (B) CP, (D) MB and (F) SG.*

The XANES spectra (recording during the 1st scan to avoid oxidation by synchrotron beam) of As^{III} on binary mixed oxides at arsenic K-edge are shown in Figure 5.4 (A), (C) and (E) for CP, MB and SG, respectively. In all types of binary mixed oxides, the intensity of the band associated to As^{III} (at E^0 = 11871.4 eV) decreases as a function of time. The intensity of the As^{III} peak drops after 6 h UV(18W) light irradiation. However, this decrease is small, suggesting the energy of the UV(18W) radiation dose not quantitatively oxidized As^{III} on the surface of the binary mixed oxide samples.

To quantify the ratio of As^{III} to As^{V} on the surface of binary mixed oxides, the intensities of As^{III} and of As^{V} peaks in the XANES spectra were used. With UV(18W) radiation, CP and MB can oxidize As^{III} to As^{V} on their surface with approximately 3.17 and 3.83 % for CP and MB within 6 h irradiation, respectively. We do not observe any photocatalytic oxidation of As^{III} with SG.

The results of UV(18W) light irradiation in Figure 5.4 (A), (C) and (E) are not clear to observe the intensity of As^{V} XANES spectra. Therefore, we used the synchrotron beam irradiating onto the surface of the samples and found the XANES spectra of As^{V} intensity increase more and more at As^{V} edge position. The results after irradiating synchrotron beam on those samples are presented in Figure 5.4 (B), (D) and (F) for CP, MB and SG, respectively. These results clearly show the formation of As^{V} by photocatalytic oxidation of As^{III} on the surface of binary mixed oxides.

5.3.4 Photocatalytic oxidation of As^{III} to As^{V} on the surface of TiO_2/Fe_2O_3 binary mixed oxides with synchrotron beam irradiation

In this experiment, the photocatalytic oxidation of As^{III} on the three different TiO_2/Fe_2O_3 binary mixed oxides was studied by irradiating synchrotron beam onto the surface of As^{III} bound binary mixed oxides and also detecting the XANES spectra of As^{III} at different time intervals.

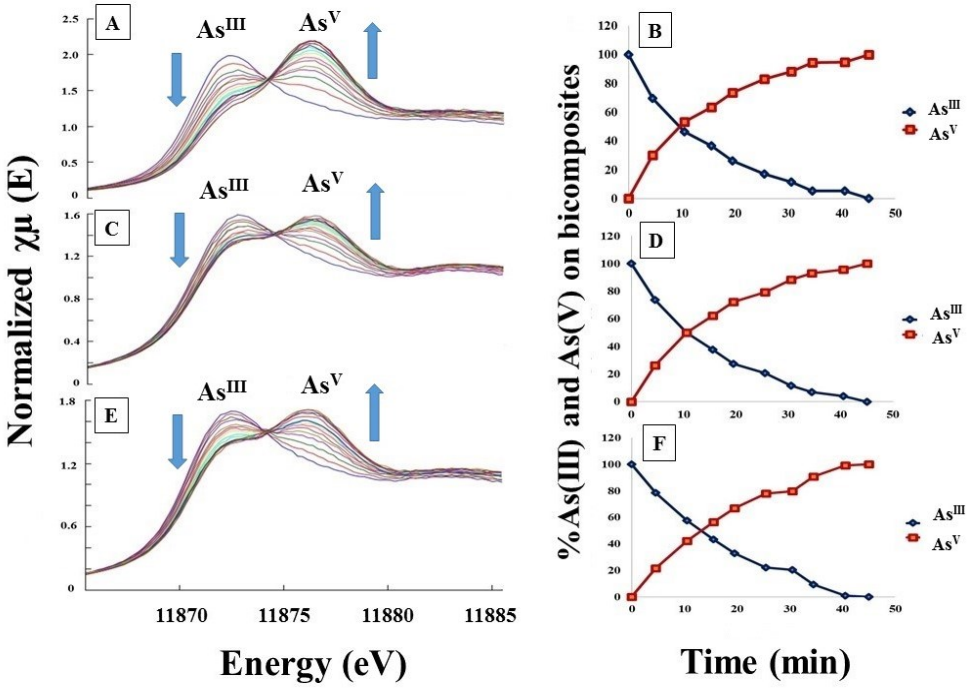


Figure 5.5 *Effect of synchrotron radiation on the photocatalytic oxidation of As^{III} on the surface of TiO_2/Fe_2O_3 binary mixed oxides. XANES spectra of arsenic on the surface of (A) CP, (C) MB and (E) SG TiO_2/Fe_2O_3 binary mixed oxides within 45 minutes. Panel B, D and F show the corresponding conversion of percentage As^{III} to percentage As^{V}*

The results are shown in Figure 5.5 (A), (C) and (E) for CP, MB and SG, respectively. At time zero (1st scan) the maximum in the spectrum is at E^0 = 11871.4 eV which confirms the presence of As^{III}. After irradiation with the synchrotron beam for 30 s (2nd scan), the XANES spectrum shows a decrease in the intensity of the peak associated to As^{III}, and an increase of the intensity of the band at E^0 = 11875.1 eV, which corresponds to As^{V}. These changes continue progressively with longer irradiation times. All the binary mixed oxides show the same overall behavior, namely that upon synchrotron beam irradiation they photocatalyse the oxidation of As^{III} to As^{V} (see Figure 5.5). XANES spectra of all samples were used to determine the ratio of As^{III}/As^{V} on the surface of binary mixed oxides and brought to estimate the photocatalytic oxidation rate of As^{III} as

shown in Figure 5.5 (B), (D) and (F). The results show full oxidation within 45 min.

5.3.5 Photocatalytic oxidation of As^{III} in aqueous solution using a tea-bag containing the TiO_2/Fe_2O_3 binary mixed oxides and synchrotron irradiation

In this experiment, TiO_2/Fe_2O_3 binary mixed oxides were packed in the tea-bag to avoid the binary mixed oxides particle dispersion into the solution. The changes of As^{III} in the solution were investigated to see how much As^{III} can photocatalytic oxidize in this system with synchrotron beam irradiation. The setting up experiment is shown in Figure 5.6 (A). The intensity of As^{III} in solution was measured using XANES analysis to indicate the initial intensity of As^{III} XANES spectra. Then, the tea-bag of binary mixed oxides was added in the solution and carried out the photocatalytic oxidation reaction in the reactor.

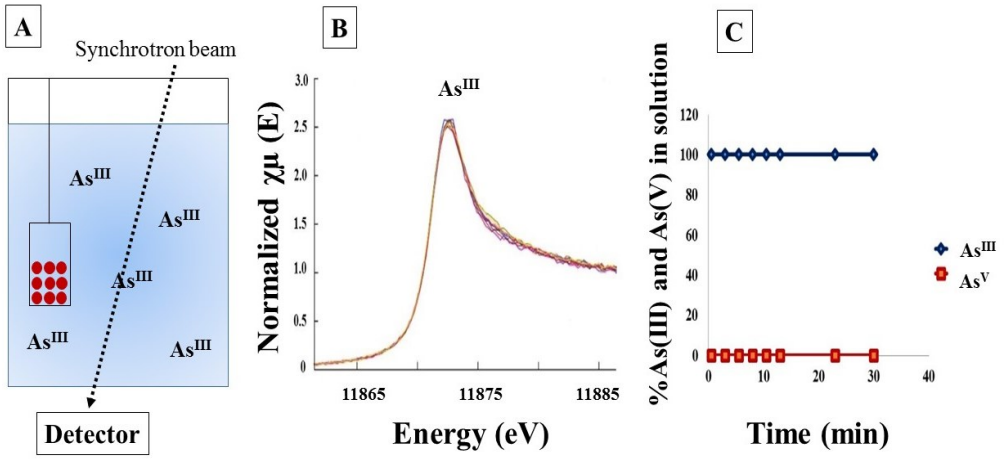


Figure 5.6 *Investigation of the photocatalytic oxidation of As^{III} in aqueous solution using 2g of MB in the tea-bag (50 mM borate buffer pH 9), (A) Schematic representation of the experimental set up using the binary mixed oxides packed in a tea-bag and subsequently placed into the photo reactor, (B) XANES spectra and K-edge of As^{III} of the system at different time intervals; (C) Calculated percentage As^{III} and percentage As^{V} in solution*

The photocatalytic oxidation in aqueous solutions was studied in this part of the experiment by using 2g MB packed in tea-bag added into an As^{III} 100 mg L^{-1} solution in perspective photo reactor. The XANES spectra shown in Figure 5.6 (B) indicate that As^{III} in solution has not undergone oxidation (same edge position at E^0 = 11871.4 eV); furthermore the intensity of the band associated to As^{III} did not decrease indicating that there is no adsorption of As^{III} onto the binary mixed oxides contained in the tea-bag. Consequently, the tea-bag was cut to let the binary mixed oxides diffuse through the As^{III} containing solution (see Figure 5.7 (A)).

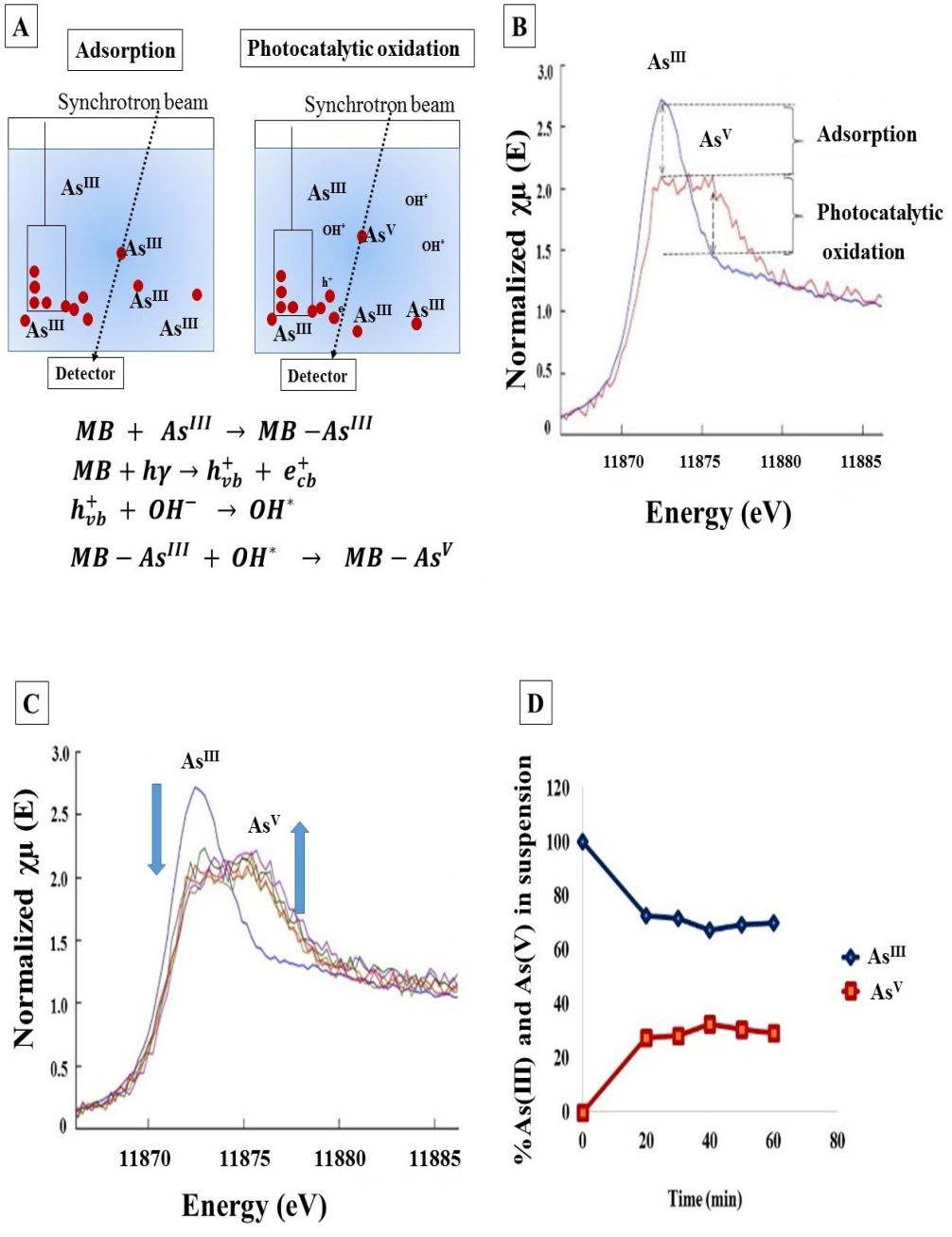


Figure 5.7 *Photocatalytic oxidation of As^{III} in aqueous solution at pH 5 using 2g of MB placed in a tea-bag with a small hole to let MB diffuse through the solution during synchrotron beam irradiation. XANES spectra at K-edge of arsenic at different time intervals. (A) The MB tea-bag set up in photo-reactor was cut; (B) XANES spectra at start of experiment and after adsorption has occurred 15 min later; (C) Overlay of arsenic XANES spectra; (D) Percentage of As^{III} and As^{V} on the surface of binary mixed oxides*

The XANES spectra in Figure 5.7 (B) and (C) show that the intensity of As^{III} decreased as a function of time while the intensity of As^{V} increased. The % As^{III} and As^{V} on the surface of binary mixed oxides was determined by XANES at different time intervals (Figure 5.7 (D)). The findings of the experiment are best explained by MB particles diffusing from tea-bag into solution, As^{III} subsequently was adsorbed from the solution onto the surface of the binary mixed oxides and photocatalytically oxidized to As^{V} (see Figure 5.7 (A) and (B)).

The tea-bag used in this experiment (see Figure 5.6) was approximately 1 mm thick that the As^{III} in solution could not directly interact with the binary mixed oxides particle. Therefore, no adsorption or photocatalytic oxidation reaction were observed. On the other hand, when the tea-bag was cut (see Figure 5.7) the binary mixed oxide particles can diffuse into the solution allowing As^{III} to directly interact with the binary mixed oxides, with the subsequent photocatalytic oxidation reaction.

5.3.6 Photocatalytic oxidation of As^{III} in aqueous solution using TiO_2/Fe_2O_3 binary mixed oxide suspension with synchrotron beam irradiation in photo reactor

In this experiment, 2 g of TiO_2/Fe_2O_3 binary mixed oxides were suspended in aqueous solution at pH 5 and 9 and irradiated using synchrotron radiation. Arsenic K-edge XANES spectra in fluorescence mode were recorded as function of time (every 30 s) and are shown in Figure 5.8.

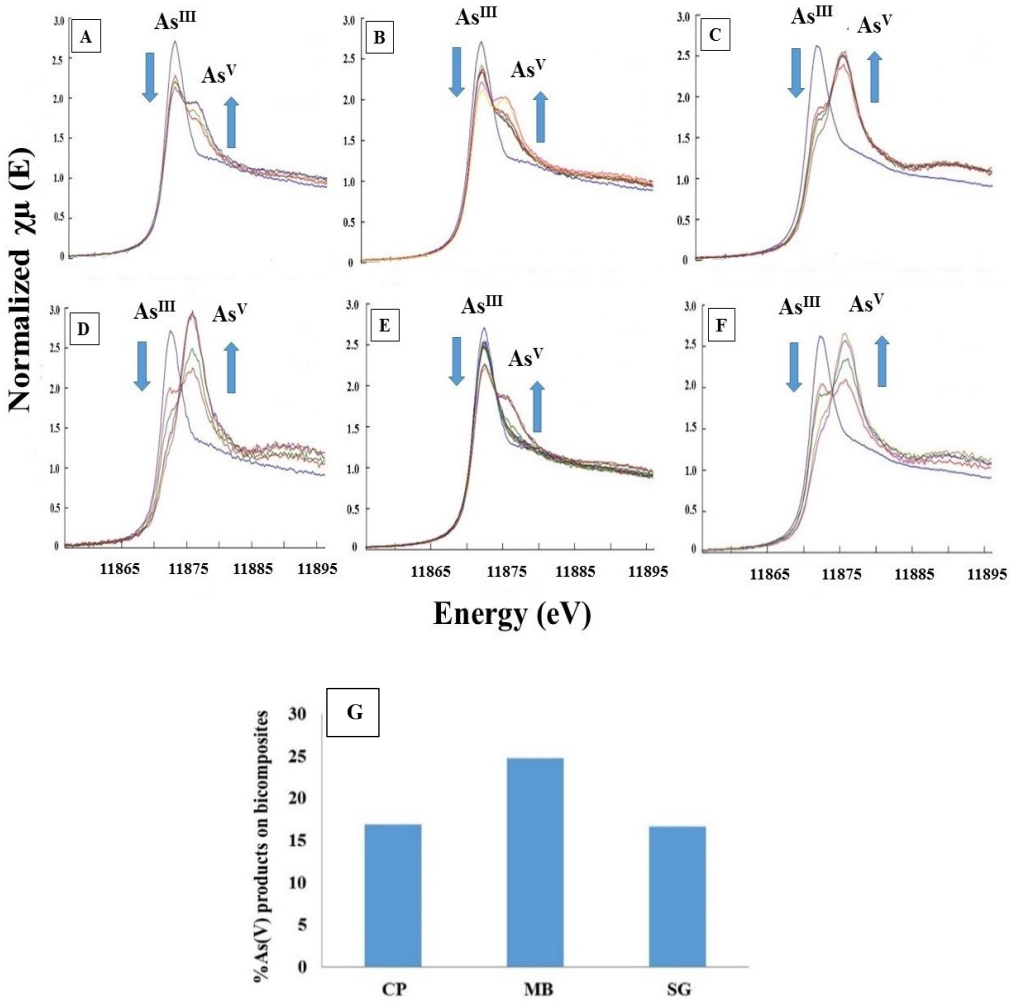


Figure 5.8 *Progress of the photocatalytic oxidation of As^{III} in solution with 2 g of binary mixed oxides suspended and using synchrotron beam irradiation, XANES K-edge spectra for: (A) CP, (B) MB and (C) SG at pH 5 (50 mM acetate buffer), and (D) CP, (B) MB and (F) SG at pH 9 (50 mM borate buffer). Panel (G) compares the percentage of As^{V} formed using CP, MB and SG (pH 9) after 7.5 min.*

The XANES spectra shown in Figure 5.8 (A) – 5.8 (F) indicate that the intensity of the As^{III} band decreases rapidly between the first and second spectra while the As^{V} band increases from the second scan onwards. This is likely due to the adsorption of As^{III} from solution and photocatalytic oxidation onto the binary mixed oxides. These results agree with previous works reported by Zhou et al.,

[21], Zhang et al., [22] and Yu et al., [23]. After the first scan, the K edge of As^{V} appears in the XANES spectra indicating that As^{III} can be photocatalytically oxidized in the binary mixed oxides suspension.

These XANES spectra were subsequently used to quantify the ratio of As^{III} to As^{V} on the binary mixed oxides at different times. These results using CP, MB and SG are compared in Figure 5.8 (G) which show $\%As^{V}$ on the surface of MB is higher than CP and SG.

In summary, the finding that the photocatalytic oxidation of As^{III} takes place if the binary mixed oxides is suspended in aqueous solution (Figure 5.8) but not when isolated in a tea-bag (Figure 5.6 and 5.7) suggests that the reaction is catalyze on the metal oxide surface.

5.3.7 Photocatalytic oxidation of As^{III} to As^{V} using mesoporous TiO_2/Fe_2O_3 binary mixed oxide suspension

We then studied the photocatalytic oxidation of As^{III} using UV irradiation and the mesoporous TiO_2/Fe_2O_3 binary mixed oxides in suspension. The changes of As^{III} and of total As concentrations resulted from the reaction were monitored using voltammetry.

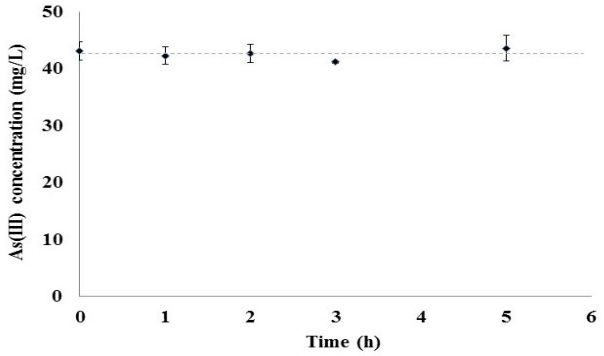


Figure 5.9 *Irradiation of As^{III} solution using a UV 18 W lamp in the absence of MB (50 mM HEPES buffer pH 7)*

As a control, we first irradiated an As^{III} aqueous solution with UV(18W) in the absence of MB. As can be seen from Figure 5.9, no oxidation to As^{V} was observed.

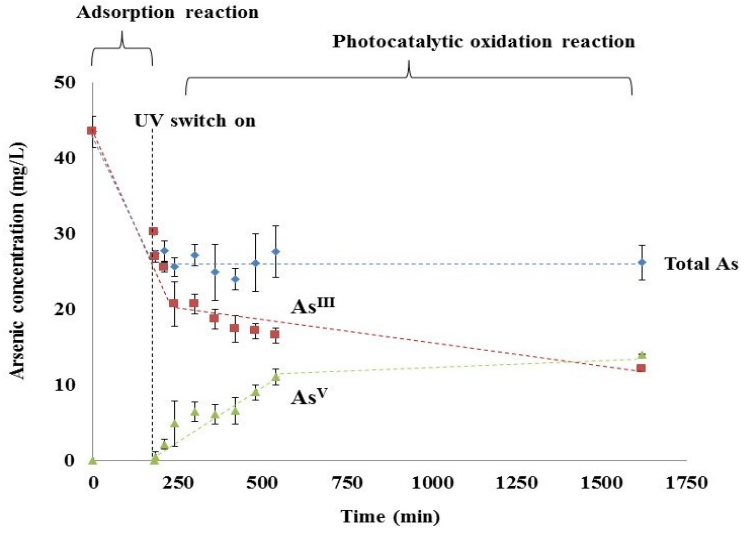


Figure 5.10 *Photocatalytic oxidation of As^{III} with mesoporous TiO_2/Fe_2O_3 binary mixed oxide (MB) suspended in 50 mM HEPES buffer at pH 7 with UV 18 watt irradiation*

Figure 5.10 presents the results from photocatalytic oxidation study of As^{III} using MB and UV(18 watt) irradiation over 24 h. In the first step, the adsorption reaction of As^{III} on the surface active sites of MB were carried out for 180 min to ensure the adsorption reaction of As^{III} reached the equilibrium on the surface of the binary mixed oxides. After this, the UV light was switched on to start the photocatalytic oxidation reaction. From the plots in Figure 5.10, it can be seen that the concentration of As^{III} in solution gradually decreased and reached equilibrium within 180 min. The initial As^{III} concentration used in this experiment was set up higher than the adsorption capacity of As^{III} on MB. Therefore, after adsorption equilibrium point, some As^{III} should still be left in solution. After 180 min of contact between the As^{III} solution and MB (to allow for adsorption), the UV light was switched on. As can be seen in Figure 5.10, we

found that the concentration of As^{III} left in the solution slowly decreased over time while the concentration of As^{V} in solution increased. The concentration of total As in solution after switching on the UV light was monitored to confirm that the decrease of As^{III} was not as a result of the adsorption reaction but from the photocatalytic oxidation of As^{III} to As^{V} by MB. The results in our studies indicate that MB can be used to photocatalytically oxidize As^{III} to As^{V} in aqueous solution by irradiating with UV light which agree with previous work reported by Lee and Choi [24] that study the photocatalytic oxidation of As^{III} using TiO_2 suspension adding Fe^{3+} with UV irradiation.

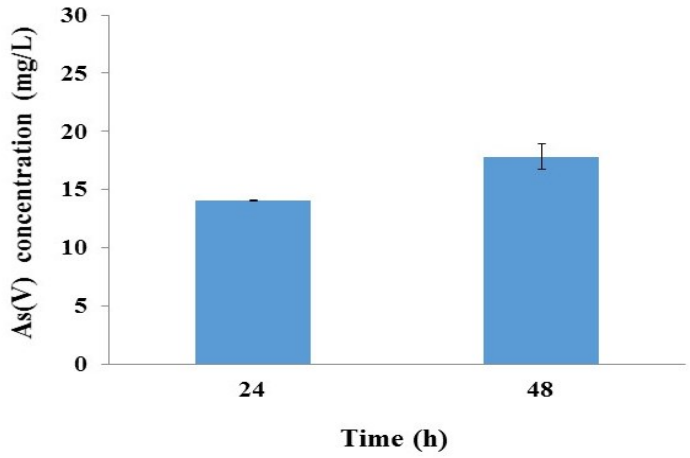


Figure 5.11 *Concentration of As^{V} formed from photocatalytic oxidation of As^{III} after 24 and 48 hours using mesoporous TiO_2/Fe_2O_3 binary mixed oxide (MB) suspension in 50 mM HEPES buffer pH 7 using UV 18W irradiation.*

Figure 5.11 shows the effect of irradiation time on As^{III} photocatalytic oxidation to As^{V} using MB and UV light. The data show a very little difference between the 24 and 48 h irradiated sample. Therefore, it is possible to conclude that by 24 h the system has reached equilibrium.

5.3.8 The possible role of hydroxyl radical in the oxidation process

The hydroxyl radical (OH*) has been proposed to be an important oxidative species for the photocatalytic oxidation of As^{III}. This radical can be generated on the surface of TiO_2 [25] or Fe_2O_3 [6]. Both Ti and Fe metal oxides reacting with photons of light can produce valence band holes (h_{vb}^+) which can combine with the hydroxide ion (OH^-) to achieve hydroxyl radicals [25]. Having established that MB can photocatalytically oxidise As^{III} to As^V in aqueous solution, it was of interest to investigate whether hydroxyl radicals generated on the surface of MB with UV light were involved in this process.

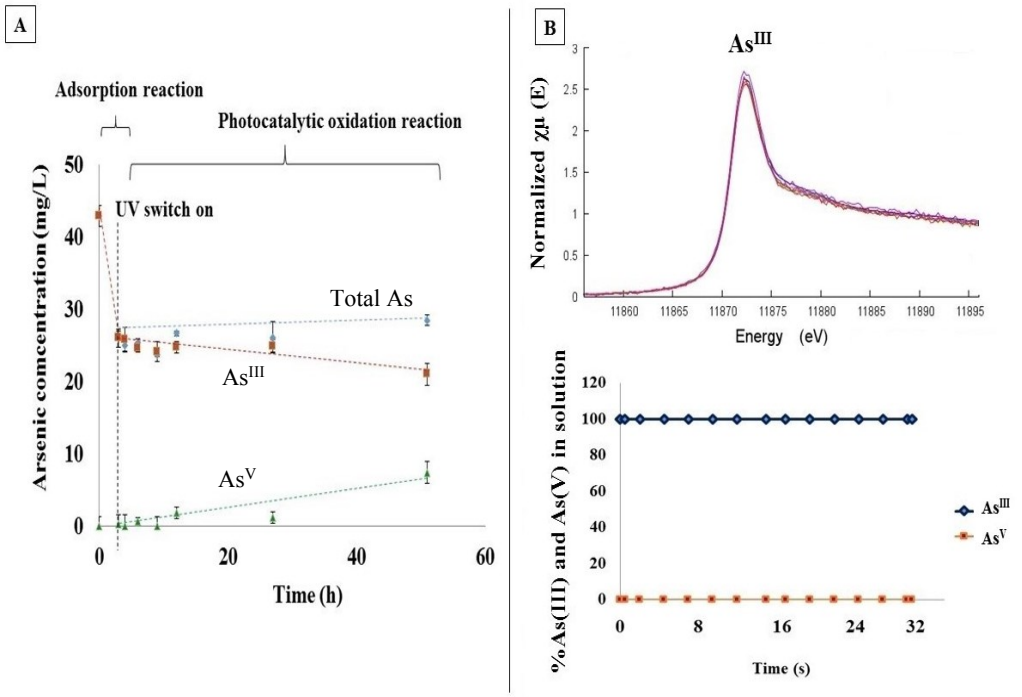


Figure 5.12 *Effect of added hydroxyl radical scavenger (salicylic acid) on photocatalytic oxidation of As^{III} in aqueous solution using binary mixed oxides. The mass ratio of binary mixed oxides to salicylic acid is 1. Oxidation using: as radiation (A) UV18 W irradiation; (B) synchrotron beam*

To this aim, a number of experiments were carried out using, salicylic acid as a hydroxyl radical scavenger. The effects of salicylic acid on As^{III} photocatalytic oxidation using MB (Salicylic acid: MB, 1:1 by mass) are presented in Figure 5.12(A) and 5.12(B). As can be seen from these plots, the As^{III} concentrations (in the presence of MB and irradiated with UV light) did not decrease significantly over time (Figure 5.12(A)). This suggests that the valence band hole (h^{+}_{vb}) generated from radiation of the binary mixed oxides surface is reacting with hydroxide ion (OH^{-}) to produce hydroxyl radical (OH^{*}) which in turn is oxidizing As^{III}. When the hydroxyl radical is scavenged by the salicylic acid, the performance of photocatalytic oxidation reaction which results in the decrease of As^{V} in the solution is reduced. Therefore, both experiments suggest that hydroxyl radical produced on the surface of MB play an important role in the photocatalytic oxidation As^{III}.

Furthermore, salicylic acid and its derivatives can also scavenge superoxide [26] which is one of oxidative species that can photocatalytically oxidize As^{III} to As^{V}. Therefore, in our study system, superoxide produced by MB could also be scavenged by salicylic acid.

5.3.9 Photocatalytic oxidation kinetic rate calculations

The kinetic models frequently used to estimate the rate of adsorption are a pseudo first and second order [27]. We used these models to study the adsorption rate of As^{III} on the bicomposites reported by D'Arcy et al., and Chapter 3 of this research. Various works have used these kinetic models to calculate the oxidation rate of As^{III} using photocatalysts [28, 29, 30, 31]. Bissen et al., [28] showed that the pseudo first order kinetic model can be used to calculate the photocatalytic oxidation rate of As^{III} using TiO_2 [28]. The pseudo first order kinetic model has also been used to determine oxidation rate of As^{III} by TiO_2 photocatalysts in previous report by Nakgima et al., [29], Kin et al., [30] and Yang et al., [31].

Therefore, in this work we investigated whether the pseudo first order kinetic model would be appropriate to fit our photocatalytic oxidation of As^{III} data in the presence of binary mixed oxides (on the surface with synchrotron radiation and in the suspension with UV radiation).

It was previously proposed that the surface mediated oxidation of As^{III} follows a pseudo first order reaction.

$$\frac{d[As^V]}{dt} = -\frac{d[As^{III}]}{dt} = k_{ox}\left([As^V]_{eq} - [As^{III}]_t\right) \qquad (5.1)$$

The logarithic form of equation 5.1 is,

$$\log\left([As^V]_{eq} - [As^V]_t\right) = \log[As^V]_{eq} - \left(\frac{k_{ox}}{2.303}\right).t \qquad (5.2)$$

In which, $[As^V]_{eq}$ and $[As^V]_t$ are the concentration of As^V product for photocatalytic oxidation reaction at equilibrium and at a given time respectively in mg L^{-1}, respectively, k_{ox} represents the photocatalytic oxidation kinetic rate constant (in min^{-1}) and, t is the reaction time (in min).

The rate constant for photocatalytic oxidation reaction was estimated by plotting $\log\left([As^V]_{eq} - [As^V]_t\right)$ against t. Using linear regression ($y = mx + c$):

$$Slope = \frac{k_{ox}}{2.303} \qquad (5.3)$$

where k_{ox} is the rate constant.

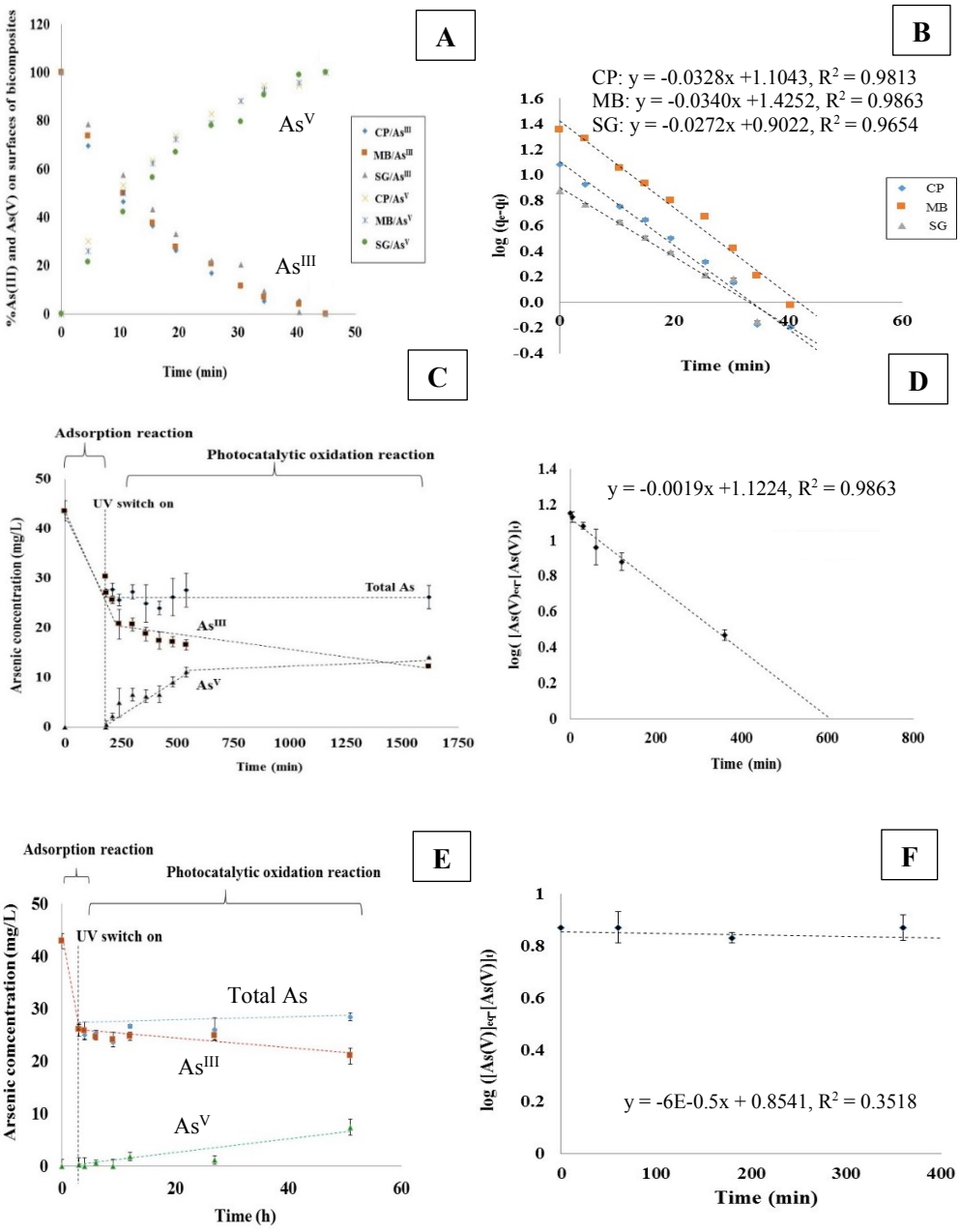


Figure 5.13 *(A) Photocatalytic oxidation kinetics of As^{III} using the synchrotron irradiation on the surface of CP, MB and SG, and (B) corresponding pseudo-first order model plots. (C) Photocatalytic oxidation kinetics of As^{III} using UV18 watt irradiation on the surface of MB; and (D) corresponding pseudo-first order model plots. (E) The effect of hydroxyl radical scavenger on the photocatalytic oxidation of As^{III} to using MB suspension with UV 18 watt irradiation is also shown.*

The oxidation kinetics of As^{III} on the surface of three different binary mixed oxides using synchrotron beam irradiation are shown in Figure 5.13 (A) and the corresponding kinetic calculation plots are presented in Figure 5.13 (B).

The oxidation kinetic of As^{III} on the surface of the MB using UV18 watt irradiation are shown in Figure 5.13(C) and the corresponding kinetic calculation plots are presented in Figure 5.13(D).

The linear regression using a pseudo first order kinetic model show very good correlations with R^2 ranging between 0.96 and 1.00 (Table 5.2).

The calculated rate constants for photocatalytic oxidation reaction using the different binary mixed oxides are compared in Figure 5.14.

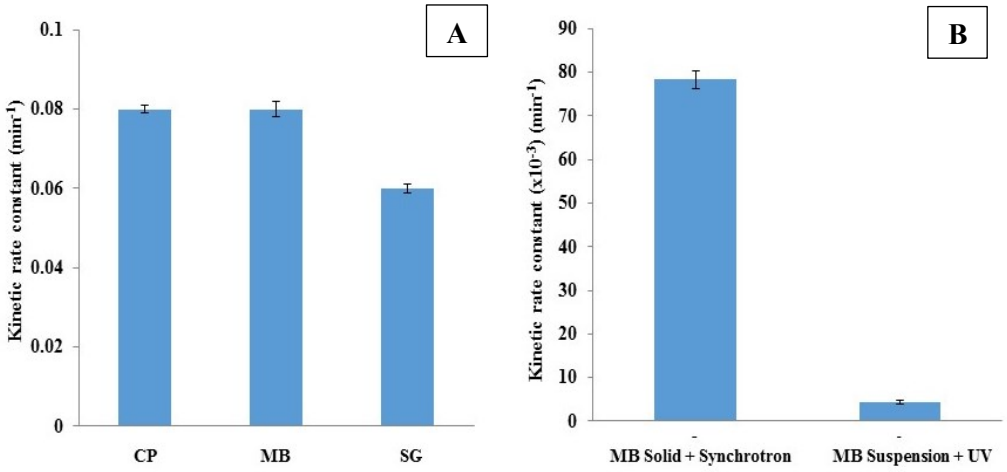


Figure 5.14 *(A) Comparison of photocatalytic oxidation rate constant (k_{ox}) on the solid surface of CP, MB and SG using synchrotron irradiation, and (B) on the solid surface of MB using synchrotron irradiation and MB suspension using UV 18 watt*

The photocatalytic oxidation rate constant (k_{ox}) of As^{III} to As^{V} on the solid surface of CP, MB and SG were found to be 0.078, 0.075 and 0.063 min^{-1}, respectively (Figure 5.14 (A)). It can be concluded that all types of TiO_2/Fe_2O_3 binary mixed oxides can photocatalytically oxidise As^{III} to As^{V} under synchrotron beam irradiation with similar rates. The mineralogical characterization of all the materials used in this work, show that they have

combine anatase and hematite phases. Our work suggests that the synthetic methods do not significantly affect the oxidation rates.

Additionally, the photocatalytic oxidation rates on solid surface of MB with synchrotron beam irradiation and in aqueous solution with UV(18W) irradiation were compared (Figure 5.14 (B)). The photocatalytic oxidation rate constant of As^{III} to As^{V} using MB in aqueous system with UV irradiation was found to be $4.37x10^{-3}$ min^{-1}. In contrast, a higher rate constant (at 7.83×10^{-2} min^{-1}) was obtained for the sample oxidized on solid surfaces of MB with synchrotron beam. It could be resulted from the high energy intensity of synchrotron irradiation introducing the faster photocatalytic oxidation reaction of As^{III} found in the same way on the surface of the binary mixed oxides generating oxidative species. These findings are in agreement with previous work reported by Dutta et al., [32]. They studied the effect of the light intensity on the photooxidation process and found the As^{III} oxidation rates are higher when increasing the intensity of light [32]. Furthermore, they reported that hydroxyl radical produced on the surface of binary mixed oxides were the species responsible for the oxidiation of As^{III} to As^{V}, which is also consistent with our results.

Having established the rate constants under different irradiation conditions, we were interested in study these rates at different time intervals. Most of research normally reports the kinetic rate of the over all reaction. However, as has already been discussed in previous chapters, we have previously found that the rate model depends on the time interval that is being studied [2]. At the beginning of the reaction, the oxidation rates are very high (i.e. very fast reactions) but they slowly decrease as they reach equilibrium. Therefore, we monitored the oxidation rates at three different times including initial, middle and final stages which are shown in Figure 5.15.

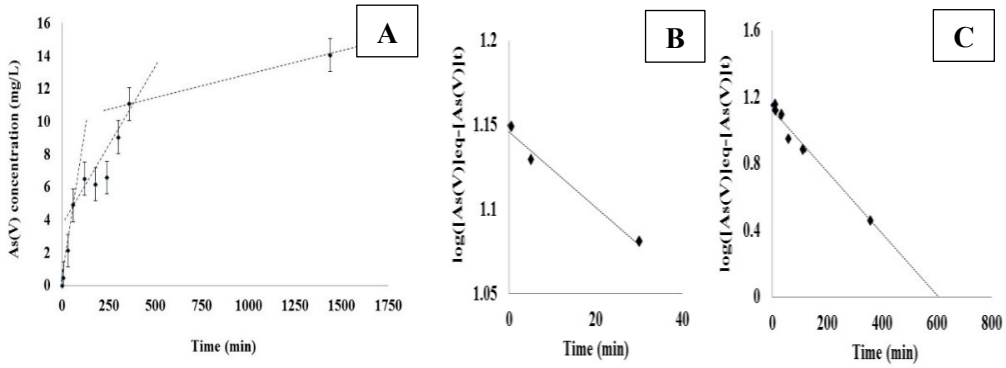


Figure 5.15 *Time profiles of As^{V} products from As^{III} photocatalytic oxidation using MB suspension with UV 18 watt irradiation, (A) Concentration of As^{V} at different times, (B) kinetic calculation plots for medium rate 0-30 min and (C) overall rate 0-600 min*

Table 5.2 *Photocatalytic oxidation rate constants for As^{III} calculated from experimental data*

Sample		Reaction time	Linear equation	R^2	k_{ox} (min^{-1})
As^{III}-CP/Synchrotron	solid	0-45 min	y = -0.0328x+1.1043	0.984	0.075
As^{III}-MB/Synchrotron	solid	0-45 min	y = -0.0340x+1.4252	0.981	0.078
As^{III}-SG/Synchrotron	solid	0-45 min	y = -0.0272x+0.9022	0.965	0.063
As^{III}-MB/UV 18 W	suspension	0-1440 min 0-30 min 0-5 min	y = -0.0019x+1.1224 y = -0.0022x+1.1460 y = -3.3652x+ 5.0000	0.986 0.9845 1.0000	$4.37x10^{-3}$ $5.07x10^{-3}$ 7.75
As^{III}-MB/UV 18W/ Salicylic acid (Hydroxyl radical scavenger)	suspension	0-1440 min	Y=0.00002x+0.862	0.016	$1.38\ x10^{-4}$

The plots of experimental data from photocatalytic oxidation of As^{III} using MB suspension monitoring with SWASV were separated to consider the fraction of rate constant at three different kinetic time periods. This included initial range between 0 and 5 min, medium range between 0 and 30 min and overall range between 0 and 1440 min. The results are summarized in Figure 5.15 and Table 5.2. As can be seen from this data, in the first 5 min the rate constant was at 7.75 min^{-1} while at 30 min and 1440 min the rate was much lower at 5.07 x 10^{-3} and 4.37 x 10^{-3} min^{-1}, respectively, show both period have rate constant in the same

ranges it could possibly conclude that the photocatalytic oxidation on the surface of MB in aqueous system approaches equilibrium within 30 min.

5.3.10 Design of photocatalytic oxidation reactor

The application of As^{III} removal process with MB will carry on in future work. The idea of the design will have two combinding units, photocatalytic oxidation reactor and continuous flow through column, which hope to conveniently use in the treatment plant. Therefore, the aim of this work is to study the photo-reactor that possibly simple use for oxidation of As^{III}.

Many photo reactors for the oxidation of As^{III} to As^{V} have been previously developed (see Table 5.3). The design of the photo-reactor used in this work for photocatalytic oxidation of As^{III} is shown in Figure 5.16.

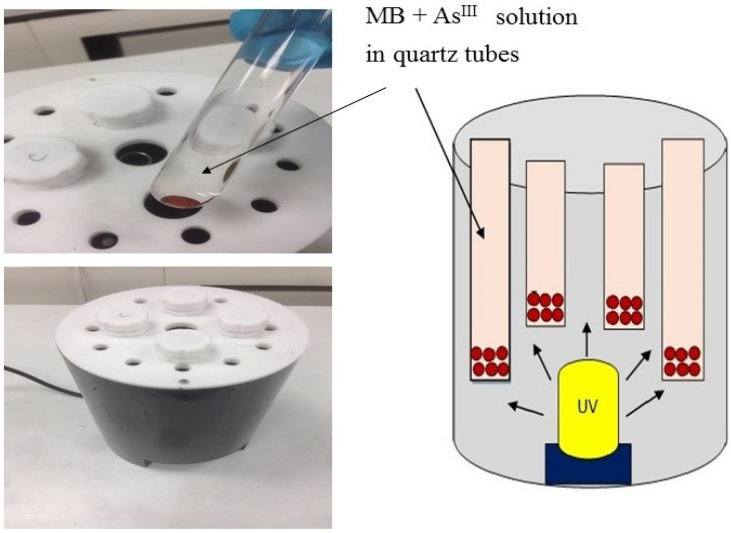


Figure 5.16 *Schematic representation of the photoreactor used in this work. The binary mixed oxides used was MB, contained in a quartz tube and irradiated with a UV 125 watt lamp. The reactor was placed inside a black metal box.*

Table 5.3 *Summary of reactor designs for photocatalytic oxidation studies*

Photocatalyst	Dose ($g\ L^{-1}$)	UV lamp (Watt)	[As^{III}] ($mg\ L^{-1}$)	pH	Reactor	Ref.
TiO_2	0.001-0.005	1000	0.1	5, 7, 9	-	[28]
TiO_2	1.5	300	374	3, 9	Pyrex	[8]
TiO_2	0.1	125	149	9	Glass plate	[32]
TiO_2	1.0	500	10	6.5-7.5	Pyrex flask	[19]
TiO_2	0.5	300	149	3	Ultrasonic bath	[33]
TiO_2	0.001	9	3	3.5, 6.5	Pyrex	[34]
SIO/TiO_2	2.0	500	20-100	3	Stainless black box	[13]
Pt/TiO_2	0.5	300	374	3	Pyrex	[35]
TiO_2/MMT	1.0	400	5	7	Glass vessel	[14]
γ-Fe_2O_3-TiO_2 nanoparticle	0.5	20	0.1-50	7	-	[15]
MB	1.0	18	40	7	Perspective box / Black box	This work
MB	1.0	120	40	7	Quartz/ black metal box	This work

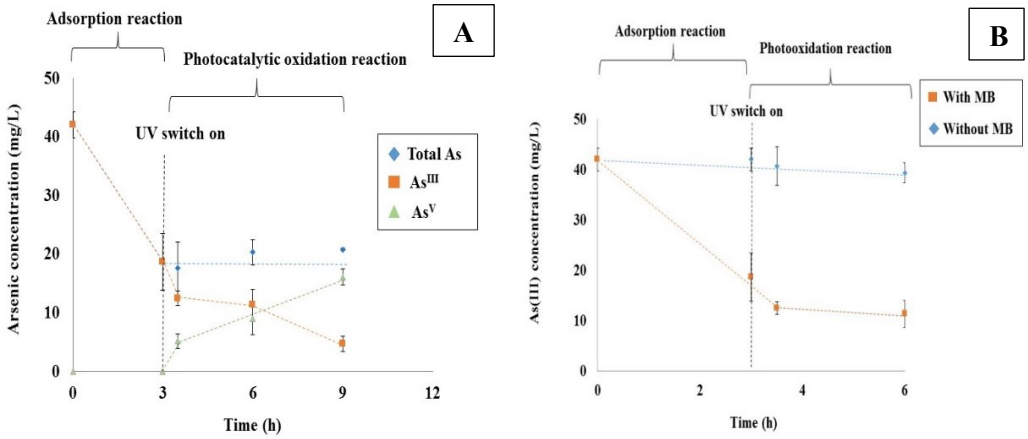


Figure 5.17 *Photocatalytic oxidation of As^{III} to As^{V} in aqueous solutions using MB suspension ($1.0\ g\ L^{-1}$) with UV 125 watt irradiation in 50 mM HEPES buffer pH 7: the photocatalytic oxidation reaction was carried out in quartz tube and photo reactor. (A) Arsenic concentration at different reaction times: (B) Photo-oxidation over time with and without MB (The standard deviations were calculated from three replications of experiments).*

To carry out the photocatalytic oxidations in the reactor. As^{III} was first adsorbed for 3 h to reach equilibrium (as previously determined – see section 5.3.7). At this point, it is expected that all active sites on the MB surface are occupied by As^{III} with some As^{III} still left in solution (Figure 5.17(A)). At this point, the UV lamp was switched on to carry out photocatalytic oxidation: after this, the amount of As^{III} in solution gradually decreases as function of times while the total arsenic in solution was still constant. The differences of As^{III} and total As concentrations were then used to estimate the concentration of As^{V} in solution. As expected, the amount of As^{V} in solution increased as function of times (Figure 5.17 (A)).

The adsorption capacity of As^{III} on MB depends on surface active sites (Chapter 3) but the photocatalytic oxidation property depends on valence band hole (h_{vb}^{+}) and conduction band electron (e_{cb}^{-}) which in turn depend on the overall mass of MB. From these experimental results, it can be concluded that after all MB active sites were occupied by As^{III}. The adsorption reaction was finished but photocatalytic oxidation still carry on with UV light. The MB still generates valence band hole (h_{vb}^{+}) combining with hydroxide (OH^{-}) in aqueous solution to generate hydroxyl radical (OH^{*}) and conduction band electron (e_{cb}^{-}) traps oxygen to produce superoxide (O_2^{*-}). Both species can oxidize As^{III} to As^{V} in solution.

A control experiment where the As^{III} sample was irradiated with UV-125 watt in the absence of MB, was carried out. As can be seen in Figure 5.17 (B), there was no significant decrease of As^{III} concentration in the absence of MB during the first 3 h (i.e. prior to UV irradiation): in contrast, in the presence of MB there was a significant decrease on As^{III} concentration in this period of time. This is due to the adsorption of As^{III} onto the MB (as discussed above).

After 3 h, the UV 125 watt was switched on and we found that As^{III} concentration in solution decreased between 3 to 6 h in the system with MB but not significantly in the system without MB. This evidence shows the effect that MB has as a photocatalyst. After 6 h, a slight decrease in As^{III} concentration in the system without MB was found. This suggests that over longer periods of time under

intense UV irradiation a small of As^{III} can be oxidized to As^{V} even in the absence of the binary mixed oxides.

5.3.11 Effect of UV lamp energy on photocatalytic oxidation of As^{III} to As^{V} using MB

We then investigated the effect that different UV irradiation (i.e. 18 vs. 125 watt) would have in the photocatalytic oxidation of As^{III}. Both experiments were carried out by using 40 mg L^{-1} As^{III} as initial concentrations, 1.0 g L^{-1} MB doses as photocatalyst and photo reaction times of 6 h at pH 7.

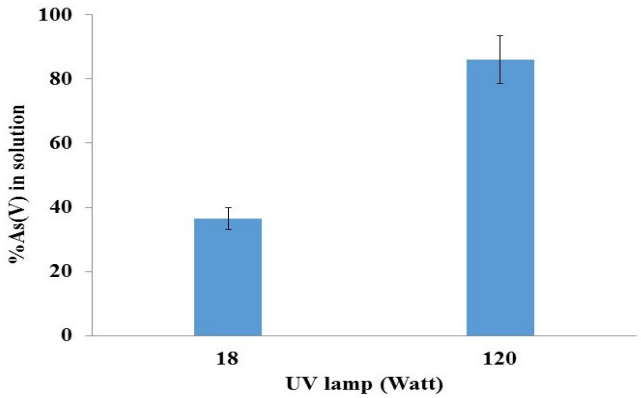


Figure 5.18 *Percentages of As^{V} products in solutions by photocatalytic oxidation using MB suspension with UV lamp 18 and 125 watt reactors within 6 h irradiation times.*

Figure 5.18 shows the effect of UV 18 watt and 125 watt lamp on the photocatalytic oxidation within 6 h. It clearly shows that irradiating with a 125 watt UV light (*ca.* 86% conversion), gives higher yields of As^{V} than when the sample was irradiated with an 18 watt UV lamp (*ca.* 36% conversion).

5.4 Conclusion

The three TiO_2/Fe_2O_3 binary mixed oxides under study in this thesis have been shown to be efficient photocatalysts for the oxidation of As^{III} to As^{V}.

Using XANES spectroscopy, we studied the kinetics of As^{III} photocatalytic oxidation to As^{V} on the surface of TiO_2/Fe_2O_3 binary mixed oxides with synchrotron beam irradiation. These experiments showed that the rate constant for the three materials under these conditions, is roughly the same (ranging between 0.062 and 0.078 min^{-1}). The data show that the photocatalytic oxidation reaches equilibrium within 45 min, with 100% As^{V} production.

In aqueous solution, irradiation with UV18 watt of an As^{III} solution in the presence of suspended MB also yielded As^{V} with a rate constant of around $4.37x10^{-3}$ min^{-1}. In this case, the photocatalytic oxidation reaction approached equilibrium point at *ca.* 30 min. Additionally, we observed that the reaction is much faster (k_{ox} = 7.75 min^{-1}) at short times (i.e. between 0 and 5 min).

The most important part to carry out photocatalytic oxidation reaction in this work is the surface of TiO_2/Fe_2O_3 binary mixed oxides which can generate valence band hole (h_{vb}^{+}) and conduction band electron (e_{cb}^{-}) to produce hydroxyl radical and superoxide to photocatalytic oxidise As^{III} to As^{V}. Furthermore, effect of hydroxyl radical scavenger study indicates that hydroxyl radicals produced on the surface of TiO_2/Fe_2O_3 binary mixed oxides are necessary for the oxidation of As^{III} to As^{V} by the binary mixed oxides.

References

(1) Mohan, D.; Pittman, C. U. *Journal of Hazardous Materials*. **2007**, *142*, 1-53.

(2) D'Arcy, M.; Weiss, D.; Bluck, M.; Vilar, R. *J. Colloid Interface Sci.* **2011**, *364*, 205-212.

(3) Zhou, W.; Fu, H.; Tian, C.; Qu, Y.; Lu, P.; Sun, C. C. *J. Phys. Chem. C*. **2008**, *112*, 19584-19589.

(4) Singh, R.; Singh, S.; Parihar, P.; Singh, V. P.; Prasad, S. M. *Ecotoxicol. Environ. Saf.* **2014**, *112*, 247-270.

(5) Yang, H.; Sun, W.; Ge, H.; Yao, R. *Environ. Sci. Technol.* **2015**, 1-8.

(6) Altun, M.; Sahinkaya, E.; Durukan, I.; Bektas, S.; Komnitsas, K. *J. Hazard. Mater.* **2014**, *269*, 31-37.

(7) Walter, F. J.; John, F.; Sarah, W.; Carolina, A.; Natalia I, G. N.; Rafael, Z. A.; Qilin, L.; PerdroJ.J, A. P.; Vicki, C.; Amy, K.; Mason, T. *Environ. Eng. Sci*. **2014**, *147*, 265-274.

(8) Lee, H.; Choi, W. *Environ. Sci. Technol*. **2002**, *36*, 3872-3878.

(9) Nakajima, T.; Xu, Y. H.; Mori, Y.; Kishita, M.; Takanashi, H.; Maeda, S.; Ohki, A. *J. Hazard. Mater.* **2005**, *120*, 75-80.

(10) Trois, C.; Cibati, A.; *Chem. Eng. J.* **2015**, *259*, 981-989.

(11) Azhdarpoor, A.; Nikmanesh, R.; Samaei, M. R.; *Environ. Tech*. **2015**, *36*, 2525-2531.

(12) Hristovski, K.; Baumgardner, A.; Westerhoff, P. *J. Hazard. Mater.* **2007**, *147*, 265-274.

(13) Zhang, F. S.; Itoh, H. *Chemosphere*. **2006**, *65*, 125-131.

(14) Li, Y.; Liu, J. R.; Jia, S. Y.; Guo, J. W.; Zhuo, J.; Na, P. *Chem. Eng. J.* **2012**, *191*, 66-74.

(15) Yu, L.; Peng, X.; Ni, F.; Li, J.; Wang, D.; Luan, Z. *J. Hazard. Mater.* **2013**, *246*, 10-17.

(16) Zhu, J.; Zheng, W.; He, B.; Zhang, J.; Anpo, M. *J. Mol. Catal. A Chem.* **2004**, *216*, 35-43

(17) Zhou, W.; Fu, H.; Tian, C.; Qu, Y.; Lu, P.; Sun, C. C. *J. Phys. Chem. C*. **2008**, *112*, 19584-19589.

(18) Smith, Y. R.; Joseph Antony Raj, K.; Ravi Subramanian, V.; Viswanathan, B. *Colloids Surfaces A Physicochem. Eng. Asp*. **2010**, *367*, 140-147.

(19) Smith, P. G.; Koch, I.; Gordon, R. A.,; Mandoli, D. F.; Chapman, B. D.; Reimer, K. J. *Environ. Sci. Technol.* **2005**, *39,* 248-254.

(20) Canche-Tello, J.; Vargas, M. C.; Hérnandez-Cobos, J.; Ortega-Blake, I.; Leclercq, A.; Solari, P. L.; Lezama-Pacheco, J.; Auwer, C. D.; Mustre de Leon, J. *J. Phys. Chem. A*. **2015**, *119*, 2829-2833.

(21) Zhou, W.; Fu, H.; Tian, C.; Qu, Y.; Lu, P.; Sun, C. C. *J. Phys. Chem. C*. **2008**, *112*, 19584-19589.

(22) Zhang, F. S.; Itoh, H. *Chemosphere*. **2006**, *65*, 125-131.

(23) Yu, L.; Peng, X.; Ni, F.; Li, J.; Wang, D.; Luan, Z. *J. Hazard. Mater.* **2013**, *246*, 10-17.

(24) Lee, H.; Choi, W. *Environ. Sci. Technol*. **2002**, *36*, 3872-3878.

(25) Nakajima, T.; Xu, Y. H.; Mori, Y.; Kishita, M.; Takanashi, H.; Maeda, S.; Ohki, A. *J. Hazard. Mater.* **2005**, *B120*, 75-80.

(26) Allgayer, H.; Hofer, P.; Schmidt, M.; Bohne, P.; Kruis, W.; Gugler, R.; *Biochemical Pharmacology*, **1992**, *43*, 259-262.

(27) Wainipee, W.; Weiss, D. J.; Sephton, M. A.; Coles, B. J.; Unsworth, C.; Court, R. *Water Res.* **2010**, *44*, 5673-5683.

(28) Bissen, M.; Vieillard-Baron, M. M.; Schindelin, A. J.; Frimmel, F. H. *Chemosphere*. **2001**, *44*, 751-757.

(29) Nakajima, T.; Xu, Y. H.; Mori, Y.; Kishita, M.; Takanashi, H.; Maeda, S.; Ohki, A. *J.Hazard. Mater.* **2005**, *120*, 75-80.

(30) Manning, B. A.; Fendorf, S. E.; Goldberg, S. *Environ. Sci. Technol.* **1998**.

(31) Yang, H.; Sun, W.; Ge, H.; Yao, R. *Environ. Technol.* **2015**, 1-8.

(32) Dutta, P. K.; Pehkonen, S. O.; Sharma, V. K.; Ray, A. K. *Environ. Sci. Technol.* **2005**, 39, 1827-1834.

(33) Choi, W.; Yeo, J.; Ryu, J.; Tachikawa, T.; Majima, T. *Environ. Sci. Technol.* **2010**, *44,* 9099–9104.

(34) Tsimas, E. S.; Tyrovola, K.; Xekoukoulotakis, N. P.; Nikolaidis, N. P.; Diamadopoulos, E.; Mantzavinos, D. *J. Hazard. Mater.* **2009**, *169*, 376-385.

(35) Ryu, J.; Choi, W. *Environ. Sci. Technol.* **2004**, *38*, 2928-2933.

Chapter 6

Conclusions and future work

6.1 Conclusions

The research presented in this thesis provided new insights into the arsenic adsorption mechanism and As^{III} photocatalytic oxidation mechanism onto TiO_2/Fe_2O_3 binary mixed oxides. Furthermore, it gives detailed kinetic information related to the photocatalytic oxidation mechanism of As^{III} to As^{V} mediated by these binary mixed oxides.

Three different methods to prepare TiO_2/Fe_2O_3 binary mixed oxides were employed based on previous literature. From these, mesoporous TiO_2/Fe_2O_3 binary mixed oxides (MB) demonstrated to be the best material due to its larger surface area, highest surface active sites, and highest adsorption capacities, as compared to the co-precipitation TiO_2/Fe_2O_3 binary mixed oxides (CP) [1] and sol-gel TiO_2/Fe_2O_3 binary mixed oxides (SG) [2]. We show that MB can be used for effective arsenic removal from aqueous solution.

The adsorption isotherms and kinetics studies have provided important insights into the mechanism of As^{III} adsorbed on MB. From these studies, it can be concluded that As^{III} adsorbs rapidly on the surface active sites of the binary mixed oxides. Adsorption isotherm studies show the Langmuir model is best to describe the adsorption mechanism of As^{III} on MB, suggesting that it forms monolayer via chemisorption. The adsorption capacities of As^{III} onto the surface active sites of MB are not significantly different at pH values between 5 and 9 probably due to the fact that As^{III} is found as the fully protonated species (i.e. no electrostatic charge) in this pH range. The intra-particle diffusion kinetic model describes the

adsorption rate of As^{III} from aqueous solution to MB's surface. The highest adsorption rate was found at short adsorption times.

The adsorption mechanism and the arsenic binding modes to the TiO_2/Fe_2O_3 binary mixed oxides were also investigated using EXAFS. From these studies, it has been possible to conclude that both As^{III} and As^{V} possibly bind with the Fe atoms on the surface of the binary mixed oxides as bidentate mononuclear edge sharing (^2E) complexes or bidentate binuclear corner sharing (^2C) complexes. On the other hand, both arsenic oxidation states can form bidentate binuclear corner sharing (^2C) complexes with Ti atoms on the binary mixed oxide surfaces. The binding modes of arsenic on three different types TiO_2/Fe_2O_3 binary mixed oxides are not significantly different. We also found that neither the adsorption pHs nor the adsorption times have significant effect on the binding modes of arsenic onto the binary mixed oxide surfaces (see Chapter 4).

The photocatalytic oxidation studies indicates that As^{III} adsorbed on the surface of the binary mixed oxides can be photocatalytically oxidized to As^{V} through a mechanism that introduces photons (UV or synchrotron) to generate valence band hole (h^+_{vb}) and conduction band electron (e^-_{cb}) which are important species to produce hydroxyl radical (OH^*) and superoxide (O_2^{*-}) in the oxidation process. Additionally, the photocatalytic oxidation mechanism studies in this research indicates that hydroxyl radicals (OH^*) produced on the binary mixed oxide surfaces upon exposure to light are likely to be the main species for the oxidation of As^{III} to As^{V} (see Chapter 5). This process seems to be analogous for the three TiO_2/Fe_2O_3 binary mixed oxides under study.

6.2 Future work

One of the key areas for future work is the adaptation of the materials and processes developed in this thesis onto a continuous flow device that can be

effectively used to purify water contaminated with arsenic. For this, the first step will be to investigate the process using a fixed bed column under continuous flow.

Experiments should be undertaken to establish the optimum flow parameters for the column (packed with mesoporous TiO_2/Fe_2O_3 binary mixed oxides) to establish that arsenic adsorption is still efficient at higher flow rates, as this would be advantageous in future applications. The column experiments should then be studied for the remediation of arsenic contaminated water to show that these binary mixed oxides are capable of reducing arsenic levels in water. This will initially involve examining the effect of influent arsenic concentration on adsorption and subsequently the experimental conditions will be optimized. Moreover, the effect of the presence of competing anions should be investigated before remediating the real contaminated water. The optimized system should then be tested with tap water spiked with arsenic and then with real ground water samples in order to demonstrate the ability of these materials to remove arsenic from contaminated water.

Regarding the nature of the MB, some specific properties should be studied further including determination of band gap energy, investigation of the surface charge, and amount of hydroxyl radical produced by the binary mixed oxides.

References

(1) D'Arcy, M.; Weiss, D.; Bluck, M.; Vilar, R. *J. Colloid Interface Sci.* **2011**, *364*, 205-212.

(2) Bullough, F.; Berry, A.; Weiss, D.; Vilar, R. *PhD transfer report*. **2012**.